LINEAR INSTABILITY AND CONTROL METHODS OF FIRST MACK MODE AND CROSSFLOW MODE

JIACHEN LU

PhD

The Hong Kong Polytechnic University

2025

The Hong Kong Polytechnic University

Department of Aeronautical and Aviation Engineering

Linear Instability and Control Methods of First Mack Mode and Crossflow Mode

Jiachen Lu

A thesis submitted in partial fulfilment of the requirements for the degree of Doctor of Philosophy

Jun 2025

CERTIFICATE OF ORIGINALITY

I hereby declare that this thesis is my own work and that, to the best of my knowledge and belief, it reproduces no material previously published or written, nor material that has been accepted for the award of any other degree or diploma, except where due acknowledgement has been made in the text.

_____ (Signed)

LU, Jiachen (Name of student)

Abstract

First Mack modes and crossflow instabilities play critical roles in supersonic boundary layer transitions, whereas they have not received sufficient attention. Several critical issues require further investigation: First Mack modes lack a physics-based comprehension of their behavior across varying spanwise wavenumbers. Their distinct responses to control techniques at different spanwise wavenumbers have not been systematically evaluated. The identification of crossflow instabilities and their independence from first Mack modes in hypersonic regime remain contested. The stabilization mechanisms of crossflow modes have not been clearly elucidated. This thesis addresses these theoretical and engineering challenges through direct numerical simulation, linear stability theory, and momentum potential theory.

The first part focuses on the linear instability and control strategies of first Mack modes at varying spanwise wavenumbers in a Mach 4.5 flat-plate boundary layer. As the spanwise wavenumber increases, the streamwise wavenumber initially rises before declining, with its maximum marking the transition of the first mode from an acoustic to a vortical nature. These distinct physical characteristics result in divergent responses to laminar control techniques and differing stabilization mechanisms: Wall cooling slightly stabilizes planar first modes and significantly stabilizes oblique first modes by suppressing the thermal components. Similarly, wall suction exhibits a weaker stabilization effect on planar first modes compared to their oblique counterparts, with thermal and vortical components in the oblique mode damped under steady suction. For porous coatings, slightly oblique first modes are modulated by scattering effects and wall admittance, whereas highly oblique first modes are destabilized by mean-flow distortions induced by the coatings. Grooves, despite their macroscale geometry relative to porous coatings, govern planar first modes through wall admittance mechanisms, where acoustic components are modulated by wall admittance. For highly oblique first modes, mean-flow distortions are responsible for the destabilizing effects.

The second part provides new evidence for the consistency of first Mack and crossflow modes. Boundary-layer receptivity to three-dimensional slow acoustic and vorticity waves over a Mach 5.9 sharp wing is systematically investigated under varying sweep angles. Uniform behaviors between these modes highlight their consistency: Linear stability theory categorizes both instabilities as S modes. The vortical component dominates both modes, emphasizing their inherent vortical nature. These modes share identical receptivity pathways: For slow acoustic waves, strong acoustic components

are generated at the leading edge through the synchronization mechanism and subsequently diminish. The vortical components grow steadily throughout the receptivity process, resulting in a high-growth-rate non-modal growth phase of perturbations. After adjustments of acoustic and thermal components, the linear growth occurs. While for vorticity waves, leading-edge disturbances primarily consist of vortical components, arising from interactions between vorticity waves, shock waves, and boundary layers. Acoustic and vortical components go through adjustment in their shape, and thermal components exhibit initial decay followed by recovery, resulting in a lower-growth-rate non-modal growth phase. Ultimately, the linear growth phase commences.

The final part investigates the stabilization mechanisms of crossflow modes in a Mach 6 blunt-wing boundary layer. Wall cooling can effectively stabilize the crossflow mode by predominantly suppressing the thermal component. Wall suction exhibits limited control effects and directly influences the vortical component. Porous coatings and macro-slit grooves exhibit moderate stabilization effects on the crossflow mode. Mean-flow distortions are identified as the primary driver of their stabilization effects. Stabilization mechanisms of crossflow instabilities exhibit significant parallels with those of first Mack modes, further highlighting their physical consistency.

List of Publications

Publications arising from the thesis are listed below.

Journal Papers

J. Lu, K. C. K. Uy, R. Zhao, and C. Wen, "Stabilization mechanisms of traveling crossflow mode in hypersonic swept wing flows," *AIAA Journal*, vol. 63, pp. 1176–1190, 2025.

J. Lu, R. Zhao, K. C. K. Uy, and C. Wen, "Acoustic-Vortical Evolution Mechanisms of Supersonic First Mack Mode," *Physics of Fluids*, vol. 37, issue 7, pp. 074101, 2025.

J. Lu, K. C. K. Uy, R. Zhao, and C. Wen, "On the Receptivity of First and Crossflow Modes in Hypersonic Sharp Wing Flows," *Journal of Fluid Mechanics*, vol. 1021, pp. A18, 2025.

J. Lu, R. Zhao, K. C. K. Uy, and C. Wen, "Stabilization Mechanisms of First Mack mode in Supersonic Flat Plate Flows," (in preparation).

Conferences

J. Lu, K. Chun Kit Uy, R. Zhao, and C. Wen. "The identification method of crossflow modes in hypersonic boundary layers," in *the 13th National Fluid Mechanics Academic Conference*, Harbin, China, 2024.

J. Lu, R. Zhao, K. Chun Kit Uy, and C. Wen. "Stabilization mechanisms of various methods on the traveling crossflow instability in hypersonic boundary-layer flows," in the 1st European Fluid Dynamics Conference, Aachen, Germany, 2024.

J. Lu, R. Zhao, and C. Wen. "Research on the First Mack Mode Based on Momentum Potential Theory," in the 31th Annual Conference of BSTAM, Beijing, China, 2025. (outstanding paper award)

J. Lu, K. Chun Kit Uy, R. Zhao, and C. Wen. "Three-Dimensional Receptivity of Hypersonic Boundary Layers over Sharp Wings," in *the 35th International Symposium on Shock Waves*, Brisbane, Australia, 2025.

Acknowledgements

First and foremost, I would like to express my deepest gratitude and highest respect to my chief supervisor, Prof. Chih-yung Wen. His profound knowledge and sharp academic vision have guided me to an in-depth exploration of boundary layer instability and shaped my academic perspective. Without his continuous support, I would not have been able to complete this thesis. Beyond research, Prof. Wen is also a kind friend who taught me to appreciate life. He ignited my passion for both academic pursuits and life itself.

I also offer my sincere appreciation to my co-supervisor, Prof. Rui Zhao. He has created opportunities for me to engage with the academic community and provided valuable guidance and constructive feedback throughout my research, from which I greatly benefited.

I extend my gratitude to my collaborator, Dr. Chun-kit Uy, for his essential guidance in helping me start my research, master necessary methodologies, and tackle various practical challenges.

I am deeply grateful to my research fellows in the fluid mechanics group, Prof. Jiaao Hao, Prof, Zijian Zhang, and Dr. Peixu Guo, for their insightful discussions and comments.

I also want to acknowledge all the members of Prof. Wen's laboratory for their friendship and kindness.

Finally, I would like to thank my family for their unconditional love, encouragement and support.

Table of Contents

Abstract i

List of Publications iii

Acknowledgements iv

Table of Contents v

List of Figures viii

List of Tables xii

Chapter 1 Introduction 1

1.1. Background 1

1.2. Second Mack mode 2

1.3. First Mack mode 2

1.4. Crossflow mode 3

1.5. Receptivity process 5

1.6. Laminar control techniques 6

1.7. Momentum potential theory 8

1.8. Thesis Outline 8

Chapter 2 Methodology 11

2.1. Direct Numerical Simulation 11

2.2. Linear Stability Analysis 13

2.3. Momentum Potential Theory 14

Chapter 3 Stabilization Mechanisms of First Mack Mode 17

3.1. Problem Description 17

3.2. Acoustic–Vortical Evolution Mechanisms of First Mack Mode 19

3.2.1. Linear stability theory results 19

3.2.2. Direct numerical simulation results 20
3.2.3. Momentum potential theory results 22
3.3. Stabilization of First Mack Mode 23
3.3.1. Wall cooling-heating 23
3.3.2. Wall blowing-suction 25
3.3.3. Porous coatings 27
3.3.4. Grooves 32
3.4. MPT Analysis of Stabilization Mechanisms 38
3.4.1. Wall cooling-heating 38
3.4.2. Wall blowing-suction 40
3.4.3. Porous coatings 42
3.4.4. Grooves 45
3.5. Summary 49
Chapter 4 Stabilization Mechanisms of Crossflow Mode 50
4.1. Problem Description 50
4.2. Stabilization of Crossflow Mode 53
4.2.1. Wall cooling-heating 53
4.2.2. Wall blowing-suction 55
4.2.3. Porous coatings 57
4.2.4. Grooves 61
4.3. MPT Analysis of Stabilization Mechanisms 64
4.3.1. Wall cooling-heating 64
4.3.2. Wall blowing-suction 67
4.3.3. Grooves 69
4.4. Summary 71
Chapter 5 Unified Identification of First Mack and Crossflow Instabilities 73

5.1. Problem Description 73
5.2. Linear Stability Theory Results 76
5.3. Receptivity to Freestream Waves 79
5.3.1. Receptivity to slow acoustic waves 81
5.3.2. Receptivity to vorticity waves 89
5.4. Summary 96
Chapter 6 Conclusion 98
6.1. Summary and Conclusions 98
6.2. Possible Directions for Future Work 99
References 101

List of Figures

Figure 1-1 A flowchart depicting the structure of the thesis. 9

Figure 3-1 Schematic of the problem formulation: (a) supersonic boundary-layer flow over a flat plate, (b) stabilization techniques, and (c) geometric parameters for cavities. 18

Figure 3-2 Code and grid-independence verification for the baseline case. 18

Figure 3-3 α_r and α_i eigenfunctions at $x^* = 0.7$ m under different β. Legends from (b) to (f) are the same. 20

Figure 3-4 p' contours and perturbation streamlines under different β. 21

Figure 3-5 Instantaneous snapshots of MPT components when $\beta = 0, 0.7, 1.18$. unit: kg/(m^{2}s). 22

Figure 3-6 Normalized MPT components at $x^* = 0.7$ m when $\beta = 0, 0.7, 1.18$. 23

Figure 3-7 Baseflow profiles at $x^* = 0.7$ m for wall cooling-heating cases. 24

Figure 3-8 The maximum u' in wall cooling-heating cases. 24

Figure 3-9 Perturbation streamlines in case $T_w = 2$ 25

Figure 3-10 Baseflow profiles at $x^* = 0.7$ m for wall blowing-suction cases. 26

Figure 3-11 The maximum u' in wall blowing-suction cases. 26

Figure 3-12 Perturbation streamlines in wall-suction cases. 27

Figure 3-13 Instantaneous wall pressure perturbations under different grid resolutions when $\beta = 1.18$. 28

Figure 3-14 Averaged baseflow profiles at $x^* = 0.7$ m for porous coating cases. 29

Figure 3-15 Evolution of maximum velocity perturbations with different porous coatings. 30

Figure 3-16 Growth rates from LST and baseflow pressure contours of porous-coating cases. 31

Figure 3-17 Perturbation streamlines in coating case $\theta = 1.5\pi$. 31

Figure 3-18 The maximum u' in case *H1b0.5* under different grid resolutions. 33

Figure 3-19 The maximum u' in grooved cases with different widths. 34

Figure 3-20 The maximum u' in grooved cases with different heights.....35

Figure 3-21 The baseflow pressure contours in grooved cases. 36

Figure 3-22 Comparison of LST growth rates between cases *H1b0.5* and *H1.5b0.5*..37

Figure 3-23 Baseflow profiles at $x^* = 0.7$ m for grooved cases. 37

Figure 3-24 Perturbation streamlines in grooved cases. 38

Figure 3-25 The MPT component magnitudes at $x^* = 0.7$ m in 2D $T_w = 2$ case. Unit: kg/(m^{2}s).....39

Figure 3-26 The MPT component magnitudes at $x^* = 0.7$ m in 3D $T_w = 2$ case. Unit: kg/(m^{2}s).....39

Figure 3-27 The MPT component magnitudes at $x^* = 0.7$ m for 2D wall-suction case. Unit: kg/(m^{2}s).....41

Figure 3-28 The MPT component magnitudes at $x^* = 0.7$ m for 3D wall-suction case. Unit: kg/(m^{2}s).....41

Figure 3-29 The average MPT component magnitudes at $x^* = 0.7$ m for 2D porous coating cases. Unit: kg/(m^{2}s). 43

Figure 3-30 The average MPT component magnitudes at $x^* = 0.7$ m for 3D porous coating cases. Unit: kg/(m^{2}s). 43

Figure 3-31 Instantaneous magnitude of MPT components for case $\theta = 0.5\pi$. Unit: kg/(m^{2}s).....45

Figure 3-32 Instantaneous magnitude of MPT components for case $\theta = 1.5\pi$. Unit: kg/(m^{2}s).....45

Figure 3-33 The average MPT component magnitudes at $x^* = 0.7$ m for 2D grooved cases. Unit: kg/(m^{2}s). 46

Figure 3-34 The average MPT component magnitudes at $x^* = 0.7$ m for 3D grooved cases. Unit: kg/(m^{2}s). 46

Figure 3-35 Instantaneous magnitude of MPT components for case *H1b0.5*. Unit: kg/(m^{2}s).....48

Figure 3-36 Instantaneous magnitude of MPT components for case *H1.5b0.5*. Unit:

kg/(m^{2}s). 48

Figure 4-1 Schematic of the geometry and problem formulation. 50

Figure 4-2 Spatial growth rate from LST. 51

Figure 4-3 Evolutions of disturbances from DNS. 52

Figure 4-4 Spatial growth rates in the baseline case using different grids. 53

Figure 4-5 Baseflow quantities at s^* = 80 mm in wall cooling cases. 54

Figure 4-6 N factors in wall cooling cases. 55

Figure 4-7 Baseflow quantities at s^* = 80 mm in wall suction cases. 56

Figure 4-8 N factors in wall suction cases. 57

Figure 4-9 Definitions of porous coating and groove parameters. 57

Figure 4-10 N factor in porous coating cases. 58

Figure 4-11 Average baseflow quantities at s^* = 80 mm in porous coating cases. 59

Figure 4-12 Schematic of LST regions for different modes. 60

Figure 4-13 Growth rates from LST and baseflow pressure contours of porous-coating cases. 60

Figure 4-14 N factors in the *H1b0.5* case using different grids. 61

Figure 4-15 N factor in grooved cases. 62

Figure 4-16 N factor at s^* = 110 mm. 62

Figure 4-17 Growth rates from LST and baseflow pressure contours of grooved cases. 63

Figure 4-18 Average baseflow quantities at s^* = 80 mm in grooved cases. 64

Figure 4-19 The instantaneous snapshots of MPT components. 65

Figure 4-20 The amplitudes of MPT components in the 0.8T_r case. 67

Figure 4-21 The instantaneous snapshots of MPT components in wall suction cases. 68

Figure 4-22 The amplitudes of MPT components in the wall suction case. 69

Figure 4-23 The instantaneous snapshots of MPT components in grooved cases. 70

Figure 4-24 The amplitudes of MPT components in grooved cases.....71

Figure 5-1 The schematic of the spanwise-infinite swept wing and coordinate systems 74

Figure 5-2 The baseflow contours over the front airfoil ($x^* = 0 \sim 40$ mm) for the $\Lambda = 0°$ case.....75

Figure 5-3 Baseflow variables in different cases. 75

Figure 5-4 Growth rate contours at $s^* = 40$ mm.....76

Figure 5-5 Pressure gradients and spatial growth rates under different thicknesses. ..78

Figure 5-6 The evolution of F and S modes. 79

Figure 5-7 The density fluctuation contours. 82

Figure 5-8 The streamwise velocity fluctuation contours.....83

Figure 5-9 The wall density fluctuation amplitudes and streamwise wavenumbers. ..84

Figure 5-10 The u' profiles for AC-0° and AC-45° cases at neutral points. 85

Figure 5-11 The instantaneous snapshots of MPT components.....86

Figure 5-12 The normalized amplitudes of MPT components. 87

Figure 5-13 The receptivity coefficients of all cases. 89

Figure 5-14 The streamwise velocity fluctuation contours.....90

Figure 5-15 The density fluctuation contours. 91

Figure 5-16 The wall density fluctuation amplitudes and streamwise wavenumbers. 92

Figure 5-17 The instantaneous snapshots of MPT components. 94

Figure 5-18 The normalized amplitudes of MPT components. 95

List of Tables

Table 3-1 Porous coating parameters and growth rates at $x^* = 0.7$ m. 28

Table 3-2 Wall admittances and growth rates of grooves with different cavity widths. 34

Table 3-3 Wall admittances and growth rates of grooves with different cavity heights. 35

Table 3-4 Comparison of λ_x^* between the baseline case and the wall-cooling case. ..40

Table 3-5 Comparison of λ_x^* between the baseline case and the wall-suction case. ..41

Table 3-6 Comparison of λ_x^* between the baseline case and case $\theta = 0.5\pi$. 43

Table 3-7 Comparison of λ_x^* between the baseline case and case $\theta = 1.5\pi$. 44

Table 3-8 Comparison of λ_x^* between the baseline case and case *H1b0.5*. 47

Table 3-9 Comparison of λ_x^* between the baseline case and case *H1.5b0.5*. 47

Table 4-1 Freestream conditions. 51

Table 4-2 Porous coating parameters. 58

Table 4-3 Comparison of λ_s^* between the baseline case and the wall cooling case. 66

Table 4-4 Comparison of λ_s^* between the baseline case and the wall suction case. 67

Table 4-5 Comparison of λ_s^* between the baseline case and grooved cases. 70

Table 5-1 Free-stream conditions. 74

Table 5-2 Locations of neutral points at different sweep angles. 79

Table 5-3 The spatial wavenumbers $\alpha_{r,\infty}$ of freestream disturbances. 81

Chapter 1 Introduction

1.1. Background

Laminar–turbulent transition in supersonic boundary layers significantly impacts the performance of supersonic vehicles by inducing substantial local skin friction and heat flux[1,2]. Analyses from the National Aerospace Plane (NASP) project suggest a potential doubling of payload capacity if the fully laminar boundary layer is maintained, compared to those in fully turbulent scenarios[3]. Furthermore, heat transfer during the transition process can exceed that in fully turbulent regions[4]. Therefore, understanding the transition mechanisms of boundary layers and developing effective flow control techniques are critically important.

In low-disturbance flight environments, this transition process follows these fundamental stages[5]: (1) receptivity, (2) linear instability, (3) nonlinear instability, and (4) breakdown. During the receptivity phase, external free-stream perturbations, such as acoustic waves, entropy fluctuations, or vortical disturbances, interact with the boundary layer, generating instability modes within the shear layer[6,7]. The initial amplitudes of unstable modes typically remain orders of magnitude below characteristic flow scales, permitting linear stability theory (LST) to accurately model the exponential growth of instabilities during the linear stage. Further downstream, the amplitudes of the disturbances eventually saturate, nonlinear interactions and secondary instabilities emerge, and the flow undergoes rapid breakdown to turbulence within a brief downstream interval.

LST enables detailed analysis of linear instability mechanisms, with several instabilities identified as primary drivers of transition in supersonic flows[8–10], including the first Mack mode, the second Mack mode, and the crossflow mode. Along quasi-two-dimensional supersonic aircraft leading edges, the first mode is the most amplified instability at low-Mach-number boundary layers, whereas the second mode exhibits higher growth rates as the Mach number exceeds 3.8[11,12]. In the three-dimensional (3D) boundary layers subject to pressure gradients and sweep effects, curved inviscid streamlines at the boundary layer edges generate a generalized inflection point (GIP) within the crossflow profile and induce the crossflow instability[13]. Identifying the physical nature of these unstable modes is essential for the prediction of boundary layer transition and designing laminar control techniques, benefiting further engineering applications. A literature review is then presented, which

addresses pivotal aspects of supersonic boundary layer transition, including physical properties of unstable modes, the receptivity process, laminar control techniques, and the analysis tool.

1.2. Second Mack mode

The second mode has attracted significant attention due to its higher growth rates in hypersonic boundary layers. As early as the 1980s, it was identified as an inviscid mode[11], characterized by increasing maximum growth rates with larger Reynolds number. Subsequent studies made significant progress in understanding its physical nature, classifying the second mode as an acoustic mode[14,15]. Its instability waves were interpreted as acoustic waves trapped between the wall and the sonic line.

In recent years, advances in numerical simulations and analytical methods have further clarified the physics and energy sources of the second mode within different theoretical frameworks: Kuehl[16] suggested that the dynamics of the second mode align with a forced, resonating, thermoacoustic standing wave trapped in a thermoacoustic impedance well, deriving energy from thermoacoustic Reynolds stresses. Tian et al.[17], using a relative phase analysis based on the linearized Navier-Stokes equations, demonstrated that wall-normal velocity perturbations dominate energy extraction from the mean flow for the second mode.

1.3. First Mack mode

First Mack modes were traditionally regarded as dispensable drivers for supersonic boundary layer transition when Mach number exceeds 3.8, as they show obviously smaller growth rates. However, recent studies have also emphasized the essential role of the first Mack mode in the transition process. Lee's group[18,19] systematically investigated boundary-layer transition in hypersonic cone experiments, confirming that the first mode serves as the origin of soliton-like wave packets in turbulence and plays a critical role in transition. Recent numerical studies by Guo et al.[20] on a Mach 6 flat-plate boundary layer revealed that the first mode acts as the source of detuned modes responsible for boundary-layer transition. These findings suggest that the first mode may assume a more pivotal role in hypersonic boundary-layer transition, necessitating further investigations into its physical mechanisms.

Compared to the extensive investigations involving second Mack modes, significant gaps remain in comprehending first modes. Mack[8], while solving LST problems in compressible flows, concluded that the most unstable first mode must

inherently be three-dimensional. The most unstable first mode is regarded as an extension of Tollmien-Schlichting (TS) waves from incompressible boundary layers to supersonic regimes[21] and is classified physically as a vortical mode[22]. Smith[23] identified the first mode as a viscous-inviscid mixed mode whose properties vary with wave angle. When the wave angle ψ satisfies $\psi > \tan^{-1}\left(\sqrt{Ma^2-1}\right)$, the first mode manifests as a viscous mode, characterized by a maximum amplification rate that increases as the Reynolds number decreases[11]. Recently, Liang et al.[24] proposed an inviscid energy analysis framework, revealing that the phase difference between streamwise velocity and pressure perturbations near the GIP serves as the energy source for the first mode.

Although previous research confirmed that the physical nature of the first mode is closely related to its wave angle[23], a systematic comparative analysis of its dynamical behavior under different wave angles remains lacking. Schmid and Henningson[21] demonstrated that viscous instability completely vanishes when the Mach number exceeds 3.8. Meanwhile, Mach 4.5 represents a proposed working Mach number for future high-speed cruise aircraft[25] and is also a typical operating condition during the takeoff and landing phases of hypersonic vehicles, highlighting the necessity of further investigations into flow dynamics and instability at this regime.

1.4. Crossflow mode

The crossflow modes originate from the GIP within the crossflow profile and serve as a prevalent and important mechanism in the transition stage among various 3D configurations, such as yawed cones[26–29], swept wings[30–32], and other complex configurations[33–36]. They can be classified into two categories: stationary crossflow modes and traveling crossflow modes, differentiated by their respective frequencies. These two instabilities have different origins: Traveling crossflow modes are sensitive to the freestream turbulence level, while stationary crossflow modes are affected by surface roughness[37,38]. Stationary crossflow modes are traditionally recognized as being dominant in real high-speed flights and have received more attention than their traveling counterparts[32,39,40], due to the low environmental noise at high altitudes and inevitable surface roughness[41–43]. However, traveling crossflow modes were detected and identified in recent model flight experiments by Wan et al.[44], in which pressure signals were obtained over an inclined blunt cone. The low-frequency signals peaked at about 10 kHz, and were identified as traveling crossflow modes through the high level of consistency between LST and experimental results. These results confirmed that traveling crossflow modes can be responsible for hypersonic laminar–turbulent

transitions under real flight conditions. Qiu's[31] numerical results also demonstrate that traveling crossflow vortices are essential for forming low-frequency hairpin-like structures that ultimately trigger turbulence.

A long-standing conceptual debate in hypersonic regimes concerns the independence and identification of the first Mack and crossflow modes. In low Mach number regimes, the crossflow instability and the Tollmien-Schlichting (T-S) wave (or the first Mack mode) occupy distinct frequency ranges[10,45]. The crossflow instability is near zero frequency over a large spanwise wavenumber range, while the first Mack mode is present at positive frequencies. However, in high Mach-number flows, distinguishing the dominant mode becomes challenging. Liu[10,46] employed the compressible Falkner-Skan-Cooke flow model and LST to investigate the theoretical property of first and crossflow instabilities. They discovered that the crossflow instability integrates with S modes, making it indistinguishable from the first mode at large local sweep angles or Mach numbers greater than 1.6. Similar identification challenges were observed by Peck et al.[47] in a study of a highly swept fin positioned over a cone at a Mach number of 6. In that configuration, the flow between the transition front and the fin leading edge is subject to large crossflow velocities and strong pressure gradients. However, their energy budget analysis indicated that the magnitudes of crossflow-related terms were not substantial compared to streamwise terms. Whether the primary mechanism for transition is driven by crossflow instability or the first Mack mode remains uncertain. Several criteria attempt to determine whether the dominant instability in transition is the first Mack mode or the crossflow mode. Reed and Saric[48] proposed a threshold for low-speed scenarios where transition is attributed to the crossflow mode if the maximum crossflow velocity exceeds 3% of the boundary-layer-edge velocity. Liu[46] suggested that the $|u'|$ profile of T-S modes (or first modes) exhibits dual peaks in the weakly compressible regime, versus crossflow modes display a single peak. However, both metrics can be problematic in high-speed regimes and geometrically complex flows with distorted boundary layers (e.g., Peck et al.[47]). To date, the only explicit criterion that can "distinguish" these two modes involves their pressure gradient responses: first modes are damped by favorable pressure gradients[49,50], whereas the crossflow instabilities are amplified[51].

Fundamental questions persist regarding the mode identification, particularly given overlapping frequency responses and analogous sensitivities to Mach number and wall thermal conditions. This raises intriguing questions: Are the first and crossflow modes of the same nature? Further, are they actually the same instability? Do these consistent responses originate from their same nature?

1.5. Receptivity process

The receptivity stage establishes the initial disturbance amplitudes of instabilities. That of second Mack modes has been thoroughly investigated[52–55]. Fedorov and Khokhlov[56] pioneered this field by establishing a theoretical framework via the multiple-mode method, demonstrating that second Mack modes arise from the excitation of the fast (F) or slow (S) mode near the leading edge and intermodal conversion downstream at the synchronization point, where F and S modes share nearly identical phase speeds. Subsequently, Ma and Zhong conducted a series of numerical simulations on the receptivity of a Mach 4.5 sharp flat plate boundary layer to acoustic, vortical, and entropy waves[57–59], which physically relate to pressure, temperature (or density), and velocity fluctuations[60]. Their results further affirm the synchronization theory of Fedorov and Khokhlov. Balakumar et al. numerically investigated the boundary-layer receptivity over diverse geometries, e.g. sharp and blunt cones[61], straight and flared cones[62], sharp and blunt wedges[7], further confirming Fedorov's synchronization theory when the disturbance frequency supports the second mode.

Despite extensive investigations of second Mack modes, research on the receptivity of first and crossflow modes to free-stream disturbances remains limited[41,63,64]. When the frequency is not high enough to sustain the second mode, the F mode remains neutral within the boundary layer, precluding synchronizations between the F mode and vortical or S modes[65]. This results in fundamentally divergent receptivity pathways compared to second Mack modes. Balakumar and King[41] quantified the receptivity of a Mach 3 swept wing boundary layer with direct numerical simulation (DNS), proposing receptivity coefficients for roughness, acoustic, and vortical disturbances. Their results demonstrated that acoustic disturbances are about eight times weaker in generating unstable traveling crossflow vortices compared to the vorticity waves. Xu et al.[64] applied LST in a Mach 6 three-dimensional boundary layer, showing that the discrete-spectrum slow mode can be excited by the slow acoustic waves from the continuous spectrum near the leading edge, and evolve downstream into the unstable traveling crossflow mode. Liu et al.[63] combined triple-deck theory and DNS to reveal a pathway of generating first Mack modes through the interaction between slow acoustic waves and streamwise isolated wall roughness.

As the receptivity stage explains the origins of instabilities, divergent receptivity pathways would imply independent instability mechanisms. Clarifying whether first Mack and crossflow modes share identical receptivity pathways provides new evidence for the conceptual controversy between the oblique first and traveling crossflow mode.

1.6. Laminar control techniques

After comprehending the dynamics of unstable modes, designing control methods becomes necessary. Various laminar control techniques have been developed to delay transition. Kimmel[66] categorized these approaches into active and passive methods. Active control methods include wall blowing-suction[67–69], wall heating-cooling[70–72], and plasma actuators[73,74], while passive strategies encompass global or local shaping[75,76] and porous coatings[77]. These approaches exhibit distinct stabilization effects on different instability modes.

For Mack modes, wall heating-cooling and blowing-suction have been investigated since the last century. Lysenko and Maslov[78] experimentally confirmed that wall cooling stabilizes first-mode instabilities while destabilizes second-mode disturbances as early as the 1980s. Malik[79] attributed this stabilizing effect on the first mode to the formation and subsequent disappearance of a second GIP in regions where $u < 1 - 1/M_e$. For the second mode, the destabilization effect is interpreted by the region in the boundary layer where $M^2 > 1$ expands with cooling. In contrast, wall steady blowing-suction exhibits aligned effects on first and second Mack modes[80]. Wall suction reduces the peak growth rates of both first and second Mack modes. Malik also linked the stabilizing effect on first Mack modes of wall suction to the second GIP. Poulain et al.[81] employed an adjoint-based optimization technique to identify optimal wall control strategies. Their analysis revealed that wall blowing-suction modifies streamwise momentum transport between the critical layer and the boundary layer edge, while wall heating and cooling targets thermally sensitive regions.

Building on the acoustic nature of second modes, Malmuth et al.[12] proposed that wall acoustic absorbers (porous materials) could potentially stabilize the second mode. Follow-up theoretical[82,83], numerical[84], and experimental[85,86] investigations by Fedorov et al. confirmed that porous surfaces suppress second-mode growth through acoustic absorption mechanisms. They further established an impedance model for porous surfaces based on acoustic wave propagation theory in narrow pores. Currently, acoustic porous walls, as a passive flow control technique, have been widely applied and extensively studied for delaying second-mode-dominated boundary layer transition[77]. In contrast, their impact on first Mack modes reveals complex behavior. Fedorov et al.[86] conducted experimental and theoretical studies on the effect of an ultrasonically absorptive coating on a Mach 6 sharp cone, finding that the coating strongly stabilizes the second mode while marginally destabilizing the first mode. Wang and Zhong[87] discovered that this amplification effect can be mitigated by reducing the

admittance phase of the coating. Tian et al.[88] demonstrated that the planar first mode can be marginally stabilized when the admittance phase φ approaches 0.5π. Zhao et al.[89] designed an acoustic metasurface to suppress the planar first mode; however, their DNS yielded results that contradicted LST predictions, which they attributed to a "roughness" effect. Chen et al.[90] employed relative phase analysis to explain the energy transfer of the planar first mode under porous coatings, attributing destabilization to the wall-normal transport term, though their investigation was based solely on LST. Liu et al.[91] integrated the admittance model into their nonlinear parabolized stability equation (NPSE) code and observed that the admittance wall boundary delays the oblique breakdown of the first mode. However, their study did not consider the effects of real cavity structures and relied exclusively on NPSE, omitting DNS. To date, the effects of porous coatings on first modes remain unresolved, and investigations of 3D first modes are scarce.

The geometric dimensions of porous coatings are typically much smaller than boundary-layer thicknesses to preserve aerodynamic smoothness[82,92]. An intriguing question emerges regarding groove effects when cavity dimensions exceed these thresholds, especially when the geometric scales are close to the boundary-layer thicknesses. For second Mack modes, increasing the slit spacing will lead to stronger scattered waves at the surface and weaken the acoustic stabilization capability[84,93]. This scale-related behavior remains uncharacterized for first modes.

For crossflow instabilities, these laminar flow control techniques have also been developed. A detailed investigation of wall suction by Friederich and Kloker[94] found that both the primary and secondary crossflow instability can be stabilized by homogeneous suction at the wall, while strong, localized "pinpoint" suction has a much better control effect. Eppink and Wlezien[95] analyzed data obtained from the NASA/Boeing Hybrid Laminar Flow Control Crossflow Experiment and found that the traveling crossflow mode is highly sensitive to the wall temperature. Subsequent experiments by Saric and Reed[51] demonstrated that providing initial subcritical 3D biasing to the baseflow (via holes, glow discharge, or bumps) can suppress the amplification of the stationary crossflow mode. Recently, Fedorov and Novikov[96] used LST to show that spanwise-invariant grooves can delay the onset of crossflow-induced transition.

Despite these advancements, the mechanisms behind these control techniques remain inadequately interpreted due to a lack of suitable analysis techniques. Key unresolved challenges include the divergent responses of two-dimensional (2D) and 3D first modes to control techniques and the absence of a physics-based interpretation of

their stabilization effects.

1.7. Momentum potential theory

Infinitesimal freestream disturbances can be decomposed into three modes, namely the vortical, acoustic, and entropic modes. Kovasznay[97] first performed this decomposition based on three independent differential equations. However, Kovasznay's approach is not applicable to nonuniform flow fields. Doak proposed a new decomposition for time-stationary fluctuating flow fields, namely Doak's momentum potential theory (MPT)[98,99]. In Doak's approach, the momentum density field $\rho\boldsymbol{u}$ is decomposed into vortical, acoustic, and thermal components. The vortical component contains all rotational motion, while the irrotational motion is split into acoustic (irrotational and isentropic) and thermal (irrotational and isobaric) components. The explicit physical significance of the decomposition makes MPT an elegant tool for identifying the physical essence of disturbances and providing physics-based explanations in time-stationary fluctuating flows[100–102].

In recent years, MPT has been employed to provide an intuitive and systematic interpretation for the evolution and damping of unstable modes. Unnikrishnan and Gaitonde[103,104] used MPT to decompose the instability modes in a Mach 6 boundary-layer flow, providing a detailed analysis of the evolution of unsteady modes and the effect of wall cooling in transition processes. Long et al.[105,106] employed MPT to explore the underlying energy mechanisms of the second mode and its response to a grooved porous coating. Liu et al.[107] further examined the stabilization mechanisms of absorptive, near-zero-impedance, and reflection-controlled metasurfaces on the second mode in the MPT framework. Zhu and Lee[108] used this framework to clarify the heating reduction mechanism caused by a wavy surface. MPT will be employed to provide an intuitive and systematic interpretation for the evolution and damping of unstable modes in this thesis.

1.8. Thesis Outline

As critical gaps have been identified hereinbefore, this thesis investigates the linear instability and control methods of first Mack and crossflow instabilities. The study will first analyze the mechanism evolution of first Mack modes under varying spanwise wavenumbers, followed by a systematic assessment of their responses to stabilization techniques, including wall cooling–heating, wall blowing–suction, porous coatings, and grooves. Subsequently, the stabilization mechanisms of crossflow modes

under these control methods will be examined. Finally, the conceptual debates between the oblique first mode and traveling crossflow mode will be addressed.

The thesis is structured into six chapters. An overview of each chapter is provided as follows, and the structure of the thesis is depicted in Figure 1-1:

Chapter 1 is the introduction, beginning with an overview of the research background. This is followed by a literature review on the transition of supersonic boundary layers, which encompasses key aspects such as physical properties of unstable modes, the receptivity process, laminar control techniques, and the analysis tool. The chapter concludes by outlining the structure and objectives of the present study.

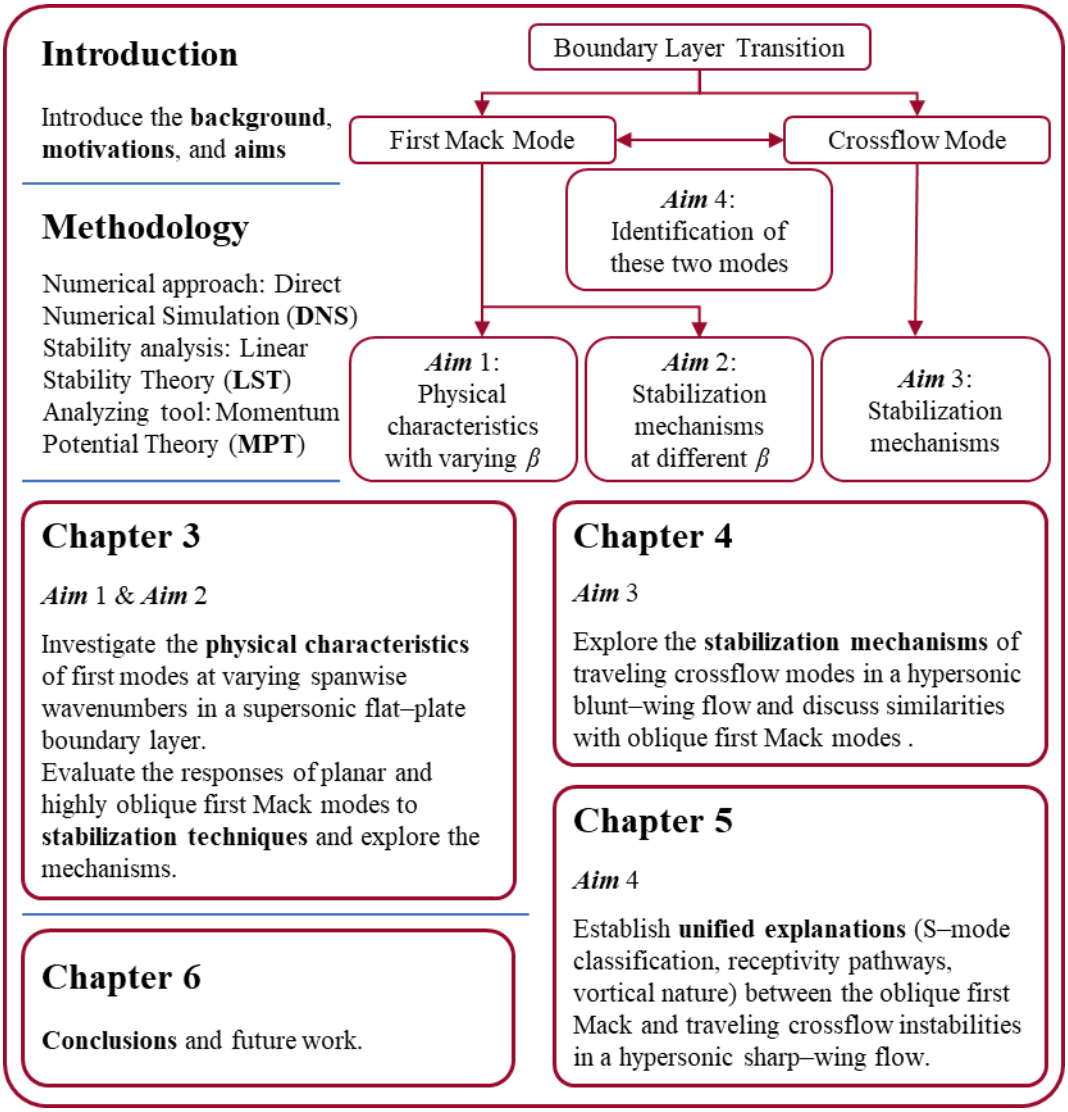

Figure 1-1 A flowchart depicting the structure of the thesis.

Chapter 2 describes the numerical and analytical tools employed in this study, including direct numerical simulation (DNS), linear stability theory (LST), and momentum potential theory (MPT).

Chapter 3 addresses ***Aims*** 1 and 2. First Mack modes in a Mach 4.5 flat-plate boundary layer are systematically investigated. The evolution of their physical properties across varying spanwise wavenumbers is first examined, followed by an analysis of their divergent responses to control techniques and the associated stabilization mechanisms at different spanwise wavenumbers.

Chapter 4 addresses ***Aim*** 3. The stabilization mechanisms of traveling crossflow modes are investigated in a Mach 6 blunt swept-wing boundary layer.

Chapter 5 addresses ***Aims*** 4. The receptivity of first Mack and crossflow modes to 3D slow acoustic and vorticity waves is investigated over a Mach 4.5 sharp wing. Detailed analysis of the receptivity pathways reveals fundamental consistencies between first Mack and crossflow modes.

Chapter 6 concludes the thesis by summarizing the key findings and providing a brief discussion on the possible future studies emerging from the observations reported in this work.

Chapter 2 Methodology

2.1. Direct Numerical Simulation

The direct numerical simulation is used for simulating the steady baseflows and unsteady perturbation fields in the thesis, which is governed by the 3D compressible Navier-Stokes equations for a calorically perfect gas with appropriate boundary and initial conditions. The equations in a curvilinear coordinate (ξ, ς, ζ) can be written in the conservation form:

$$\frac{\partial \boldsymbol{Q}}{\partial t}+\frac{\partial \boldsymbol{E}}{\partial \xi}+\frac{\partial \boldsymbol{F}}{\partial \varsigma}+\frac{\partial \boldsymbol{G}}{\partial \zeta}=0 \tag{2.1}$$

where t is time, $\boldsymbol{Q}$ is the vector of conservative variables, $\boldsymbol{E}$, $\boldsymbol{F}$, and $\boldsymbol{G}$ are the flux vectors in each direction. The projection of these vectors from the curvilinear coordinate (ξ, ς, ζ) to the Cartesian coordinate (x, y, z) is:

$$\begin{aligned} &\boldsymbol{Q}=J\boldsymbol{Q}_c && \boldsymbol{E}=J\left(\boldsymbol{E}_c\frac{\partial \xi}{\partial x}+\boldsymbol{F}_c\frac{\partial \xi}{\partial y}+\boldsymbol{G}_c\frac{\partial \xi}{\partial z}\right) \\ &\boldsymbol{F}=J\left(\boldsymbol{E}_c\frac{\partial \varsigma}{\partial x}+\boldsymbol{F}_c\frac{\partial \varsigma}{\partial y}+\boldsymbol{G}_c\frac{\partial \varsigma}{\partial z}\right) && \boldsymbol{G}=J\left(\boldsymbol{G}_c\frac{\partial \zeta}{\partial x}+\boldsymbol{G}_c\frac{\partial \zeta}{\partial y}+\boldsymbol{G}_c\frac{\partial \zeta}{\partial z}\right) \end{aligned} \tag{2.2}$$

here $J=|\partial(x,y,z)/\partial(\xi,\varsigma,\zeta)|$ is the transformation Jacobian matrix. Vectors in the Cartesian coordinate system are:

$$\boldsymbol{Q}_c=\begin{Bmatrix}\rho\\ \rho u\\ \rho v\\ \rho w\\ e\end{Bmatrix} \tag{2.3}$$

$$\boldsymbol{E}_c=\begin{Bmatrix}\rho u\\ \rho u^2+p-\tau_{xx}\\ \rho uv-\tau_{xy}\\ \rho uw-\tau_{xz}\\ u(e+p)-u\tau_{xx}-v\tau_{xy}-w\tau_{xz}+q_x\end{Bmatrix} \tag{2.4}$$

$$\boldsymbol{F}_c = \begin{Bmatrix} \rho v \\ \rho uv - \tau_{xy} \\ \rho v^2 + p - \tau_{yy} \\ \rho vw - \tau_{yz} \\ v(e+p) - u\tau_{xy} - v\tau_{yy} - w\tau_{yz} + q_y \end{Bmatrix} \tag{2.5}$$

$$\boldsymbol{G}_c = \begin{Bmatrix} \rho w \\ \rho uw - \tau_{xz} \\ \rho vw - \tau_{yz} \\ \rho w^2 + p - \tau_{zz} \\ w(e+p) - u\tau_{xz} - v\tau_{yz} - w\tau_{zz} + q_z \end{Bmatrix} \tag{2.6}$$

where ρ is the density, u, v, and w are the components of velocity, e is the specific total energy, defined as

$$e = \frac{p}{\gamma - 1} + \frac{\rho\left(u^2 + v^2 + w^2\right)}{2} \tag{2.7}$$

The specific heat ratio $\gamma = 1.4$, p is pressure. The stress tensor τ and heat flux q are

$$\begin{aligned} \tau_{xx} &= 2\mu\frac{\partial u}{\partial x} - \frac{2}{3}\mu\left(\frac{\partial u}{\partial x} + \frac{\partial v}{\partial y} + \frac{\partial w}{\partial z}\right) \\ \tau_{yy} &= 2\mu\frac{\partial v}{\partial y} - \frac{2}{3}\mu\left(\frac{\partial u}{\partial x} + \frac{\partial v}{\partial y} + \frac{\partial w}{\partial z}\right) \\ \tau_{zz} &= 2\mu\frac{\partial w}{\partial x} - \frac{2}{3}\mu\left(\frac{\partial u}{\partial x} + \frac{\partial v}{\partial y} + \frac{\partial w}{\partial z}\right) \end{aligned} \tag{2.8}$$

$$\begin{aligned} \tau_{xy} &= \tau_{yx} = \mu\left(\frac{\partial u}{\partial y} + \frac{\partial v}{\partial x}\right) \\ \tau_{xz} &= \tau_{zx} = \mu\left(\frac{\partial u}{\partial z} + \frac{\partial w}{\partial x}\right) \\ \tau_{yz} &= \tau_{zy} = \mu\left(\frac{\partial v}{\partial z} + \frac{\partial w}{\partial y}\right) \end{aligned} \tag{2.9}$$

$$q_x = -\frac{\mu}{Pr(\gamma-1)Ma_\infty^2}\frac{\partial T}{\partial x}$$
$$q_y = -\frac{\mu}{Pr(\gamma-1)Ma_\infty^2}\frac{\partial T}{\partial y} \tag{2.10}$$
$$q_z = -\frac{\mu}{Pr(\gamma-1)Ma_\infty^2}\frac{\partial T}{\partial z}$$

T is the temperature, Ma_∞ is the freestream Mach number, the subscript ∞ denotes freestream quantities. The Prandtl number $Pr = 0.72$. The dynamic viscosity coefficient μ is calculated by Sutherland's law. The governing equations are closed by the equation of state of an ideal gas. The density ρ, velocity (u, v, w), temperature T, and pressure p are made dimensionless by the freestream parameters ρ_∞^*, U_∞^*, T_∞^*, and $\rho_\infty^* U_\infty^{*2}$. Here, U_∞^* refers to the freestream velocity magnitude. The symbol * denotes dimensional variables. The fifth-order upwind scheme is employed to discretize the inviscid flux derivatives. The second-order central difference scheme is used to discretize viscous terms. The lower-upper symmetric Gauss-Seidel (LUSGS) scheme is employed to resolve the steady flow field, and a third-order total variation diminishing Runge-Kutta scheme is used for unsteady temporal integration.

2.2. Linear Stability Analysis

Spatial LST is used to capture the unsteady modes in the boundary layers. The vector $\boldsymbol{Q}$ is decomposed into a 1D steady solution and an unsteady perturbation under the assumption of a local-parallel flow:

$$\boldsymbol{Q}(x,y,z,t) = \bar{\boldsymbol{Q}}(y) + \boldsymbol{Q}'(x,y,z,t) \tag{2.11}$$

where $\bar{\boldsymbol{Q}}$ is the baseflow variable vector, $\boldsymbol{Q}'$ represents the perturbation. After linearization, the perturbation term in normal-model form is written as follows:

$$\boldsymbol{Q}'(x,y,z,t) = \hat{\boldsymbol{Q}}(y)\exp(i\alpha x + i\beta z - i\omega t) + c.c. \tag{2.12}$$

$\hat{\boldsymbol{Q}}$ is the eigenfunction in the wall-normal direction, α is the streamwise wavenumber, β is the spanwise wavenumber, ω is the angular frequency and *c.c.* is the complex conjugate. For spatial analysis, α is considered to be complex with real (subscript r) and imaginary parts (subscript i). $-\alpha_i$ represents the spatial growth rate of unstable modes. The spatial wavenumbers α and β are normalized by $1/L^*$, while the circular frequency ω is normalized by U_∞^*/L^*, where L^* is the reference length and will be specified in the following sections. The transformations between the dimensional frequency F^*, the dimensionless angular frequency ω, the dimensional spanwise wavelength λ_z^*, and the

dimensionless spanwise wavenumber β are:

$$\omega = \frac{2\pi \times F^* \times L^*}{U_\infty^*} \quad \beta = \frac{2\pi \times L^*}{\lambda_z^*} \tag{2.13}$$

The LST incorporating local curvature effects κ is utilized for spatial analysis. The Lamé coefficients are $h_1 = 1 + \kappa y$ and $h_2 = h_3 = 1$. Substituting equation (2.12) into the linearized compressible Navier-Stokes equations forms the governing equation:

$$\bar{\boldsymbol{C}}\hat{\boldsymbol{Q}} = \left(\alpha_r + i\alpha_i\right)\hat{\boldsymbol{Q}} \tag{2.14}$$

where $\bar{\boldsymbol{C}}$ is the Jacobian matrix composed of both the inviscid and viscous fluxes and is expressed in terms of baseflow quantities. The detailed formulations can be found in previous studies[109,110]. The boundary conditions for this eigenvalue problem are:

$$\begin{cases} \hat{u} = \hat{w} = \hat{T} = 0, \hat{v} = A\hat{p}, & \left| y = 0 \right. \\ \hat{u} = \hat{v} = \hat{w} = \hat{T} = 0, & \left| y \to \infty \right. \end{cases} \tag{2.15}$$

where $A = \left|A\right| e^{i\theta}$ is the complex wall acoustic admittance, $|A|$ denotes the admittance magnitude and θ denotes the admittance phase. For a solid smooth wall, $|A| = 0$. For porous coatings, the impedance model proposed by Zhao et al.[93] is used to calculate A. The detailed relationship between coating geometric parameters (cavity height H, half-width b, periodic s_c) and A is:

$$A = \frac{1}{Z} = \frac{1}{\rho c}\frac{R_{00} - 1}{R_{00} + 1} \tag{2.16}$$

where Z is the impedance, c is the sound velocity, R_{00} is the reflection coefficient of zeroth-order diffraction:

$$R_{00} = 1 + \frac{2j\tan(k_h H)(\rho/\tilde{\rho})\varphi(k_h/k_0)}{1 - j\tan(k_h H)(\rho/\tilde{\rho})\varphi\sum_{r,q=-\infty}^{+\infty}(k_h S_{rq}^2 / \sqrt{k_0^2 - (2r\pi/s_c)^2 - (2q\pi/s_c)^2})} \tag{2.17}$$

The definitions of parameters are the same as in Ref. [93].

2.3. Momentum Potential Theory

Doak's MPT approach decomposes fluctuations into vortical, acoustic, and thermal components. The momentum density $\boldsymbol{m}(\equiv\rho\boldsymbol{u})$ is chosen as the primary dependent vector field to be decomposed. By Helmholtz's theorem, the momentum density field can be expressed as:

$$\boldsymbol{m} \equiv \rho \boldsymbol{u} = \boldsymbol{m}_{\boldsymbol{B}} - \nabla\psi, \nabla \cdot \boldsymbol{m}_{\boldsymbol{B}} = 0 \tag{2.18}$$

where $\boldsymbol{m}_{\boldsymbol{B}}$ is the rotational vortical part and $-\nabla\psi$ is the irrotational component written in the form of a potential function. For a time-stationary flow field, an instantaneous flow quantity can be divided into a mean part (denoted by an overbar) and a fluctuation part (denoted by a prime):

$$\bar{\boldsymbol{m}} = \bar{\boldsymbol{m}}_{\boldsymbol{B}} - \nabla\bar{\psi}, \ \boldsymbol{m}' = \boldsymbol{m}'_{\boldsymbol{B}} - \nabla\psi' \tag{2.19}$$

The mean continuity equation and the fluctuation continuity equation can be expressed as follows:

$$\nabla \cdot \bar{\boldsymbol{m}} = 0, \ \frac{\partial \rho'}{\partial t} + \nabla \cdot \boldsymbol{m}' = 0 \tag{2.20}$$

By substituting equation (2.19) into equation (2.20), the mean scalar potential $\bar{\psi}$ is zero. Consequently, a form of Poisson's equation is derived for the scalar potential of the fluctuation component:

$$\frac{\partial \rho'}{\partial t} = \nabla^2 \psi' \tag{2.21}$$

For a single-chemical-component continuum in thermal equilibrium, the density ρ can be defined as a function of the thermodynamic pressure p and entropy S:

$$\frac{\partial \rho'}{\partial t} = \frac{\partial \rho}{\partial p}\frac{\partial p'}{\partial t} + \frac{\partial \rho}{\partial S}\frac{\partial S'}{\partial t}, \ \frac{\partial \rho}{\partial p} = \frac{1}{a^2} = \frac{1}{\gamma RT}, \ \frac{\partial \rho}{\partial S} = -\frac{(\gamma - 1)\rho}{\gamma R} \tag{2.22}$$

Thus, the scalar potential of the fluctuation component is divided into acoustic part and thermal part:

$$\psi' = \psi'_A + \psi'_T, \frac{1}{\gamma RT}\frac{\partial p'}{\partial t} = \nabla^2 \psi'_A, -\frac{(\gamma - 1)\rho}{\gamma R}\frac{\partial S'}{\partial t} = \nabla^2 \psi'_T \tag{2.23}$$

The fluctuation momentum density $\boldsymbol{m}'$ is finally decomposed into the vortical component $\boldsymbol{m}'_{\boldsymbol{B}}$, the acoustic component $\boldsymbol{m}'_{\boldsymbol{A}}$, and the thermal component $\boldsymbol{m}'_{\boldsymbol{T}}$ as

$$\boldsymbol{m}' = \boldsymbol{m}'_{\boldsymbol{B}} + \boldsymbol{m}'_{\boldsymbol{A}} + \boldsymbol{m}'_{\boldsymbol{T}}, \ \boldsymbol{m}'_{\boldsymbol{A}} = -\nabla\psi'_A, \ \boldsymbol{m}'_{\boldsymbol{T}} = -\nabla\psi'_T \tag{2.24}$$

These MPT components have different physical natures. The vortical component $\boldsymbol{m}'_{\boldsymbol{B}}$ is isobaric and isentropic. The acoustic component $\boldsymbol{m}'_{\boldsymbol{A}}$ is irrotational and isentropic. The thermal component $\boldsymbol{m}'_{\boldsymbol{T}}$ is irrotational and isobaric.

In this thesis, the MPT decomposition serves as a post-processing mathematical framework for characterizing perturbation fields. The acoustic, vortical, and thermal

components are inherently coupled for a certain instability. MPT can reveal fundamental mechanistic distinctions across different instabilities by clarifying the equilibrium state. It can also provide interpretive insights by quantifying disruptions to the equilibrium under control techniques, thereby revealing mechanistic differences between control approaches.

Chapter 3 Stabilization Mechanisms of First Mack Mode

As mentioned in the introduction, the physical nature of the first Mack mode is closely related to its wave angle, whereas a systematic comparative analysis of its dynamical behavior under different wave angles remains lacking. This chapter examines the first Mack modes in a Mach 4.5 flat-plate boundary layer. Specifically, their distinct physical natures under varying spanwise wavenumbers will be discussed, followed by their different responses to stabilization techniques.

3.1. Problem Description

This study investigates the first Mack mode in a Mach 4.5 flat-plate boundary layer with identical frequencies but varying spanwise wavenumbers, as illustrated in Figure 3-1. The flow parameters align with those in Ref. [111]: a free-stream temperature of 65.15 K, a unit Reynolds number of 7.2×10^{6} m^{-1}, and a wall temperature of 260.6 K. The most unstable oblique first mode parameters reported in Ref. [111] are adapted as the baseline case, whose frequency F^* = 21 kHz, spanwise wavelength $\lambda_z^* = 0.016$ m (corresponding to ω = 0.547 and β = 1.18). The computational domain for the DNS of the supersonic boundary layer is set up between x^* = 0.4 and 0.8 m. The inlet boundary layer thickness at $x_{in}^* = 0.4$ m is $\delta_{in}^* = 3.016\times10^{-3}$ m, which also serves as the reference length. The wall-normal length of the domain is set to 0.1 m, while the spanwise length is determined by the spanwise wavenumber of each case. Periodic boundary conditions are applied along the spanwise direction, the outflow boundary conditions are used at the top and outlet of the computational domain. The wall is modeled as iso-thermal and non-penetrative. Stabilization techniques are applied within x^* = 0.6 and 0.8 m and will be introduced in Sec. 3.3. The first mode is introduced via a slot of wall-normal blowing-suction, defined as a velocity perturbation:

$$v(x, y=0, z, t) = A_p f\left(x\right) g\left(z\right) h\left(t\right) \tag{3.1}$$

where:

$$\begin{aligned} &f\left(x\right) = 4\sin\theta(1-\cos\theta)/\sqrt{27} \\ &\theta = 2\pi\left(x^* - x_{start}^*\right)\Big/\left(x_{end}^* - x_{start}^*\right), x_{start}^* \le x^* \le x_{end}^* \\ &g\left(z\right) = \cos\left(2\pi z^*/\lambda_z^*\right) \\ &h\left(t\right) = \sin\left(2\pi F^* t^*\right) \end{aligned} \tag{3.2}$$

where A_p is the dimensionless magnitude of disturbances, set to 10^{-6}, $x^*_{start} = 0.412\text{m}$ and $x^*_{end} = 0.44\text{m}$ are the beginning and end of the blowing-suction slot.

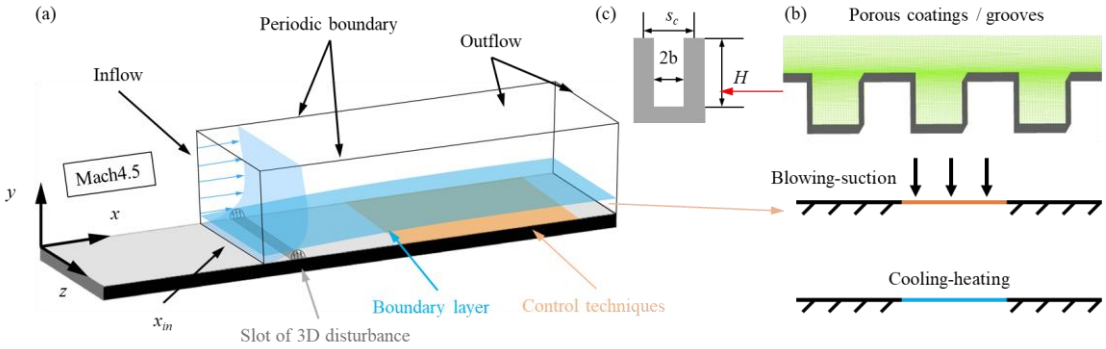

Figure 3-1 Schematic of the problem formulation: (a) supersonic boundary-layer flow over a flat plate, (b) stabilization techniques, and (c) geometric parameters for cavities.

The numerical codes and grid independence are systematically validated in Figure 3-2 with the baseline case. The coarse grid comprises 781 × 201 × 21 points, while the fine grid has 1171 × 301 × 31 points. Figure 3-2(a) compares the velocity and temperature profiles at $x^* = 0.6$ m and $x^* = 0.8$ m, and Figure 3-2(b) presents the growth rates of the oblique first mode from DNS and LST under both grids.

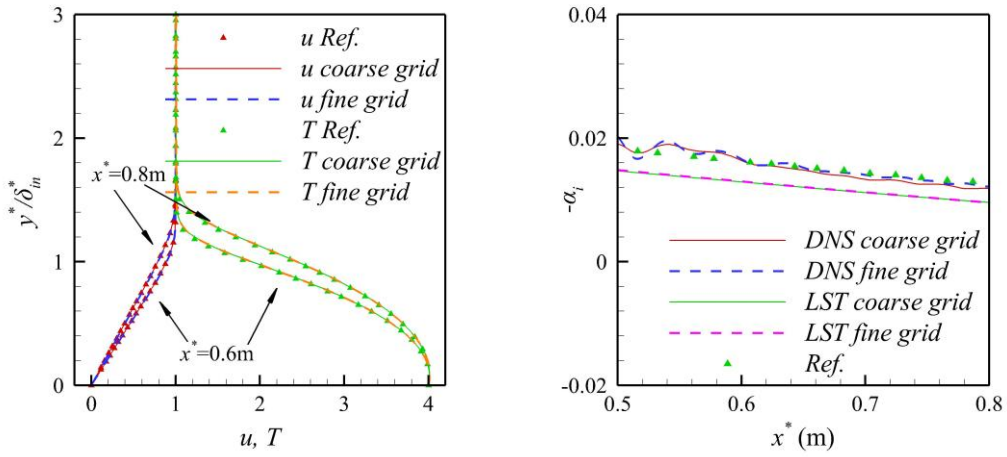

(a) baseflow profiles at $x^* = 0.6$ m and $x^* = 0.8$ m (b) spatial growth rate under coarse and fine grids

Figure 3-2 Code and grid-independence verification for the baseline case.

The nondimensional spatial growth rate of the DNS data is calculated by:

$$-\alpha_i = \frac{L^*}{u'_{\max}} \frac{du'_{\max}}{dx^*} \tag{3.3}$$

L^* is the reference length and is equal to δ_{in}^* in this chapter. The results demonstrate excellent agreement between the coarse and fine grids for both the base flow and growth rates, with strong consistency against reference data, confirming the reliability of the numerical methodology and code. The coarse grid will be utilized for further simulations.

3.2. Acoustic–Vortical Evolution Mechanisms of First Mack Mode

3.2.1. Linear stability theory results

Figure 3-3 summarizes the LST results at $x^* = 0.7$ m. As shown in Figure 3-3(a), both the streamwise wavenumber α_r and growth rate α_i initially increase and then decrease with the spanwise wavenumber β. The maximum streamwise wavenumber occurs at $\beta = 0.7$, while the peak growth rate is observed at $\beta = 1.0$. Beyond $\beta = 1.9$, the first mode stabilizes at this frequency. The non-monotonic relationship between α_i and β consists with the finding of Mack[8]. Figure 3-3(b)–(d) illustrate the eigenfunctions of flow variables (u', v', w', p', T') under different β, normalized by their respective maximum values. Dashed lines indicate the location of the GIP (where $d\left(\rho du/dy\right)/dy = 0$), while arrows show the direction of eigenfunction variation as β increases. In the planar first mode ($\beta = 0$), the u' profile exhibits an obvious double-peak structure, which aligns with Liu's result[46] that dual peaks in u' profiles are a sign of the first mode. With β increasing, the peak u' perturbation beyond the GIP gradually diminishes, while those beneath the GIP and near the solid wall decrease in magnitude and shift toward the wall. A new peak emerges at the GIP, eventually dominating throughout the boundary layer in large-β cases ($\beta \geq 1.6$). This evolution results in the u' profile going through "dual peaks–triple peaks–single peak" configurations. The v' profile also displays two peaks at $\beta = 0$, with the peak beyond the GIP being dominant. Previous studies on second Mack modes have observed similar dual-peak configurations in the v' profile[103], but with the lower peak being dominant. This contrast aligns with Liang's viewpoint[24] that the first mode is an "off-wall" mode. As β increases, the v' peak beneath the GIP shifts toward the wall and vanishes, while a secondary peak forms near the GIP, implying off-wall motions. The w' profiles remain nearly unchanged across β. The p' profiles exhibit a shift of the peak value from the wall to the GIP. The T' profiles show small changes, except for the vanishing of the

near-wall peak. Collectively, as β increases, all perturbation components of the first mode concentrate near the GIP, reinforcing the growing importance of off-wall motion. The evolution of these patterns will be further examined using DNS results.

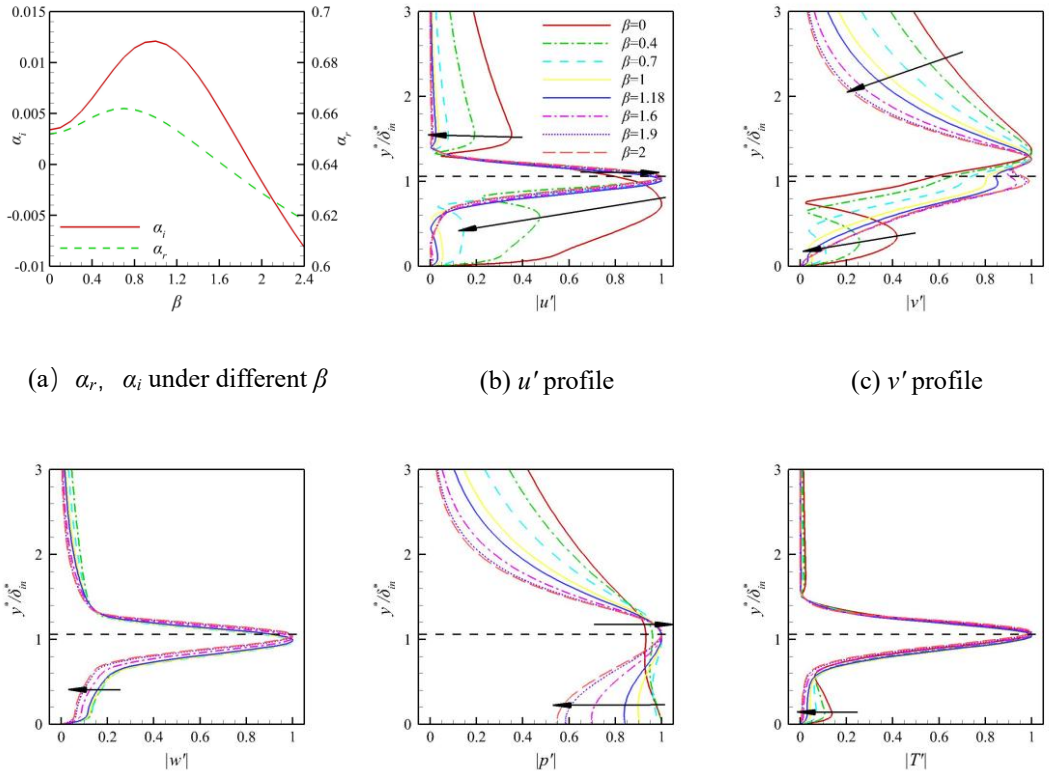

(a) α_r, α_i under different β (b) u' profile (c) v' profile

(d) w' profile (e) p' profile (f) T' profile

Figure 3-3 α_r and α_i eigenfunctions at $x^* = 0.7$ m under different β. Legends from (b) to (f) are the same.

3.2.2. Direct numerical simulation results

The following analysis presents the flow fields at the $z^* = 0$ m cross-section obtained from DNS, as depicted in Figure 3-4. Here, p' is represented using contour plots. As previously demonstrated, u' and v' exhibit significant changes with increasing β, while w' shows minimal differences, implying the alterations in streamwise motion patterns may be the primary driver of property changes in first modes. Consequently, to illustrate particle motion patterns of the unstable mode, perturbation streamlines derived from u'-v' velocity perturbations are superimposed. White dashed lines mark the sonic line positions, and dark gray dashed lines indicate the GIP.

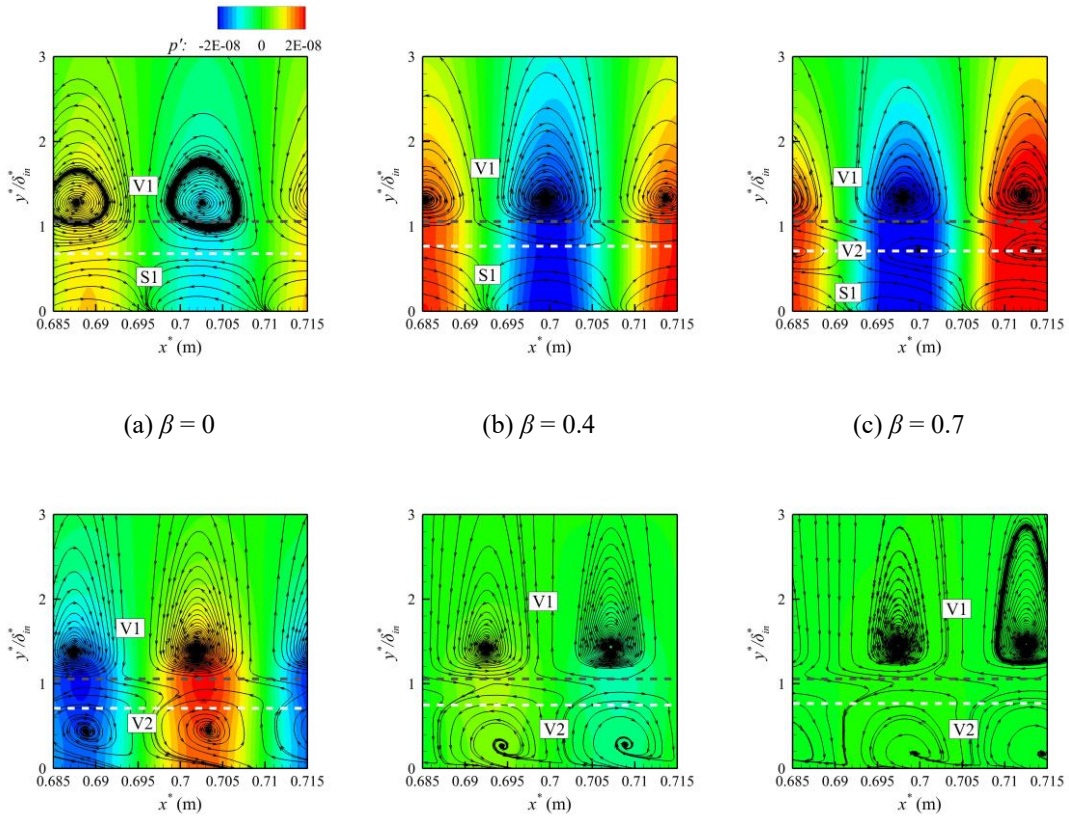

(a) $\beta = 0$ (b) $\beta = 0.4$ (c) $\beta = 0.7$

(d) $\beta = 1.18$ (e) $\beta = 1.6$ (f) $\beta = 2$

Figure 3-4 p' contours and perturbation streamlines under different β.

From contour plots, the perturbation amplitudes roughly align with the growth rate trend predicted by LST, i.e., the maximum p' happens between $\beta = 0.7$ and 1.18. In weakly oblique cases ($\beta = 0$ and 0.4), two distinct regions of the perturbation field can be observed beyond and beneath the sonic line: in the upper regions, perturbation streamlines are featured as counter-rotating vortex pairs (V1), while the lower regions are dominated by oscillatory sound waves (S1) trapped between the sonic line and the wall. These dual-regime behaviors closely resemble the second mode, described as "trapped-acoustic" waves. A critical transition happens at $\beta = 0.7$, characterized as the emergence of a new set of vortices (V2) centered on the sonic line. This shift of motion patterns marks the transition of physical properties from sound-dominant to vortex-dominant. For highly oblique cases ($\beta > 0.7$), the new vortex pairs (V2) grow in size and shift toward the wall, suppressing the original near-wall trapped waves (S1). The perturbation structure transitions to a dual-vortex pair configuration (V1 and V2) separated by the GIP, signifying a vortex-dominant mechanism for highly oblique first modes, corroborating classifications of the oblique first mode as a vortical mode[22].

3.2.3. Momentum potential theory results

The momentum density fields obtained from DNS are decomposed using MPT. Figure 3-5 illustrates the instantaneous snapshots of acoustic, vortical, and thermal components in representative cases (β = 0, 0.7, 1.18). The black solid lines indicate the GIP.

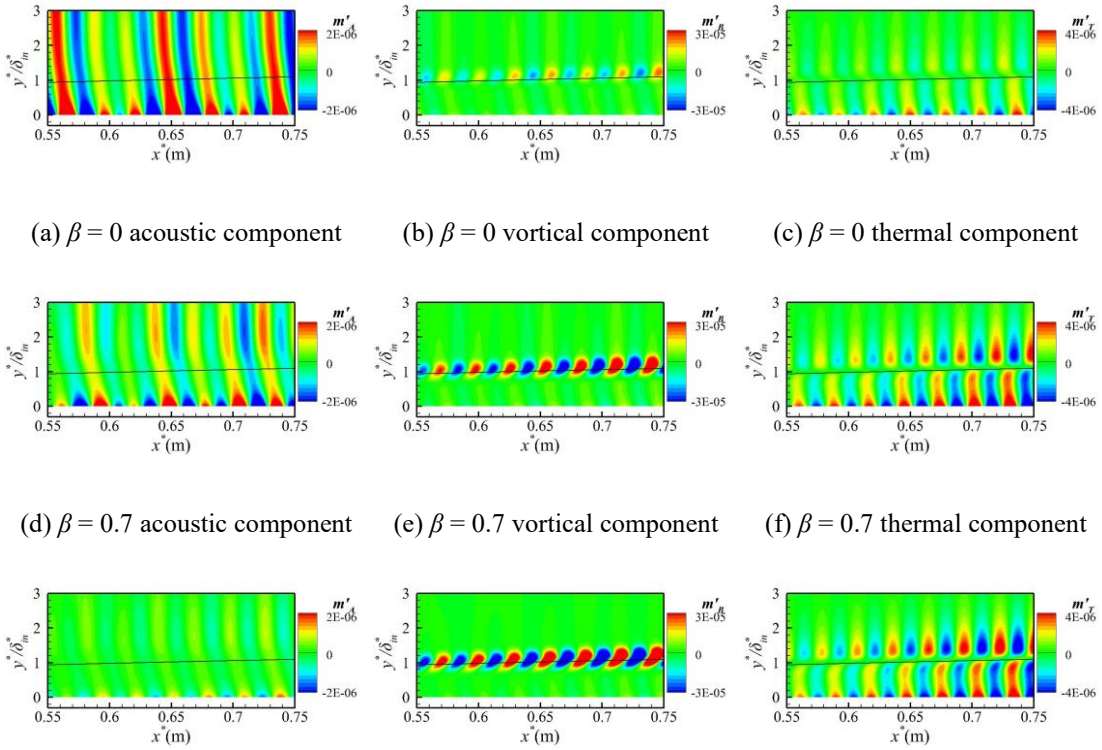

(a) β = 0 acoustic component (b) β = 0 vortical component (c) β = 0 thermal component

(d) β = 0.7 acoustic component (e) β = 0.7 vortical component (f) β = 0.7 thermal component

(g) β = 1.18 acoustic component (h) β = 1.18 vortical component (i) β = 1.18 thermal component

Figure 3-5 Instantaneous snapshots of MPT components when β = 0, 0.7, 1.18. unit: kg/(m^{2}s).

As β increases, $\boldsymbol{m'}_A$ decreases in magnitude, $\boldsymbol{m'}_B$ and $\boldsymbol{m'}_T$ intensify. In all cases, $\boldsymbol{m'}_A$ remains concentrated near the wall, while $\boldsymbol{m'}_B$ dominates near the GIP. $\boldsymbol{m'}_T$ initially exhibiting near-wall behavior, shifts toward the GIP as β increases.

Figure 3-6 presents the normalized MPT components for the three representative cases, where each component is normalized by the corresponding local maximum momentum density. Black dashed lines indicate the GIP. $\boldsymbol{m'}_A$ is significant near the wall, but diminishes with increasing β. In the highly oblique first mode, $\boldsymbol{m'}_A$ contributes less than 2% of the total momentum density. $\boldsymbol{m'}_B$ becomes increasingly concentrated near the GIP with increasing β, while its contribution away from the GIP

declines, indicating a reinforcement of their vortical nature. $\boldsymbol{m'}_T$ makes up a smaller proportion during this process. The mechanism evolution of the first mode from an acoustic mode to an "off-wall" vortical mode is clearly demonstrated. As shown in Figure 3-3(a), the most unstable first mode occurs at β = 1.0, hereby categorized as a highly oblique first mode with dominantly vortical characteristics. Consequently, laminar control strategies targeting vortical instabilities hold greater promises for engineering applications in first-mode-dominant scenarios.

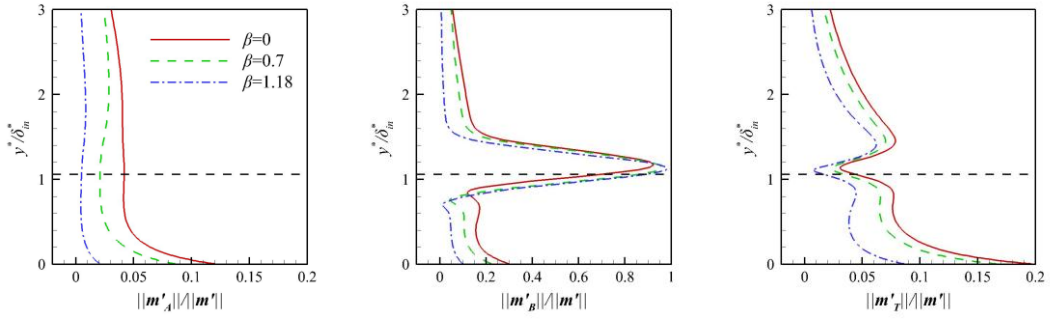

(a) acoustic component (b) vortical component (c) thermal component

Figure 3-6 Normalized MPT components at x^* = 0.7 m when β = 0, 0.7, 1.18.

3.3. Stabilization of First Mack Mode

3.3.1. Wall cooling-heating

Wall cooling-heating is applied between x^* = 0.6 m and x^* = 0.8 m, the wall temperatures T_w are set to 2 (cooling), 3 (cooling), 4 (baseline), and 5 (heating). Baseflow profiles at x^* = 0.6 m are illustrated in Figure 3-7. The sonic line positions ($u = c_r - a$) are marked with the horizontal color lines in Figure 3-7(a). A vertical black dashed line is drawn at 0 to facilitate identifying the position of GIPs in Figure 3-7(b). Notably, sonic line positions remain nearly identical for 2D and 3D first modes due to their comparable α_r values at these two β. Reducing wall temperature yields thinner boundary layers, shifting the sonic lines and GIPs toward the wall. A second GIP emerges in the wall cooling case where $u < 1 - 1/M_e$. This second GIP moves outwards while the primary GIP shifts toward the wall under lower T_w. The first mode can be stabilized when both GIPs disappear at critically low T_w, as described by Malik[79].

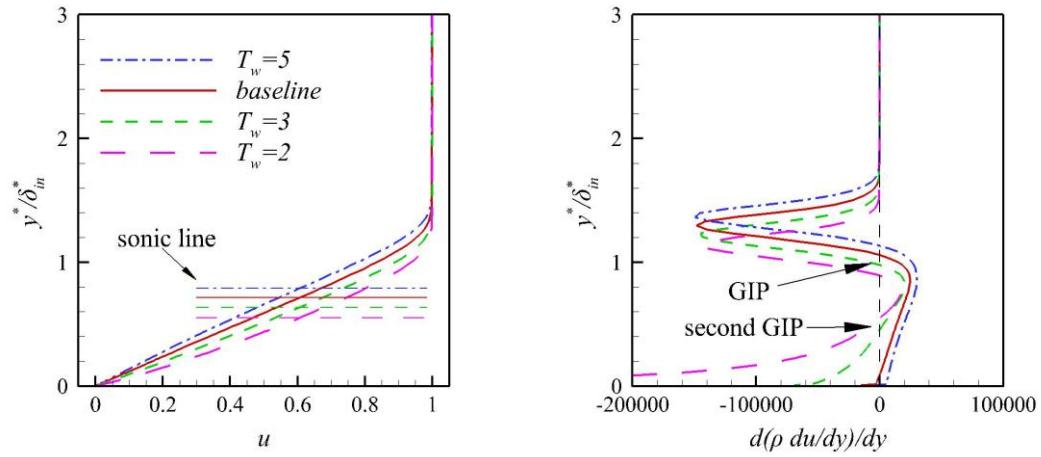

(a) u profiles and sonic line positions (b) GIPs

Figure 3-7 Baseflow profiles at x^* = 0.7 m for wall cooling-heating cases.

The growth of 2D and 3D first modes is quantified by the maximum streamwise velocity perturbation amplitudes at each streamwise station, as depicted in Figure 3-8. The beginning and end of the wall cooling-heating zone are marked by the vertical black dashed lines. Wall cooling exhibits stabilizing effects on first modes, while wall heating exerts a destabilizing influence. The stabilization effect is marginal for 2D modes but pronounced for 3D modes. This disparity likely originates from inherent differences in the physical mechanisms at different β.

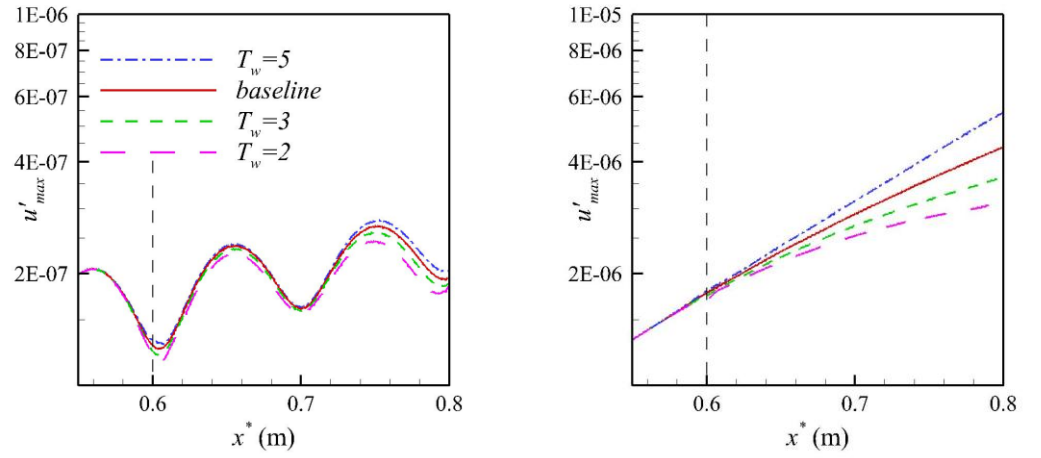

(a) β = 0 (b) β = 1.18

Figure 3-8 The maximum u' in wall cooling-heating cases.

Figure 3-9 illustrates the $u'-v'$ perturbation streamlines when T_w = 2. The red dashed lines represent the GIP, the dark dashed lines mark the sonic line, and the red dashed-dotted lines represent the second GIP generated by wall cooling. For the 2D mode, the motion pattern where the sonic line splits the upper vortex pair (V1) and lower trapped sound wave (S1) persists under wall cooling. Both V1 and S1 shift marginally toward the wall, consistent with the sonic line displacement, which is likely related to the marginal stabilization effect on the 2D first mode. The 3D first mode exhibits a dual-vortex pair configuration (V1 and the lower vortex pair (V2)) partitioned by the primary GIP.

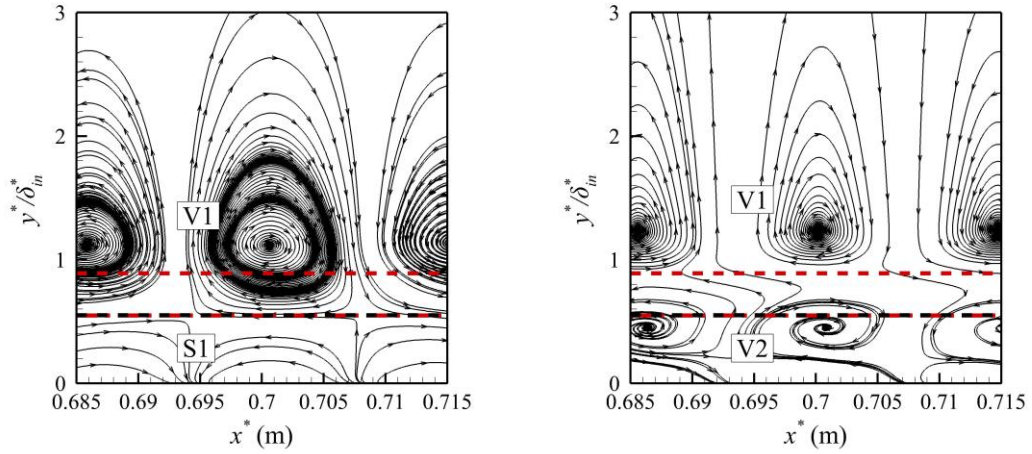

(a) β = 0 (b) β = 1.18

Figure 3-9 Perturbation streamlines in case T_w = 2.

3.3.2. Wall blowing-suction

Wall blowing-suction is also applied between x^* = 0.6 m and x^* = 0.8 m, with the intensity quantified by the suction coefficient A_s, defined by the wall mass flux:

$$A_s = -\rho_w v_w \tag{3.4}$$

where ρ_w and v_w denote wall density and wall-normal velocity, respectively. For the suction case, A_s = +0.0005, while A_s = −0.0005 is employed for the wall-blowing case. Baseflow profiles are plotted in Figure 3-10. The sonic lines and GIPs are depicted in a pattern similar to Figure 3-7. Wall suction has a similar effect to wall cooling: the sonic line and GIP shift toward the wall. These displacements are more pronounced in wall blowing-suction cases than in cooling-heating cases, with wall suction also generating

the second GIP, which is nearly at the same height as the sonic line.

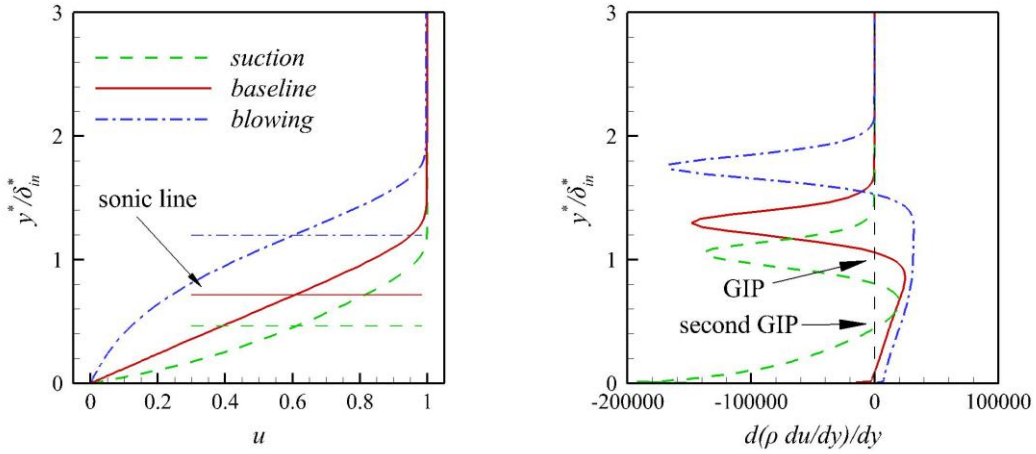

(a) u profiles and sonic line positions (b) GIPs

Figure 3-10 Baseflow profiles at $x^* = 0.7$ m for wall blowing-suction cases.

The evolution of maximum streamwise velocity perturbations $u'_{\max}$ for 2D and 3D first modes under wall blowing-suction is plotted in Figure 3-11. Steady wall suction stabilizes both modes, whereas blowing exerts destabilizing effects. Despite equal A_s magnitudes, wall blowing produces stronger destabilization effects than wall suction, which is likely attributed to its pronounced modifications to the baseflow. The 2D first mode is also less sensitive to the stabilization effect of steady wall suction.

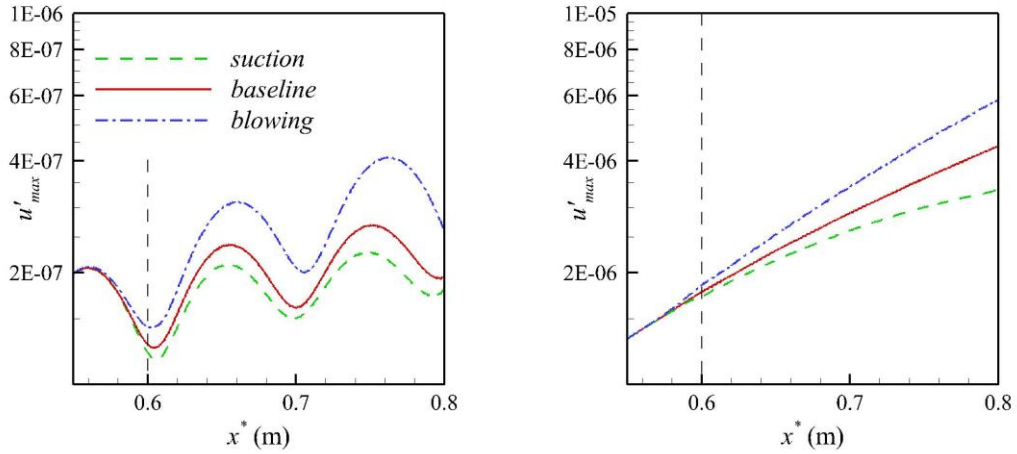

(a) $\beta = 0$ (b) $\beta = 1.18$

Figure 3-11 The maximum u' in wall blowing-suction cases.

The perturbation streamlines for wall-suction cases are illustrated in Figure 3-12. Both GIPs and sonic lines are marked with dashed lines in a pattern similar to those in Figure 3-9. This strong wall suction does not fundamentally alter the motion patterns of first modes: S1 in the 2D first mode case and V2 in the oblique first mode case persist despite the obvious downward displacement of the sonic line and the GIP. However, S1 and V2 undergo significant wall-normal compression under wall suction.

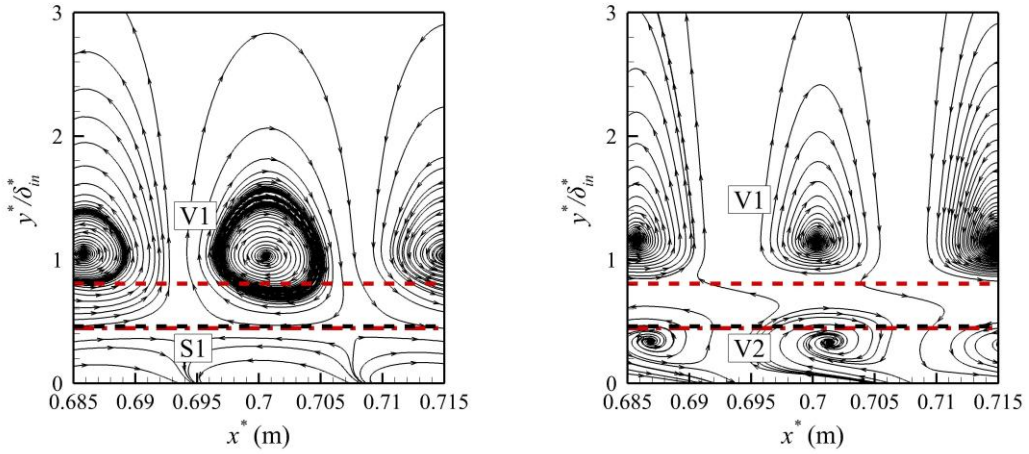

(a) $\beta = 0$ (b) $\beta = 1.18$

Figure 3-12 Perturbation streamlines in wall-suction cases.

3.3.3. Porous coatings

Aiming at stabilizing the proposed first mode, porous coatings with different admittance phases θ (0.5π, 1π, 1.5π) are designed based on the admittance equation proposed by Zhao et al.[93], and their effects on first modes are predicted using LST. Table 3-1 summarizes the coating geometry parameters, admittance values and corresponding growth rates for the planar first mode and the highly oblique first mode ($\beta = 1.18$) at $x^* = 0.7$ m. The coatings are labeled according to their designed admittance phase. Stabilizing or destabilizing effects relative to the no-coating case are indicated alongside the LST growth rates. According to LST predictions, porous coatings marginally stabilize the first mode when $\theta = 0.5\pi$, while destabilizing the first mode under larger admittance phases. The destabilization effect is much larger in planar cases than that in oblique cases.

These coatings are applied to the flat plate, as depicted in Figure 3-1(b, c). For the porous coatings, the DNS grid resolutions for each real cavity are: $\theta = 1\pi$ (9 × 81), $\theta =$

0.5π (9 × 41), and θ = 1.5π (9 × 101). The grid resolution of the porous coatings is verified using the coarsest case, θ = 1.5π, by increasing the grid density of each cavity to 17 × 201. The instantaneous wall pressure perturbations for oblique first modes under these two mesh conditions are depicted in Figure 3-13. The wall pressure distributions closely align, confirming that the current grid resolution is sufficient to capture the effects of the porous coatings.

Table 3-1 Porous coating parameters and growth rates at x^* = 0.7 m.

	$\theta = 1\pi$	$\theta = 0.5\pi$	$\theta = 1.5\pi$
b /m	2×10^{-4}	3×10^{-4}	9×10^{-4}
H /m	5×10^{-3}	1×10^{-3}	5.14×10^{-3}
aspect ratio	0.08	0.6	0.35
porosity	0.5	0.8	0.5
Admittance	−3.717+0.083i	−0.548+3.542i	−1.421+4.844i
LST (β = 0)	0.011 (+231%)	0.003 (−8%)	0.008 (+140%)
LST (β = 1.18)	0.014 (+22%)	0.010 (−6%)	0.014 (+22%)

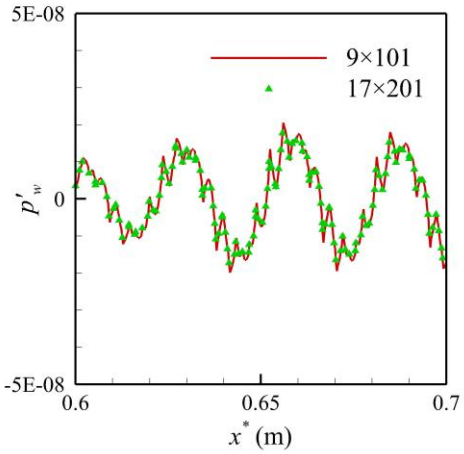

Figure 3-13 Instantaneous wall pressure perturbations under different grid resolutions when β = 1.18.

The baseflow profiles at $x^* = 0.7$ m in porous coating cases, obtained by averaging the flow field within porous coating periods, are summarized in Figure 3-14. Average profiles align closely with the baseline, exhibiting a small impact of porous coatings.

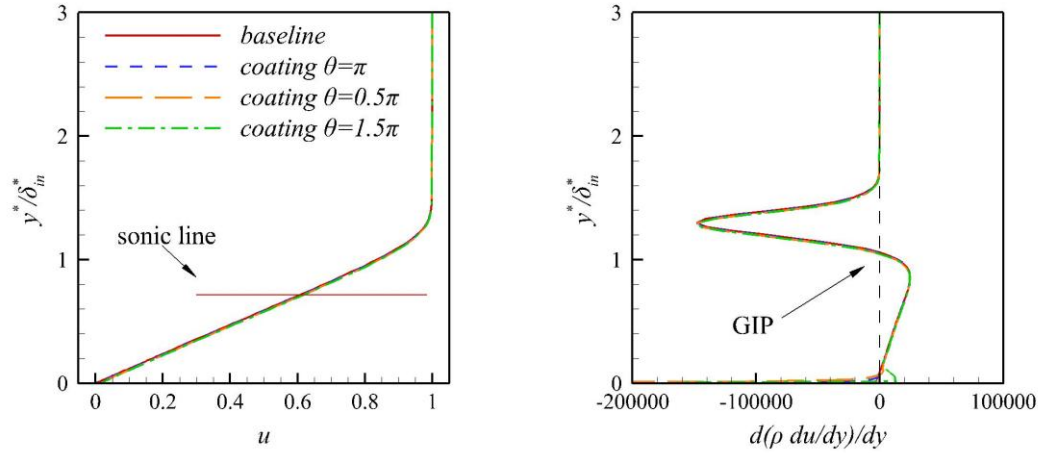

(a) u profiles and sonic line position (b) GIP

Figure 3-14 Averaged baseflow profiles at $x^* = 0.7$ m for porous coating cases.

The evolution of first modes under the influence of porous coatings is illustrated by the maximum u-velocity perturbations at each streamwise station, as depicted in Figure 3-15. The beginning of porous coatings is marked by the vertical dark dashed lines. The LST predictions of growth rate (slopes) at $x^* = 0.7$ m are also depicted with the colored dashed lines for comparison. Porous coatings exhibit distinct impacts on first modes in 2D ($\beta = 0$) and 3D ($\beta = 1.18$) cases.

For planar first modes, growth rate changes roughly resemble the LST prediction within the porous wall region except for the solid–porous junction ($x^* = 0.62 \sim 0.8$ m): the slopes in cases $\theta = 1\pi$ and $\theta = 1.5\pi$ strongly surpass the baseline, while that in case $\theta = 0.5\pi$ closely matches the baseline (Figure 3-15(a)). However, scattering effects emerge at the solid–porous junction, inducing a sudden discontinuity in u'_{max}. The scattering effect introduced by Song and Zhao[112] describes the impact of abrupt boundary condition changes at the solid–porous junction on instability modes. Their study showed that the solid–porous junction strongly suppresses the majority of the second modes but slightly enhances first modes when the admittance phase is 0.75π. In this study, scattering effects under different admittance phases are observed: Case $\theta = 1\pi$, $\beta = 0$ exhibits a slight amplification effect, case $\theta = 0.5\pi$, $\beta = 0$ shows a strong

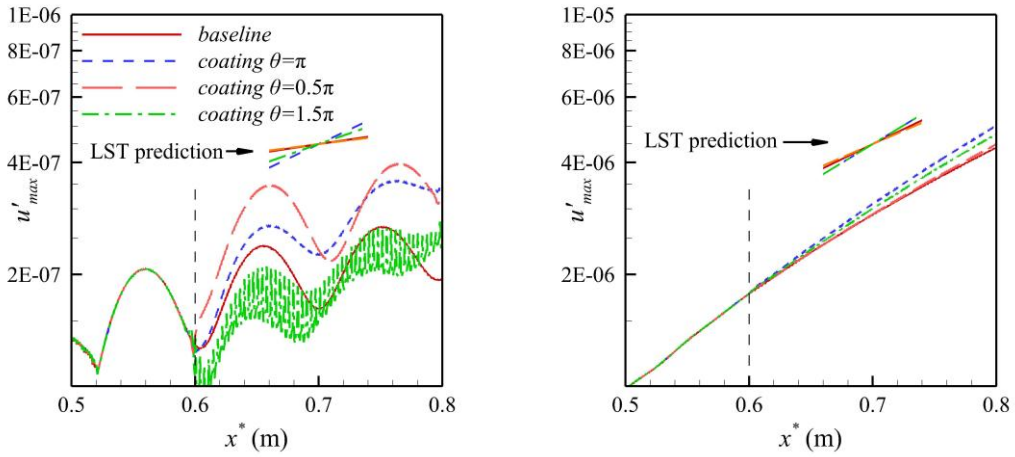

(a) $\beta = 0$ (b) $\beta = 1.18$

Figure 3-15 Evolution of maximum velocity perturbations with different porous coatings.

amplification effect, and case $\theta = 1.5\pi$, $\beta = 0$ shows a significant stabilization effect. In general, wall admittance is a key parameter for controlling planar first modes. These modes undergo scattering effects at solid-to-porous junctions, subsequently exhibiting growth rates aligned with LST predictions.

For 3D cases, growth rate changes deviate from LST predictions, and no scattering effects are observed. As illustrated in Figure 3-15(b), case $\theta = 0.5\pi$ has a marginal stabilization effect from LST, while the DNS result reveals a slight amplifying effect. Furthermore, LST suggests identical growth rates for cases $\theta = \pi$ and $\theta = 1.5\pi$, whereas the amplitude of case $\theta = \pi$ slightly surpasses case $\theta = 1.5\pi$ from DNS. All 3D coating cases exhibit mild destabilization effects. LST captures the impact of porous-wall admittance but neglects the mean flow distortions. However, the highly oblique first Mack mode is of a vortical nature. This physical nature of oblique first modes may lead to a weaker sensitivity to wall acoustic admittance, necessitating DNS with cavity geometries.

Figure 3-16 illustrates growth rates from LST and baseflow pressure contours. Here, the LST is applied on cavity-distorted baseflows and neglects wall admittance effects ($A = 0$). The growth rate for the solid wall case is also included as a reference. For cases $\theta = \pi$ and $\theta = 0.5\pi$, the growth rate will always be beyond or equal to the value in the solid wall case. However, the growth rate for $\theta = 1.5\pi$ case, which holds the largest cavity, can fall below the values in the solid wall case. These trends further

confirm that destabilization effects of oblique first modes are governed by mean flow modifications, rather than acoustic admittance, despite some errors introduced because cavities violate the parallel flow assumption. This result demonstrates that LST analysis of cavity-distorted baseflows provides more reliable predictions than admittance models for oblique first-mode scenarios.

The perturbation streamlines for case $\theta = 1.5\pi$ are illustrated in Figure 3-17, with pressure contours superposed for reference. For the 2D first mode, the near-wall acoustic waves S1 are nearly eliminated by the coating, and V1 persists. For the 3D case, V1 is nearly unchanged, while V2 is distorted. All changes in motion patterns show no connection with the background pressure field, aligning with its small impact on the baseflow.

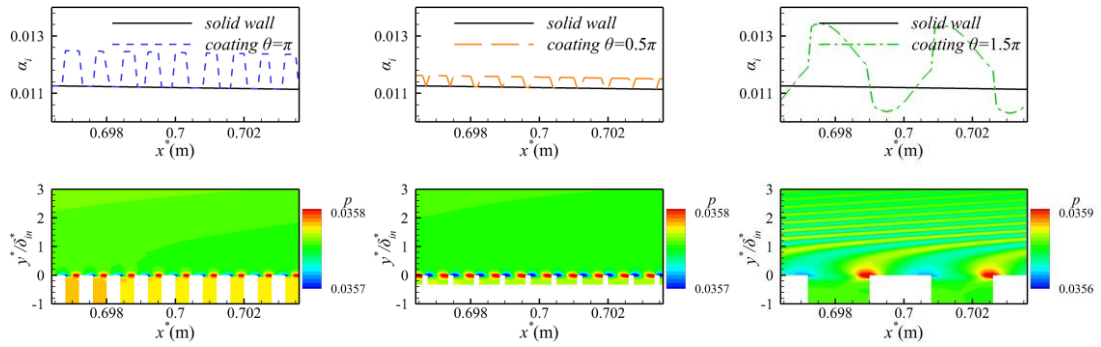

(a) case $\theta = \pi$ (b) case $\theta = 0.5\pi$ (c) case $\theta = 1.5\pi$

Figure 3-16 Growth rates from LST and baseflow pressure contours of porous-coating cases.

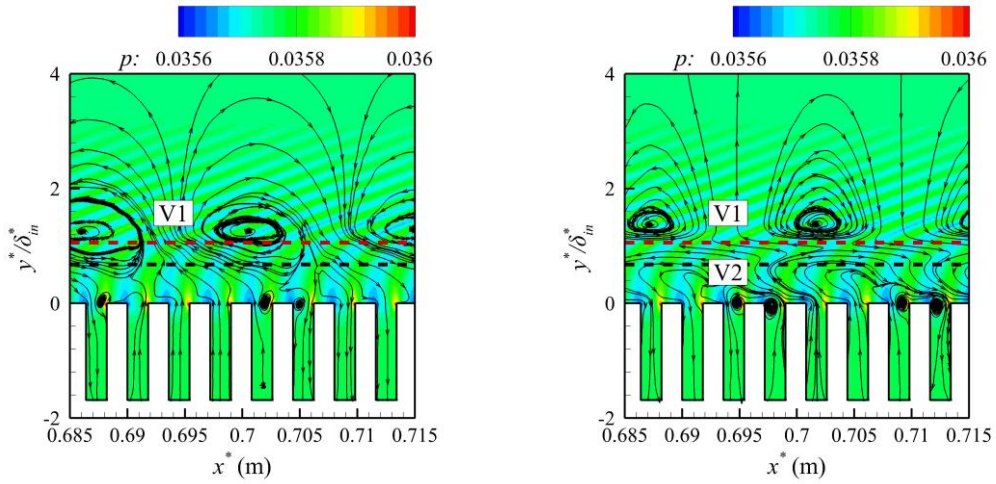

(a) $\beta = 0$ (b) $\beta = 1.18$

Figure 3-17 Perturbation streamlines in coating case $\theta = 1.5\pi$.

These findings reinforce the understanding of first-mode properties: As the planar first mode is an acoustic mode, applying porous coatings strongly affects its evolution, with growth rate trends aligning with LST predictions. Scattering effects can significantly modulate the evolution of first modes and should be considered in engineering applications. By contrast, highly oblique first modes, dominated by vortical dynamics, are destabilized by mean flow distortion rather than acoustic modulations. Previous research[89] attributed the destabilization effect of porous coatings on first Mack modes to an ambiguous "roughness effect". The present results further clarify this phenomenon into two distinct mechanisms: wall admittance effects (predominantly governing 2D first modes) and mean-flow distortion dynamics (for 3D first modes), providing physics-based interpretations for porous coating effects. Given that the most unstable first mode (β = 1.0, Figure 3-3(a)) occurs at a large β, porous coatings are likely an ineffective laminar control technique in first-mode-dominant scenarios. Nevertheless, porous coatings are effective in controlling the Mack 2nd mode instability at high Mach number (Ma > 6.0) and only mildly amplify the most unstable first mode at lower Mach number.

3.3.4. Grooves

The parallel grooves are then designed to estimate their impact on the first mode and are positioned between x^* = 0.6 m and x^* = 0.8 m. The structure scales of grooves are much larger than porous coatings, thus the reference length for the groove structures is set to L_{groove} = 0.004 m, which is close to the boundary layer thickness at x^* = 0.7 m. The groove period s_c is set to $2L_{groove}$. The cavity height H and half-width b (defined in Figure 3-1(c)) are varied to estimate the stabilizing or destabilizing effects.

This investigation first examines the impact of cavity widths with a fixed cavity height $H = 1L_{groove}$, whereas the half-width varies as follows: $0.125L_{groove}$ (*H1b0.125*), $0.25L_{groove}$ (*H1b0.25*), $0.5L_{groove}$ (*H1b0.5*), $0.75L_{groove}$ (*H1b0.75*), and $0.875L_{groove}$ (*H1b0.875*). The grid dimensions for the narrowest groove are specified as 6 × 101 for each cavity, whereas the widest groove has grid dimensions of 36 × 101. The grid convergence is validated using case *H1b0.5*, with the grid resolutions of 21×101 (coarse grid) and 31×151 (fine grid) for each cavity. Figure 3-18 compares the evolution of 2D first-mode amplitudes. The strong agreement between coarse and fine grids confirms grid independence. The coarse grid is used for subsequent calculations. Figure 3-19 presents the evolution of $u'_{\max}$. All grooves destabilize first modes within grooved regions.

For 2D first modes, abrupt $u'_{\max}$ jumps occur at each cavity leading edge due to

expansion waves, followed by recoveries. These zigzag oscillations associated with the compression or expansion waves induced by macro-slit grooves have also been observed for second Mack modes[113]. Macro-slit grooves amplify 2D first modes, with amplification effects being positively correlated with cavity widths. The maximum amplification occurs in case *H1b0.875* (3×10^{-7} to 1.1×10^{-6} at $x^* = 0.85$ m). Table 3-2 compares DNS-derived wall admittance (via equation (2.15)) with theoretical model predictions (equation (2.16)). Significant divergences between admittance values of the DNS and the theoretical model indicate that the admittance model becomes invalid for macro-slit cavities. Table 3-2 also presents LST-predicted growth rates, along with the stabilizing or destabilizing effects relative to the no-coating case. LST calculations use DNS-derived admittance values and the undisturbed baseflow profile at $x^* = 0.7$ m. Conventional methods typically use the undisturbed baseflow profile and theoretical admittance values to assess the effects of porous coatings[88], whereas this study uses admittance values from DNS as the theoretical model is invalid. The growth rates increase with larger cavity widths, closely aligning with $u'_{\max}$ amplitude trends shown in Figure 3-19(a). This alignment identifies wall admittance as a mechanism for the impact of macro-cavity grooves.

In contrast, oblique first modes experience marginal amplification. Saturation occurs for $b \geq 0.75L_{groove}$, where widening cavities no longer enhance destabilization effects. This amplification behavior is similar to the effects of porous coatings, which manifest a mechanism related to mean-flow distortions.

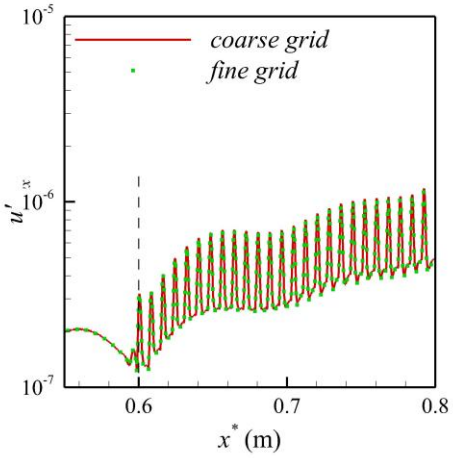

Figure 3-18 The maximum *u'* in case *H1b0.5* under different grid resolutions.

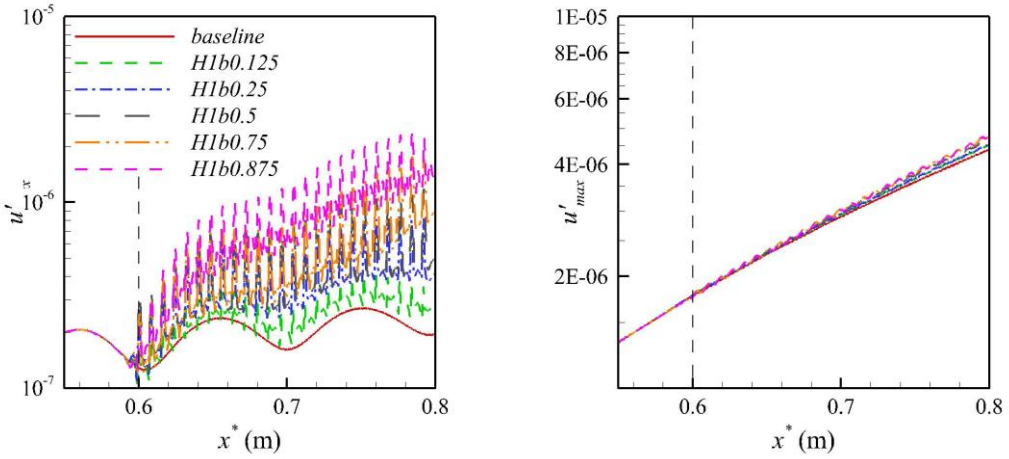

(a) $\beta = 0$ (b) $\beta = 1.18$

Figure 3-19 The maximum u' in grooved cases with different widths.

Table 3-2 Wall admittances and growth rates of grooves with different cavity widths.

	H1b0.125	*H1b0.25*	*H1b0.5*	*H1b0.75*	*H1b0.875*
Model $\|A\|$	2.10	4.72	12.27	34.03	62.86
Model θ/π	1.35	1.43	1.46	1.45	1.43
DNS $\|A\|$	4.14	9.67	10.54	12.21	15.77
DNS θ/π	1.11	1.34	1.32	1.03	0.88
α_i	0.0142 (26.79%)	0.0160 (42.86%)	0.0165 (47.32%)	0.0189 (68.75%)	0.0216 (92.86%)

The influence of cavity height is analyzed with a fixed cavity width $b = 0.5L_{groove}$, with heights varying as follows: $0.1L_{groove}$ (*H0.1b0.5*), $0.5L_{groove}$ (*H0.5b0.5*), $1L_{groove}$ (*H1b0.5*), $1.25L_{groove}$ (*H1.25b0.5*), $1.5L_{groove}$ (*H1.5b0.5*), and $2L_{groove}$ (*H2b0.5*). The shallowest groove has grid dimensions of 21 × 23 for each cavity, whereas the deepest groove has grid dimensions of 21 × 201. The evolutions of $u'_{\max}$ are illustrated in Figure 3-20.

For 2D first modes, destabilization exhibits a nonmonotonic response, with the maximum amplification effects observed in cases *H0.5b0.5* and *H1b0.5*. Wall admittance values calculated from DNS data and the admittance model are shown in Table 3-3, along with the LST-predicted growth rates. The admittance model predictions remain inconsistent with DNS results, and the DNS-derived admittance

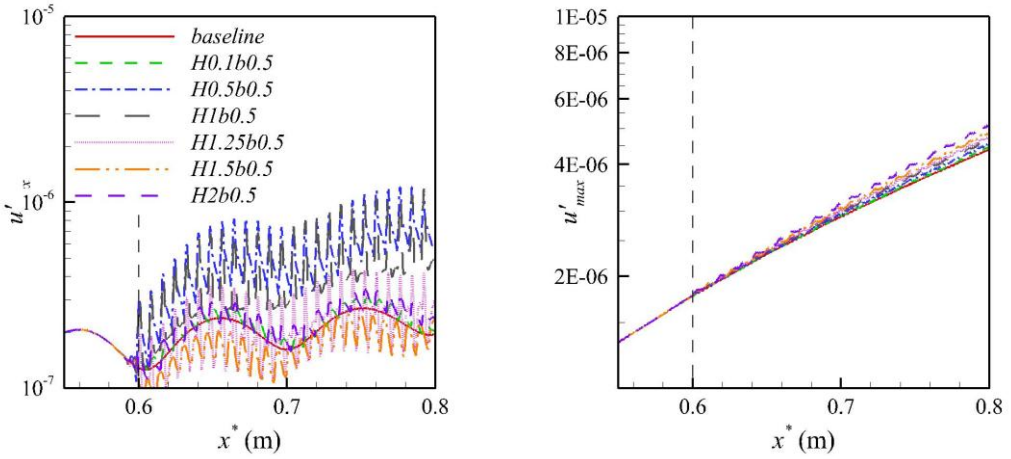

(a) $\beta = 0$ (b) $\beta = 1.18$

Figure 3-20 The maximum u' in grooved cases with different heights.

Table 3-3 Wall admittances and growth rates of grooves with different cavity heights.

	H0.1b0.5	*H0.5b0.5*	*H1b0.5*	*H1.25b0.5*	*H1.5b0.5*	*H2b0.5*
Model $\|A\|$	0.79	6.90	12.27	5.34	2.74	1.10
Model θ/π	0.51	0.52	1.46	1.47	1.46	0.64
DNS $\|A\|$	0.97	13.92	10.54	6.74	4.20	3.46
DNS θ/π	0.53	0.72	1.32	1.45	1.48	1.24
α_i	0.0108 (−3.57%)	0.0196 (75.00%)	0.0165 (47.32%)	0.0141 (25.89%)	0.0130 (16.07%)	0.0136 (21.43%)

phase varies from 0.53π to 1.48π, resulting in distinct admittance-related behaviors: For grooves with phases near 1.5π (cases *H1.25b0.5* and *H1.5b0.5*), the scattering effect at the solid-groove joint causes a sudden decrease of $u'_{\max}$ amplitudes ($x^* = 0.6 \sim 0.62$ m), followed by an accelerated growth of the instabilities due to the wall admittance. At the end of grooves ($x^* = 0.78 \sim 0.8$ m), a reverse scattering effect is induced by the groove-solid joint. The stronger amplification in case *H1.25b0.5* in Figure 3-20(a) correlates with its larger LST-predicted growth rate. For smaller-phases cases (cases *H1b0.5* and *H2b0.5*), the initial stabilizing scattering effect vanishes, and first modes are gradually destabilized following LST predictions. The initial destabilizing scattering effect in case *H0.5b0.5* is covered up by the strong destabilization effect (75.00%), while a stabilizing scattering effect is exhibited at the porous-solid joint. Case H0.1b0.5 shows minimal

impact due to its small admittance magnitude $|A|$. These observations suggest that wall acoustic conditions are the dominant mechanism for grooves, despite their significantly larger geometric scale compared to porous coatings.

For 3D first modes, the grooves only destabilize the first mode. The destabilization effect increases monotonically with cavity depth. These distinct responses reflect the differing physical properties of 2D and 3D first modes.

Cases *H1b0.5* and *H1.5b0.5* are analyzed to further validate the mean-flow distortion mechanism of grooves on 3D first modes. The pressure contours are depicted in Figure 3-21, revealing nearly identical pressure fields despite different cavity heights. Both cases exhibit expansion waves at the leading edge and compression waves at the trailing edge of each cavity. Figure 3-22 depicts the LST growth rates in cases *H1b0.5* and *H1.5b0.5*, along with the baseline for comparison. It should be noted that LST calculations use distorted baseflow profiles (including cavity flows) around $x^* = 0.7$ m while omitting the wall admittance boundary condition, thereby directly accounting for mean-flow distortion effects. Growth rates are higher in case *H1.5b0.5*, indicating the first mode is more significantly amplified by the deeper cavity. The flow profiles at $x^* = 0.7$ m in these two cases, obtained by averaging the flow field within a groove period ($x^* = 0.696 \sim 0.704$ m), are shown in Figure 3-23. Sonic lines and GIPs of grooved cases are not marked due to their small deviations from the baseline positions. Average profiles align closely with the baseline, exhibiting only small displacements toward the wall. These results indicate that distinct LST strategies should be used to evaluate the impacts of grooves on 2D and 3D first modes.

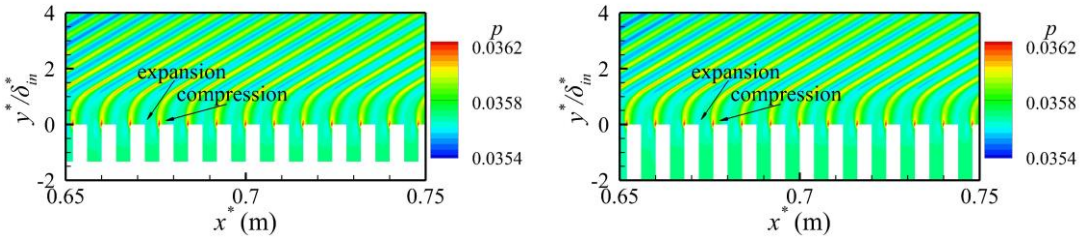

(a) *H1b0.5* (b) *H1.5b0.5*

Figure 3-21 The baseflow pressure contours in grooved cases.

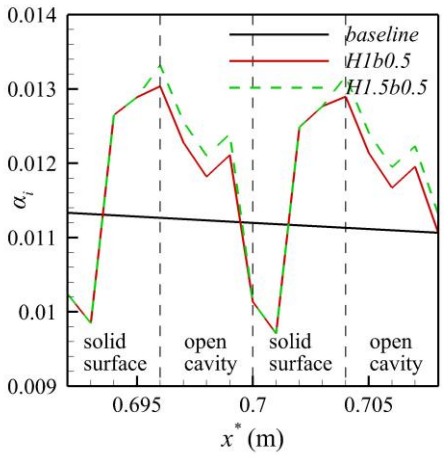

Figure 3-22 Comparison of LST growth rates between cases *H1b0.5* and *H1.5b0.5*.

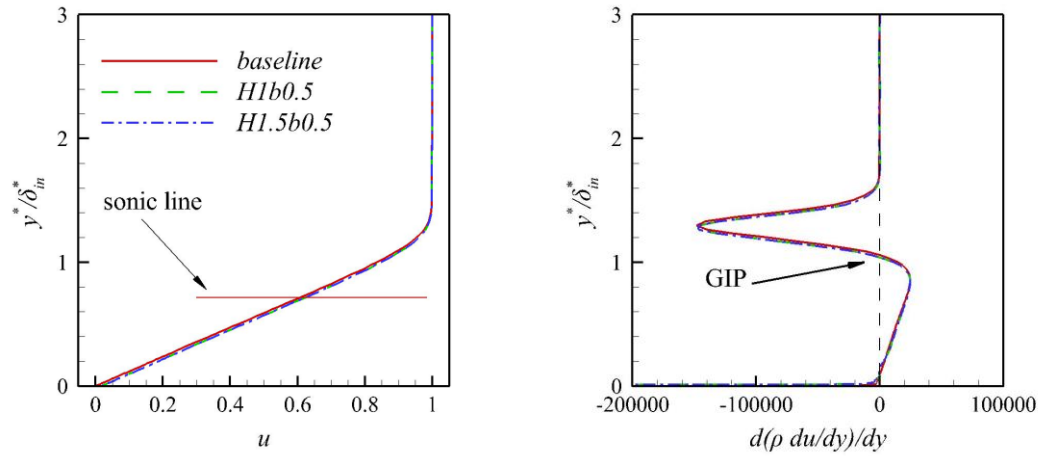

(a) *u* profiles and sonic line positions (b) GIPs

Figure 3-23 Baseflow profiles at $x^* = 0.7$ m for grooved cases.

Perturbation streamlines for grooved cases are illustrated in Figure 3-24, with pressure contours superposed for reference. Macro-slit grooves impose pronounced modulations on perturbation streamline topology, especially for the 2D first mode: In case *H1b0.5*, perturbation patterns (V1 and S1) are entirely disrupted and unidentifiable, whereas case *H1.5b0.5* partially preserves these patterns except for upper-region distortions ($y^*/\delta^*_{in} > 2$), where perturbation streamlines align with compression and expansion waves. 3D modes demonstrate less sensitivity compared to 2D cases: V1 and V2 remain identifiable despite geometric warping, indicating greater resistance of vortical modes to groove-induced perturbations.

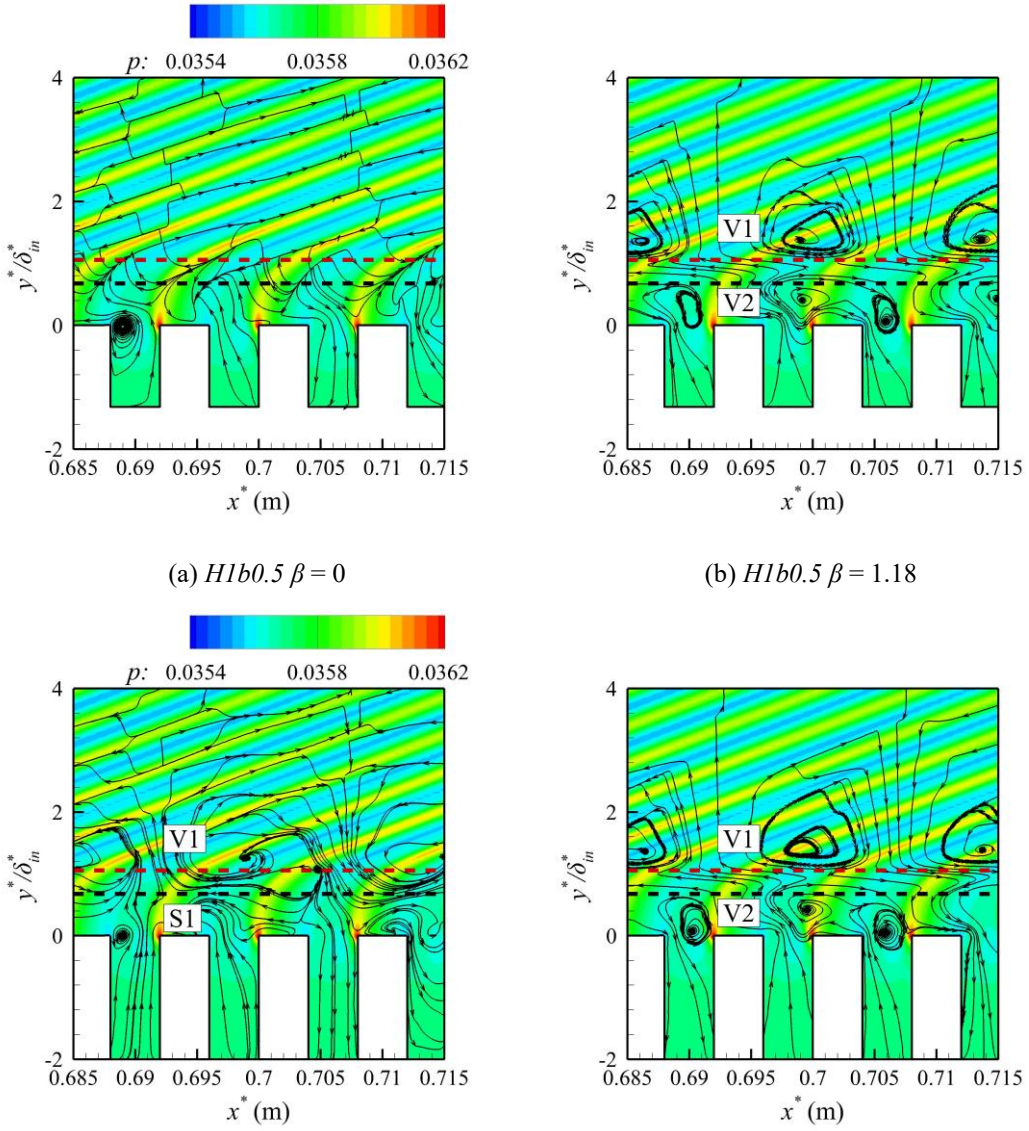

(a) *H1b0.5* $\beta = 0$ (b) *H1b0.5* $\beta = 1.18$

(c) *H1.5b0.5* $\beta = 0$ (d) *H1.5b0.5* $\beta = 1.18$

Figure 3-24 Perturbation streamlines in grooved cases.

3.4. MPT Analysis of Stabilization Mechanisms

3.4.1. Wall cooling-heating

The momentum density fields obtained from DNS are decomposed using MPT. The magnitudes of MPT components at $x^* = 0.7$ m in $T_w = 2$ cases are depicted in Figure 3-25 and Figure 3-26, with baseline profiles provided for comparison. The dash-dotted lines represent the primary GIP position, the dashed lines mark the sonic line, and the second GIP is not plotted because it is relatively close to the sonic line.

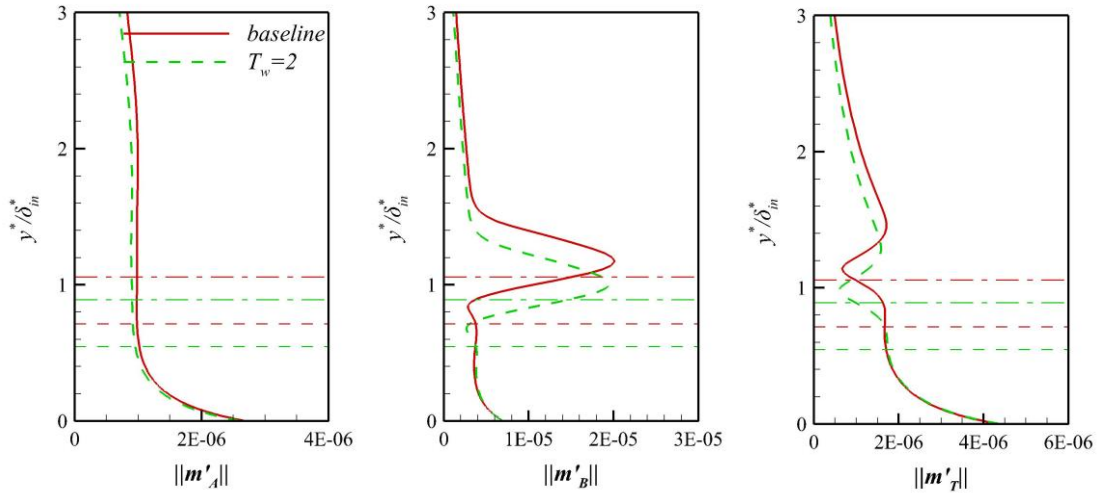

(a) acoustic component (b) vortical component (c) thermal component

Figure 3-25 The MPT component magnitudes at x^* = 0.7 m in 2D T_w = 2 case. Unit: kg/(m^{2}s).

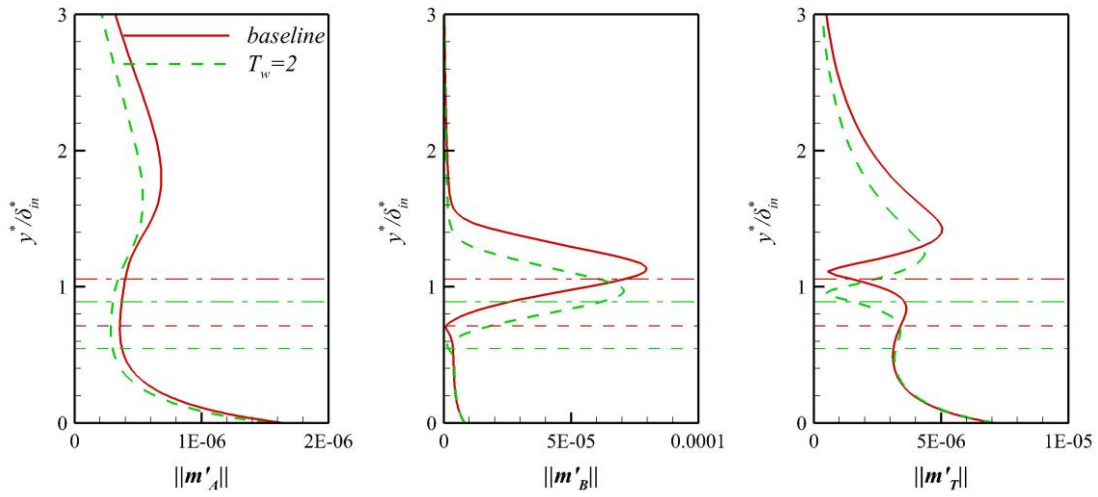

(a) acoustic component (b) vortical component (c) thermal component

Figure 3-26 The MPT component magnitudes at x^* = 0.7 m in 3D T_w = 2 case. Unit: kg/(m^{2}s).

Besides the magnitudes, the spatial wavelength is also a key characteristic of any instability[103]. The variations in the wavelengths of MPT components reflect their sensitivity to stabilization techniques[108]. In the present study, the averaged streamwise wavelengths for first modes and MPT components are calculated by examining the periodicity in u', $\boldsymbol{m}'_A$, $\boldsymbol{m}'_B$, and $\boldsymbol{m}'_T$ at the sonic line (for 2D cases) and GIP (for 3D

cases) within the controlled regions, considering u' peaks are located nearly at the sonic line at β = 0 and at the GIP at β = 1.18 from Figure 3-3. The streamwise wavelengths λ_x^* of the perturbation (evaluated and represented by u') and the corresponding MPT components for wall-cooling cases are summarized in Table 3-4.

Table 3-4 Comparison of λ_x^* between the baseline case and the wall-cooling case.

		u'	$\boldsymbol{m}'_A$	$\boldsymbol{m}'_B$	$\boldsymbol{m}'_T$
2D	baseline	0.0289	0.0289	0.0289	0.0287
	cooling	0.0289	0.0289	0.0289	0.0291
	proportion	0.00%	0.00%	0.00%	1.30%
3D	baseline	0.0282	0.0291	0.0284	0.0273
	cooling	0.0289	0.0291	0.0286	0.0291
	proportion	2.65%	0.00%	0.66%	6.85%

For the 2D first mode, MPT components exhibit minor modifications under wall cooling, as illustrated in Figure 3-25, $\boldsymbol{m}'_A$ decreases slightly above the sonic line, while $\boldsymbol{m}'_B$ and $\boldsymbol{m}'_T$ shift marginally toward the wall. For the wavelengths, only undergoes amplification, indicating a thermal-dominated mechanism.

The 3D first mode exhibits distinct behaviors. All MPT component magnitudes undergo significant reductions alongside their shift toward the wall. Streamwise wavelength analysis reveals a larger wavelength of the first-mode instability, with $\boldsymbol{m}'_T$ showing an increased wavelength, indicating that the thermal component is directly influenced.

3.4.2. Wall blowing-suction

The MPT decomposition is subsequently applied to wall-suction cases. With the same pattern, Figure 3-27 and Figure 3-28 depict MPT component magnitudes at x^* = 0.7 m for 2D and 3D wall-suction cases. Table 3-5 summarizes the streamwise wavelengths.

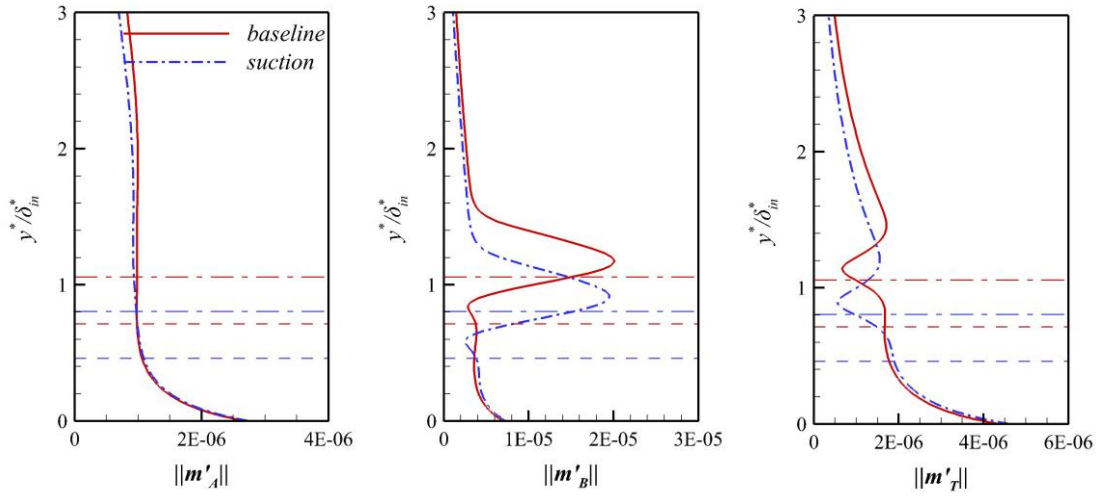

(a) acoustic component (b) vortical component (c) thermal component

Figure 3-27 The MPT component magnitudes at x^* = 0.7 m for 2D wall-suction case. Unit: kg/(m^{2}s).

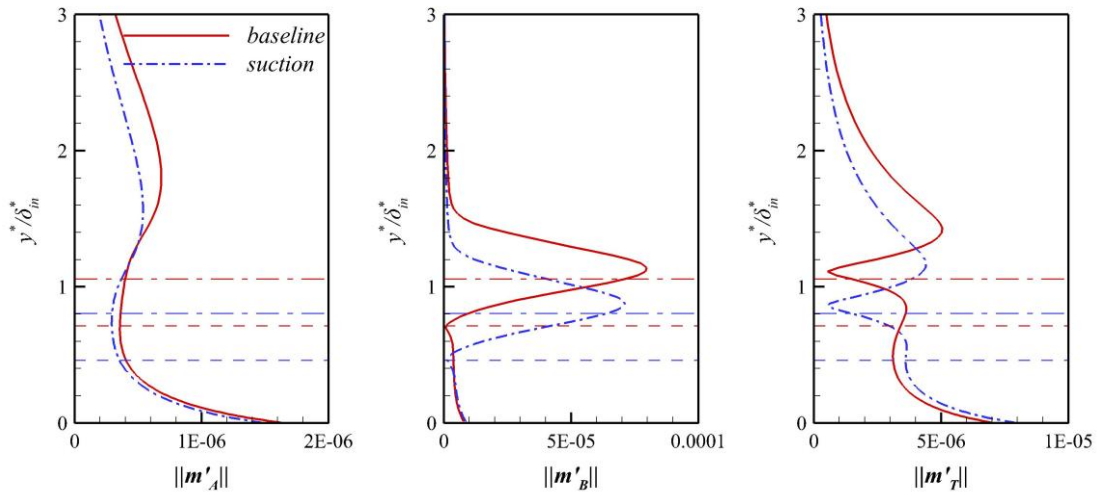

(a) acoustic component (b) vortical component (c) thermal component

Figure 3-28 The MPT component magnitudes at x^* = 0.7 m for 3D wall-suction case. Unit: kg/(m^{2}s).

Table 3-5 Comparison of λ_x^* between the baseline case and the wall-suction case.

		u'	m'_A	m'_B	m'_T
2D	baseline	0.0289	0.0289	0.0289	0.0287
	suction	0.0289	0.0289	0.0289	0.0289

	proportion	0.00%	0.00%	0.00%	0.65%
3D	baseline	0.0282	0.0291	0.0284	0.0273
	suction	0.0301	0.0291	0.0299	0.0302
	proportion	6.62%	0.00%	5.26%	10.96%

For the 2D first mode, $\boldsymbol{m}'_A$ decreases slightly above the GIP but increases marginally below it. $\boldsymbol{m}'_T$ follows a similar trend, with its peak magnitude diminishing above the GIP and amplifying beneath it. $\boldsymbol{m}'_B$ and $\boldsymbol{m}'_T$ shift significantly toward the wall. For the wavelengths, the first-mode streamwise wavelength remains unchanged. Only $\boldsymbol{m}'_B$ exhibits a distinguishable increment in wavelength, indicating that the thermal component is active in 2D first modes.

For the 3D first mode, $\boldsymbol{m}'_A$ reduces throughout the boundary layer, $\boldsymbol{m}'_B$ exhibits a significant reduction at its peak, while $\boldsymbol{m}'_T$ shows a similar change to 2D case. Streamwise wavelength analysis reveals a larger wavelength of the first-mode instability, with $\boldsymbol{m}'_T$ displaying the most pronounced wavelength increase and $\boldsymbol{m}'_B$ experiencing a secondary increase. The analogous $\boldsymbol{m}'_T$ response in 2D and 3D configurations may be attributed to inherent thermal component susceptibility to wall-normal flow modifications.

3.4.3. Porous coatings

As previously discussed, the case $\theta = 0.5\pi$ leads to a marginally lower growth rate than the baseline, but the stabilization effect is eradicated by the scattering effect. Conversely, the case $\theta = 1.5\pi$ initially exhibits a stabilizing scattering effect before a significantly higher growth rate. These two cases are selected for further analysis. The average magnitudes of MPT components for porous coating cases are depicted in Figure 3-29 and Figure 3-30. Sonic lines and GIPs in porous coating cases are omitted due to their small deviations from the baseline positions. Table 3-6 and Table 3-7 exhibit the wavelengths in cases $\theta = 0.5\pi$ and $\theta = 1.5\pi$.

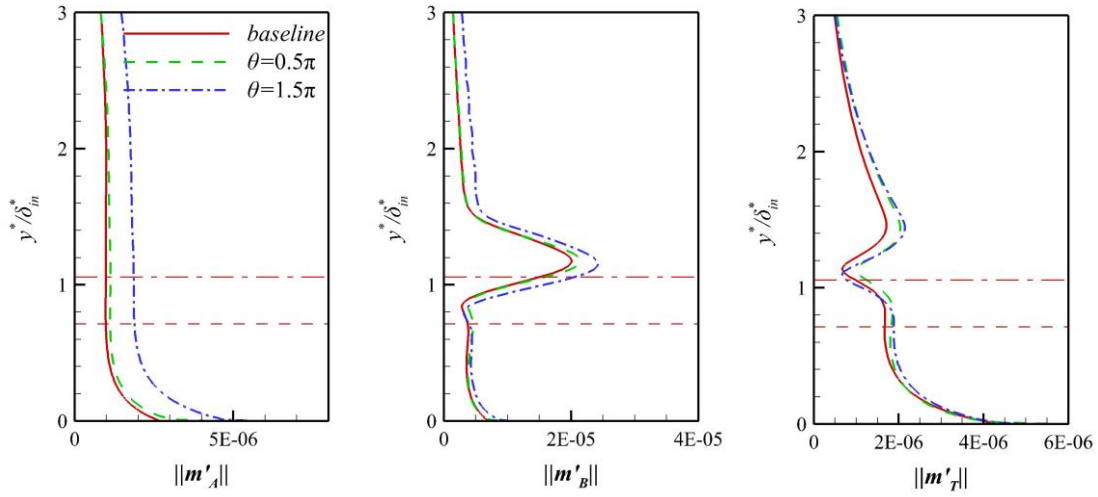

(a) acoustic component (b) vortical component (c) thermal component

Figure 3-29 The average MPT component magnitudes at x^* = 0.7 m for 2D porous coating cases. Unit: kg/(m^{2}s).

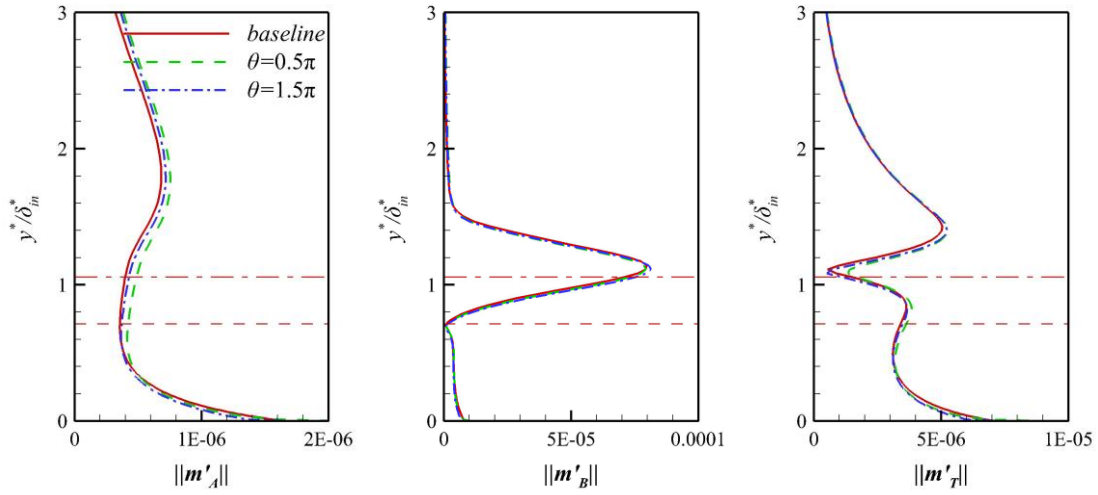

(a) acoustic component (b) vortical component (c) thermal component

Figure 3-30 The average MPT component magnitudes at x^* = 0.7 m for 3D porous coating cases. Unit: kg/(m^{2}s).

Table 3-6 Comparison of λ_x^* between the baseline case and case $\theta = 0.5\pi$.

		u'	$\boldsymbol{m}'_A$	$\boldsymbol{m}'_B$	$\boldsymbol{m}'_T$
2D	baseline	0.0289	0.0289	0.0289	0.0287
	$\theta = 0.5\pi$	0.0291	0.0294	0.0293	0.0293

	proportion	0.71%	1.46%	1.12%	1.78%
3D	baseline	0.0282	0.0291	0.0284	0.0273
	$\theta = 0.5\pi$	0.0283	0.0291	0.0284	0.0292
	proportion	0.55%	−0.17%	0.02%	6.96%

Table 3-7 Comparison of λ_x^* between the baseline case and case $\theta = 1.5\pi$.

		u'	$\boldsymbol{m}'_A$	$\boldsymbol{m}'_B$	$\boldsymbol{m}'_T$
2D	baseline	0.0289	0.0289	0.0289	0.0287
	$\theta = 1.5\pi$	0.0288	0.0285	0.0287	0.0287
	proportion	−0.45%	−1.53%	−0.77%	−0.27%
3D	baseline	0.0282	0.0291	0.0284	0.0273
	$\theta = 1.5\pi$	0.0284	0.0290	0.0285	0.0269
	proportion	0.79%	−0.36%	0.60%	−1.37%

In the 2D $\theta = 0.5\pi$ case, $\boldsymbol{m}'_A$ and $\boldsymbol{m}'_B$ exhibit marginal amplification, while $\boldsymbol{m}'_T$ is obviously amplified. In contrast, for the 2D $\theta = 1.5\pi$ case, $\boldsymbol{m}'_A$ is nearly doubled, $\boldsymbol{m}'_B$ slightly exceeds the baseline value, and $\boldsymbol{m}'_T$ similarly demonstrates marked amplification. This divergence aligns with their distinct admittance characteristics: At $\theta = 0.5\pi$, LST indicates damping effects on 2D first modes, which corresponds to the low amplitude of the acoustic component. At $\theta = 1.5\pi$, the first mode exhibits large growth rates and experiences direct amplification through the acoustic component. The wavelength data in Table 3-6 and Table 3-7 corroborate these observations: For the 2D $\theta = 0.5\pi$ case, $\boldsymbol{m}'_A$ and $\boldsymbol{m}'_T$ show significant modifications, and $\boldsymbol{m}'_A$ is the most strongly affected component in the 2D $\theta = 1.5\pi$ case.

For 3D cases, the near-wall $\boldsymbol{m}'_A$ (below the sonic line) and $\boldsymbol{m}'_T$ (below the GIP) experience mild damping, while off-wall MPT components are marginally amplified. These responses originate from two mechanisms: the absence of a solid wall, leading to near-wall damping, and the appearance of compression/expansion waves, causing off-wall amplification. These baseflow distortions can be credited to the amplifying effect on 3D first modes. Case *H1.5b0.5* has slightly stronger compression and expansion waves than case *H1b0.5*, resulting in a stronger off-wall amplification, whereas their near-wall amplitudes are nearly the same.

Instantaneous snapshots of MPT components are presented in Figure 3-31 and

Figure 3-32. The MPT behaviors further clarify the baseflow distortion mechanisms for 3D first modes: near-wall components exhibit damping at each cavity opening, while off-wall components undergo amplification due to compression and expansion waves. These phenomena demonstrate greater prominence under large half-width ($\theta = 1.5\pi$).

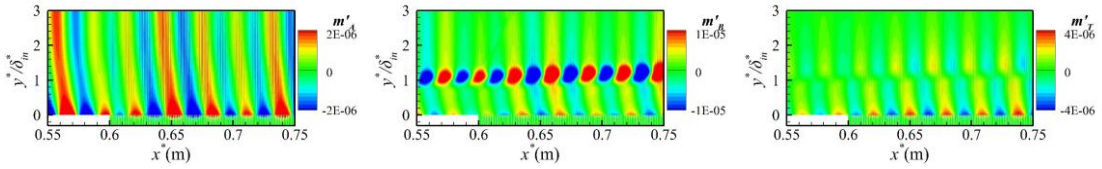

(a) $\beta = 0$ acoustic component (b) $\beta = 0$ vortical component (c) $\beta = 0$ thermal component

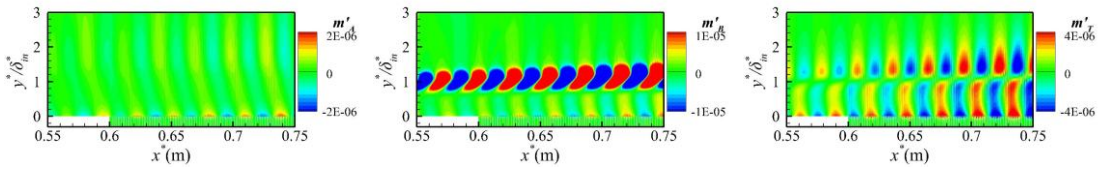

(d) $\beta = 1.18$ acoustic component (e) $\beta = 1.18$ vortical component (f) $\beta = 1.18$ thermal component

Figure 3-31 Instantaneous magnitude of MPT components for case $\theta = 0.5\pi$. Unit: kg/(m^{2}s).

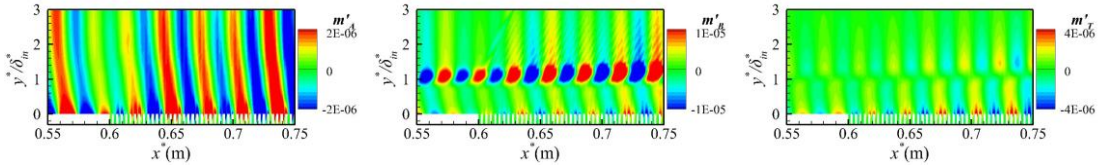

(a) $\beta = 0$ acoustic component (b) $\beta = 0$ vortical component (c) $\beta = 0$ thermal component

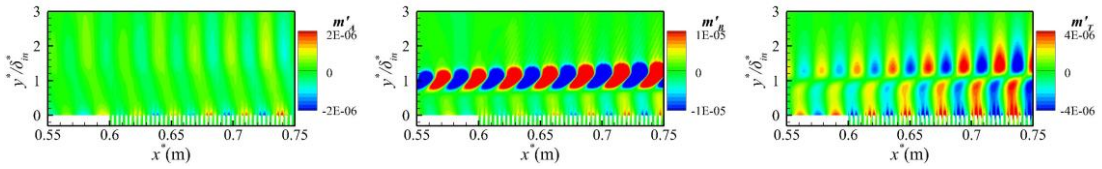

(d) $\beta = 1.18$ acoustic component (e) $\beta = 1.18$ vortical component (f) $\beta = 1.18$ thermal component

Figure 3-32 Instantaneous magnitude of MPT components for case $\theta = 1.5\pi$. Unit: kg/(m^{2}s).

3.4.4. Grooves

The MPT component magnitudes in grooved cases *H1b0.5* and *H1.5b0.5* are depicted in Figure 3-33 and Figure 3-34, where the magnitudes are obtained by

averaging the MPT components within a groove period (x^* = 0.696 ~ 0.704 m), similar to the treatment in Figure 3-23. Sonic lines and GIPs in grooved cases are not depicted due to their small deviations from the baseline positions. Table 3-8 and Table 3-9 exhibit the wavelengths in cases *H1b0.5* and *H1.5b0.5*.

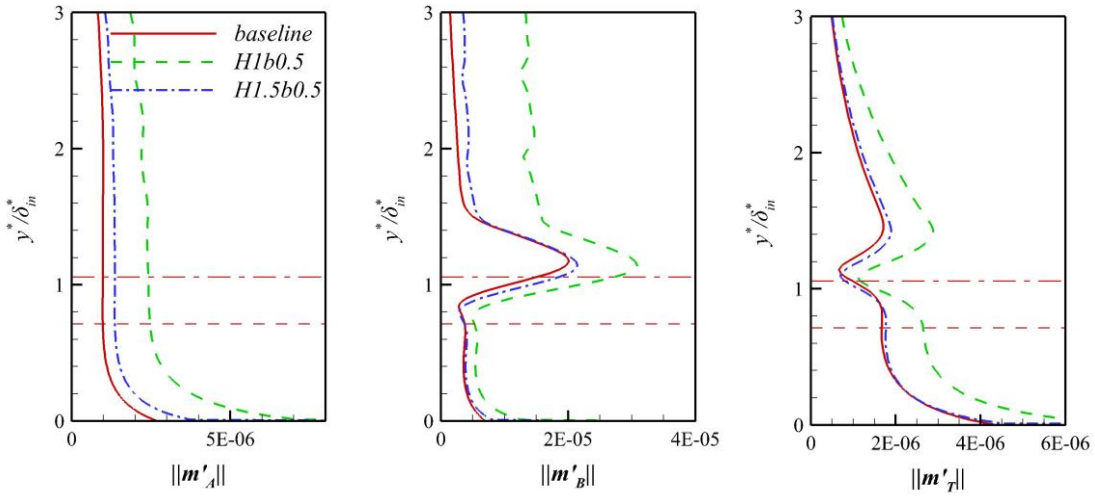

(a) acoustic component (b) vortical component (c) thermal component

Figure 3-33 The average MPT component magnitudes at x^* = 0.7 m for 2D grooved cases. Unit: kg/(m^{2}s).

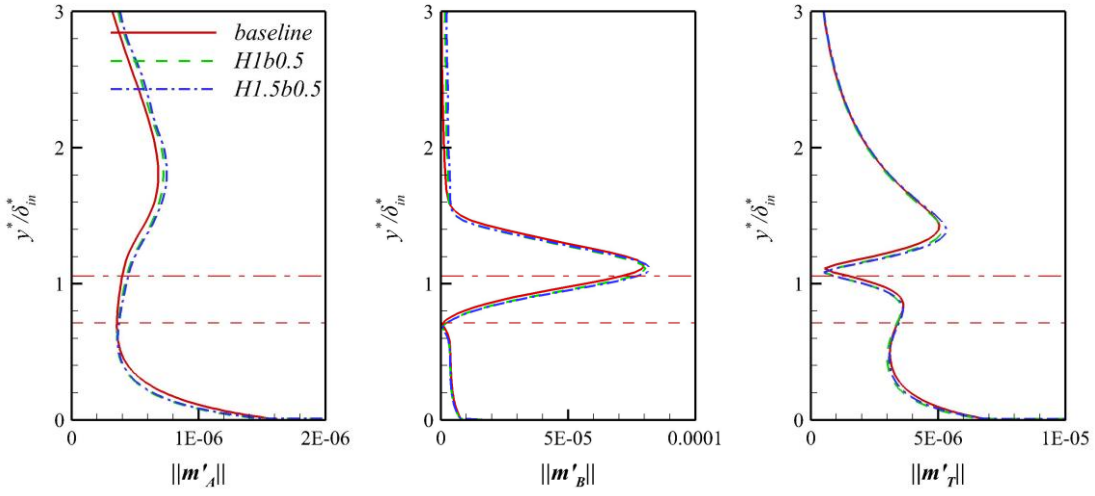

(a) acoustic component (b) vortical component (c) thermal component

Figure 3-34 The average MPT component magnitudes at x^* = 0.7 m for 3D grooved cases. Unit: kg/(m^{2}s).

Table 3-8 Comparison of λ_x^* between the baseline case and case *H1b0.5*.

		u'	$\boldsymbol{m}'_A$	$\boldsymbol{m}'_B$	$\boldsymbol{m}'_T$
2D	baseline	0.0289	0.0289	0.0289	0.0287
	H1b0.5	0.0281	0.0282	0.0294	0.0283
	proportion	−2.88%	−2.43%	1.51%	−1.57%
3D	baseline	0.0282	0.0291	0.0284	0.0273
	H1b0.5	0.0284	0.0284	0.0285	0.0259
	proportion	0.76%	−2.33%	0.50%	−5.05%

Table 3-9 Comparison of λ_x^* between the baseline case and case *H1.5b0.5*.

		u'	$\boldsymbol{m}'_A$	$\boldsymbol{m}'_B$	$\boldsymbol{m}'_T$
2D	baseline	0.0289	0.0289	0.0289	0.0287
	H1.5b0.5	0.0293	0.0282	0.0290	0.0283
	proportion	1.15%	−2.70%	0.06%	−1.46%
3D	baseline	0.0282	0.0291	0.0284	0.0273
	H1.5b0.5	0.0284	0.0283	0.0285	0.0258
	proportion	0.76%	−2.67%	0.61%	−5.36%

For 2D cases, all MPT components exhibit significant amplification in case *H1b0.5*, especially $\boldsymbol{m}'_A$, which nearly doubles in magnitude. In contrast, case *H1.5b0.5* only slightly exceeds the baseline. This divergence correlates with their distinct admittance characteristics: Case *H1b0.5* deviates from 1.5π, making the initial stabilizing scattering effect vanish. The acoustic component is strongly amplified by the wall admittance. Further increasing the cavity height to 1.5 makes the admittance reach 1.5π, resulting in weaker amplification of the acoustic component due to the initial scattering effect and the smaller LST-predicted growth rate. The wavelengths in Table 3-8 and Table 3-9 corroborate the acoustic-dominated mechanism. It is interesting to find that the wall admittance is still a governing mechanism for large-cavity grooves, despite the failure of admittance models for these structures.

For 3D cases, the near-wall $\boldsymbol{m}'_A$ (below the sonic line) and $\boldsymbol{m}'_T$ (below the GIP) experience mild damping, while off-wall MPT components are marginally amplified.

These responses originate from two mechanisms: the absence of a solid wall, leading to near-wall damping, and the appearance of compression/expansion waves, causing off-wall amplification. These baseflow distortions can be credited to the amplifying effect on 3D first modes. Case *H1.5b0.5* has slightly stronger compression and expansion waves than case *H1b0.5*, resulting in a stronger off-wall amplification, whereas their near-wall amplitudes are nearly the same.

Instantaneous snapshots of MPT components are presented in Figure 3-35 and Figure 3-36.

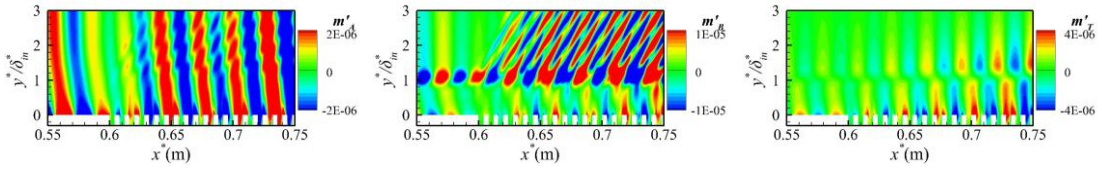

(a) $\beta = 0$ acoustic component (b) $\beta = 0$ vortical component (c) $\beta = 0$ thermal component

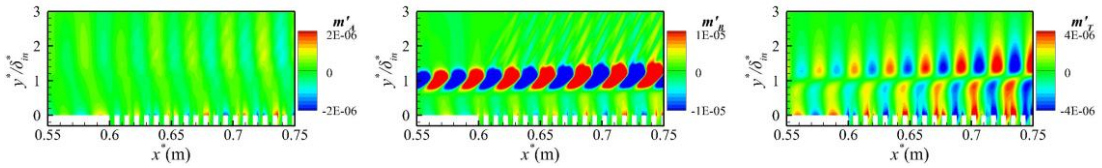

(d) $\beta = 1.18$ acoustic component (e) $\beta = 1.18$ vortical component (f) $\beta = 1.18$ thermal component

Figure 3-35 Instantaneous magnitude of MPT components for case *H1b0.5*. Unit: kg/(m^{2}s).

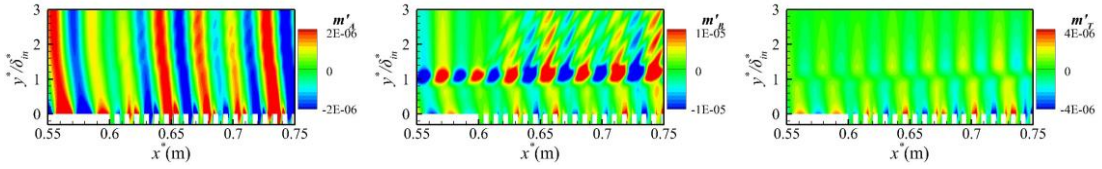

(a) $\beta = 0$ acoustic component (b) $\beta = 0$ vortical component (c) $\beta = 0$ thermal component

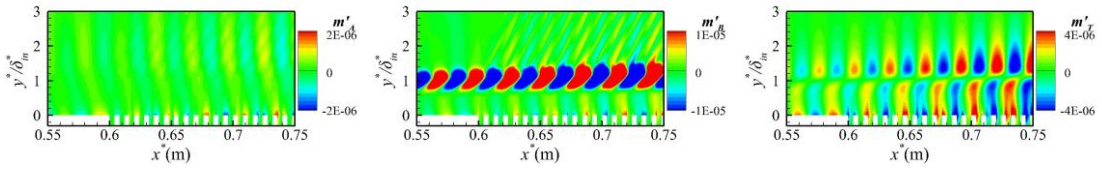

(d) $\beta = 1.18$ acoustic component (e) $\beta = 1.18$ vortical component (f) $\beta = 1.18$ thermal component

Figure 3-36 Instantaneous magnitude of MPT components for case *H1.5b0.5*. Unit: kg/(m^{2}s).

Compared to porous coating cases (Figure 3-31 and Figure 3-32), large-cavity grooves exert more significant impacts on the components: For 2D cases, acoustic and vortical components are modified by the compression and expansion waves. For 3D cases, MPT components exhibit similar changes to the large half-width porous coating case, but the changes are more pronounced.

3.5. Summary

The first Mack modes in a Mach 4.5 flat-plate boundary layer are comprehensively investigated using LST, DNS, and MPT, focusing on their physical properties and responses to stabilization techniques under different spanwise wavenumbers. The significant findings are listed as follows:

As the spanwise wavenumber increases, the streamwise wavenumber initially rises before declining, with its maximum marking the transition of the first mode from an acoustic to a vortical nature. Momentum potential theory is then applied to decompose fluctuating momentum in the perturbation field into vortical, acoustic, and thermal components. The results indicate that as the spanwise wavenumber increases, the proportion of acoustic components diminishes, while vortical components progressively dominate.

These distinct physical characteristics lead to divergent responses to control techniques and stabilization mechanisms: Wall cooling provides a slight stabilization to planar first modes and significantly stabilizes oblique first modes by suppressing the thermal component. Wall suction similarly exhibits a weaker stabilization effect on planar first modes compared to their oblique counterparts, with thermal and vortical components in the oblique mode damped under steady suction. Slightly oblique first modes are modulated by scattering effects and wall admittance, while highly oblique first modes are destabilized by mean flow distortions induced by the coatings. Grooves, despite their macroscale geometry relative to porous coatings, govern planar first modes through wall-admittance mechanisms, where the acoustic component is modulated by wall admittance. For highly oblique first modes, baseflow distortions are also responsible for the destabilization effects of grooves.

Oblique first modes exhibit significantly higher growth rates and are therefore more relevant in transition. The current result suggest that wall cooling and suction can be designed focusing primarily on the most unstable oblique case. However, porous coatings and grooves should be analyzed for both planar and oblique first modes, as they have significantly different effects on planar and oblique first modes.

Chapter 4 Stabilization Mechanisms of Crossflow Mode

Stabilizing methods of traveling crossflow modes are then examined. The stabilization mechanisms are discussed with MPT, and some parallel stabilization characteristics between oblique first Mack and traveling crossflow modes are further discussed. This chapter is reorganized based on my article published in the *AIAA Journal*, titled "Stabilization Mechanisms of Traveling Crossflow Mode in Hypersonic Swept Wing Flows".

4.1. Problem Description

This work concerns the crossflow instability over a spanwise-infinite swept wing. The swept wing in this study is modeled by a swept parabolic body, as in the work of Mack and Schmid[114] and Xu et al.[32]:

$$x^* = \frac{(y^*)^2}{2R^*} \quad \text{and} \quad R^* = 10\text{mm} \tag{4.1}$$

where R^* is the radius of the leading edge. Figure 4-1 depicts the schematic of the geometry and problem formulation. The Cartesian coordinates (x, y, and z) and the local body-fitted coordinates (s, η, and z) are also defined in Figure 4-1. For laminar control, wall cooling is applied on the whole surface, while the regions of wall suction and grooves are located between x^* = 60 mm and x^* = 80 mm (corresponding to s^* = 72.2–92.9 mm). The freestream conditions are consistent with those used by Xu et al.[32], as summarized in Table 4-1. The adiabatic wall condition is implemented. The case with the adiabatic wall condition and no control techniques is set as the baseline case.

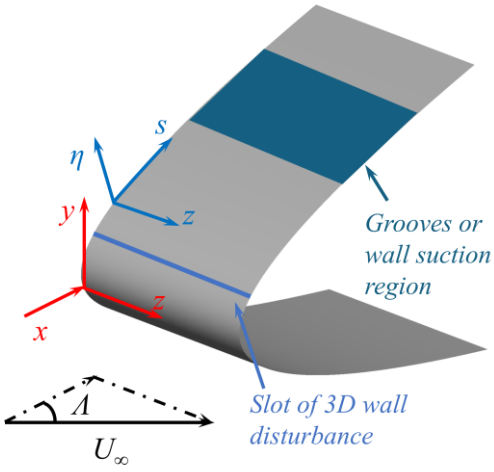

Figure 4-1 Schematic of the geometry and problem formulation.

Table 4-1 Freestream conditions.

Ma	Re_∞	T_∞^*	Λ
6	8×10^6 m^{-1}	57 K	45°

Spatial LST is used to capture the unsteady modes in this hypersonic flow. The contour of the spatial growth rate at s^* = 60 mm is presented in Figure 4-2(a). The reference length L^* is defined as:

$$L^* = \sqrt{\frac{\mu_\infty^* s^*}{\rho_\infty^* V_\infty^*}} \tag{4.2}$$

The most significantly amplified traveling crossflow instability occurs for F^* = 13 kHz and λ_z^* = 7.5 mm. Thus, this is chosen as the objective perturbation. The spatial growth rate of this crossflow mode is depicted in Figure 4-2(b). Within the computational domain, the traveling crossflow wave exhibits continuous amplification.

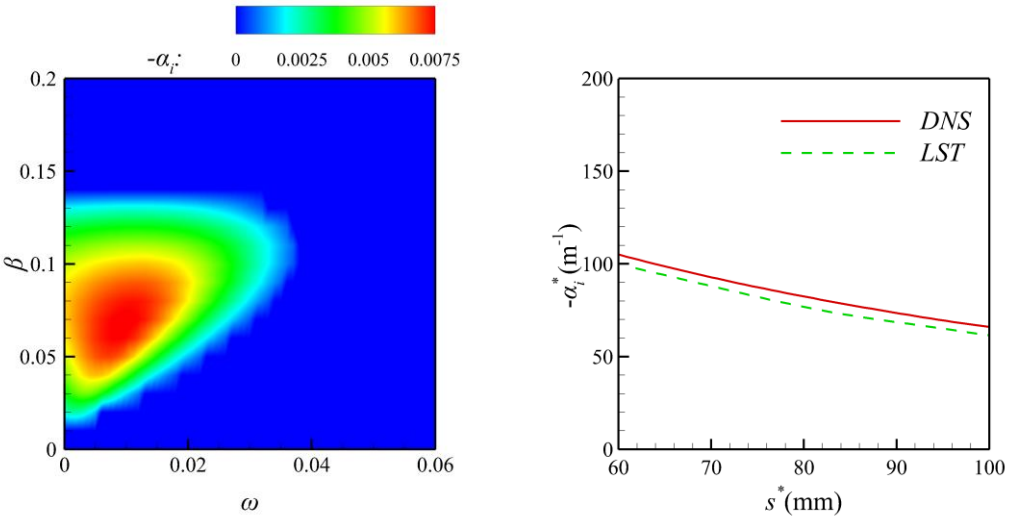

(a) spatial growth rate contour at s^* = 60 mm (b) growth rate of the objective perturbation

Figure 4-2 Spatial growth rate from LST.

In the simulations of the perturbation field, as shown in Figure 4-1, a 3D perturbation is introduced by periodic suction-blowing through a slot positioned near the leading edge, with a form close to that used in Ref. [34]:

$$q_w(x^*, z^*, t^*) = A_p e^{-\sigma[(x^*-x_{cc}^*)/\Delta x^*]^2} \cos(\frac{2\pi}{\lambda_z^*} z^*) \sin(2\pi F^* t^*) \tag{4.3}$$

where $q_w = \rho_w v_w$ represents the mass flux in the wall-normal direction. The perturbation is centered at x^*_{ce} = 8 mm and has a spatial extent of Δx^* = 4 mm. σ is a constant that determines the width of the suction-blowing perturbation; for this study, σ = 3. The forcing amplitude A_p is set to 10^{-8} to ensure the linear evolution of perturbations. As depicted in Figure 4-2(b), there is good consistency between the results obtained from DNS and those predicted by LST. The slight disparity between the DNS and LST results is due to the parallel flow assumption.

Figure 4-3(a) illustrates the instantaneous streamwise velocity fluctuation u' at s^* = 60 mm, and Figure 4-3(b) depicts the instantaneous iso-surface of u' disturbance at u' = $\pm 10^{-5}$ in the flow field. The distribution of u' closely resembles the contours of u' in the crossflow mode reported by Haas et al.[115]. Both the consistency of the spatial growth rate and the contour of u' confirm that the 3D disturbance from the slot successfully evolves to the objective traveling crossflow mode.

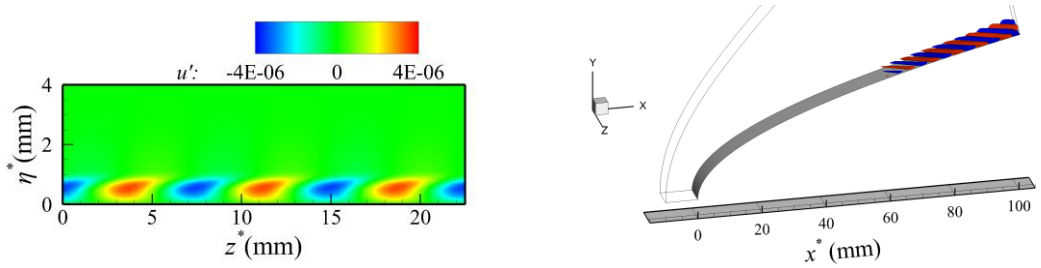

(a) contour of instantaneous u' at s^* = 60 mm (b) the iso-surface of u' disturbance

Figure 4-3 Evolutions of disturbances from DNS.

The validation of grid independence is carried out using a fine grid (417×401×31) and a coarse grid (321×301×21). The growth rates of both grids and the LST result are plotted in Figure 4-4. The growth rates in these two cases are highly consistent. The slight disparity between DNS and LST is due to the parallel flow assumption. Hence, the grid independence is confirmed, and the coarse grid can be used for calculations.

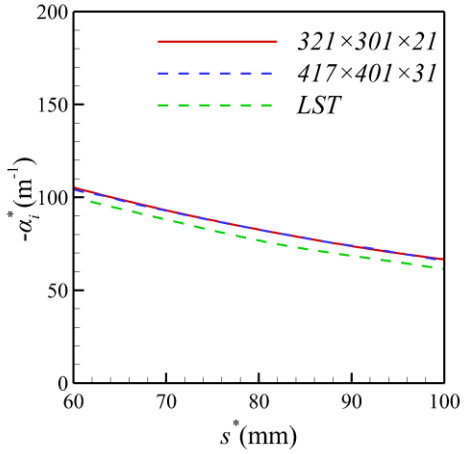

Figure 4-4 Spatial growth rates in the baseline case using different grids.

4.2. Stabilization of Crossflow Mode

The impacts of laminar control techniques on baseflows, such as the reduction of the crossflow velocity and the movement of the GIP[116–119], are regarded as the source of the stabilization effects. In this section, the details of laminar control techniques are introduced, before the impacts on baseflows and the stabilization effects are discussed.

4.2.1. Wall cooling-heating

In the present study, laminar control through wall cooling is applied by changing the temperature of the whole solid wall. Two cooled-wall cases and a heated-wall case are considered, with wall temperatures prescribed at $0.5\,T_r^*$ = 210.9 K, $0.8\,T_r^*$ = 337.5 K, and $1.2\,T_r^*$ = 506.2 K. The wall recovery temperature T_r^* is computed by

$$T_r^* = T_e^*\left(1+\frac{\gamma-1}{2}M_e^2\sqrt{Pr}\right) \tag{4.4}$$

where T_e^* and M_e represent the temperature and Mach number at the outer edge of the boundary layer at x^* = 70 mm.

The influence of wall temperature on the baseflow is first examined. The temperature, crossflow velocity, $d(\rho\, du/d\eta)/d\eta$, and $d^2u_c/d\eta^2$ are plotted in Figure 4-5. The crossflow velocity u_c is the velocity component that is perpendicular to the direction of the inviscid streamline. The last two variables are used to identify the position of the GIP (where $d(\rho\, du/d\eta)/d\eta$=0) and the crossflow inflection point (CFIP, where $d^2u_c/d\eta^2$=0), respectively. In Figure 4-5(c) and (d), black dashed lines denote the

zero value to facilitate the identification of the GIP and the CFIP. Wall cooling strongly alters the temperature distribution near the wall. The magnitude of crossflow velocity exhibits a corresponding decrease. From Figure 4-5(c) and (d), both the GIP and CFIP are shifted towards the wall when the wall temperature decreases. The maximum crossflow velocity and the position of the GIP and CFIP change almost linearly with respect to the wall temperature.

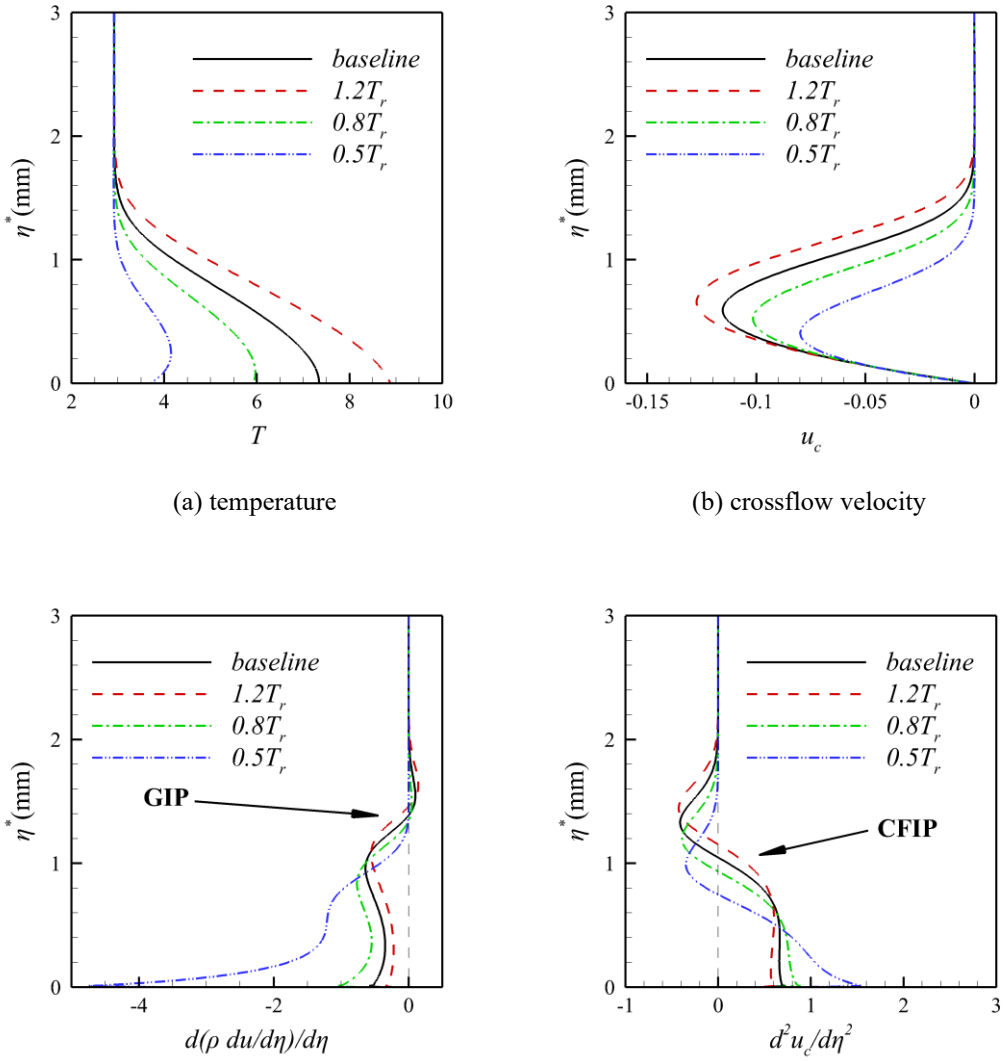

(a) temperature

(b) crossflow velocity

(c) $d(\rho\, du/d\eta)/d\eta$

(d) $d^2u_c/d\eta^2$

Figure 4-5 Baseflow quantities at $s^* = 80$ mm in wall cooling cases.

The linear growth of the traveling crossflow mode is quantified by the N factor, which is defined in terms of the localized maximum streamwise velocity fluctuation $u'_{\max}$ obtained from DNS:

$$N = \ln(u'_{\max} / u'_{ce,\max}) \tag{4.5}$$

where $u'_{ce,\max}$ is the maximum streamwise velocity perturbation at the center of the disturbance slot. The N factors of the baseline and wall cooling cases are plotted in Figure 4-6 to assess the influence of the laminar control techniques.

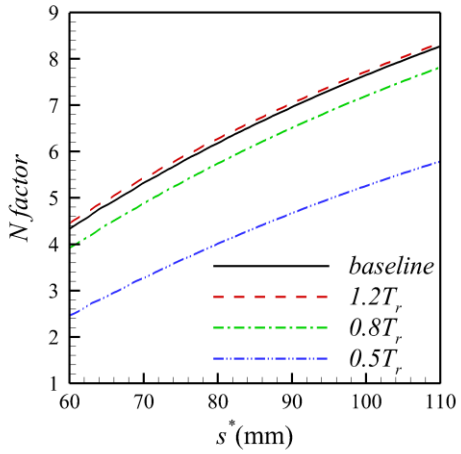

Figure 4-6 N factors in wall cooling cases.

There is a notable reduction in the N factor in Figure 4-6. The N factor decreases by more than 2 when the wall temperature is set to $0.5T_r$. This emphasizes the efficacy of wall cooling as a stabilizing technique. In contrast, the application of wall heating results in the destabilization of the traveling crossflow mode.

4.2.2. Wall blowing-suction

Steady wall blowing and suction are considered in the form of mass flux as shown in equation (3.4). A large suction coefficient of $A_s = 0.001$ is utilized for the wall suction case, whereas $A_s = -0.001$ is employed for the wall blowing case. As depicted in Figure 4-1, the blowing-suction region is located between $x^* = 60$ mm and $x^* = 80$ mm.

Constant wall suction removes the low-energy fluid at the solid surface and may stabilize the boundary layer. The baseflow quantities in the wall blowing-suction cases are plotted in Figure 4-7. Black dashed lines in Figure 4-7(c) and (d) denote the zero value. The GIP and CFIP are all closer to the wall when wall suction is applied. The crossflow velocity increases in this case. Wall blowing has the opposite effect on the baseflow.

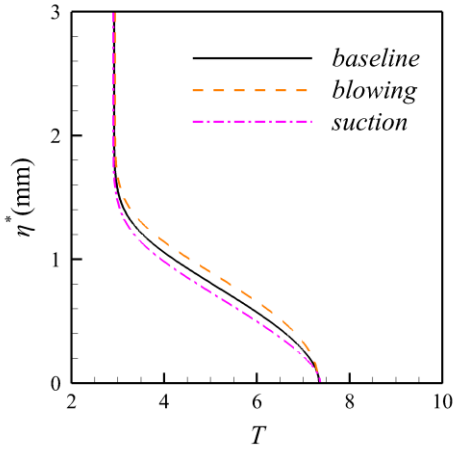

(a) temperature

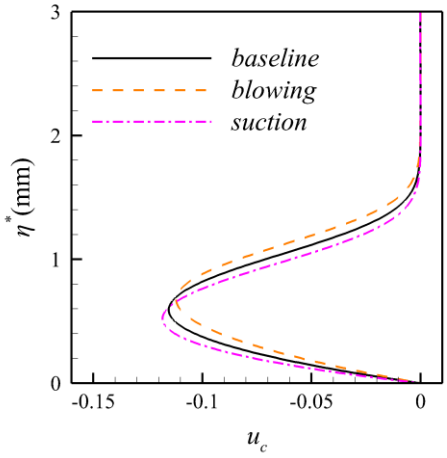

(b) crossflow velocity

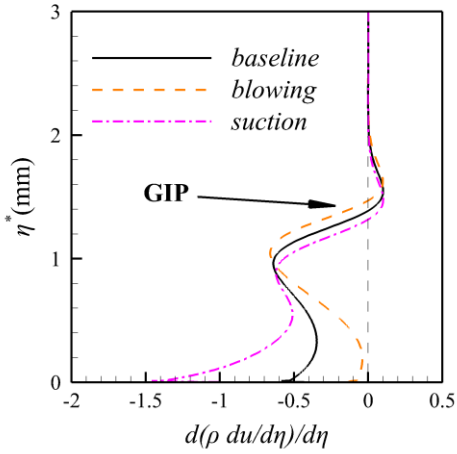

(c) $d(\rho\, du/d\eta)/d\eta$

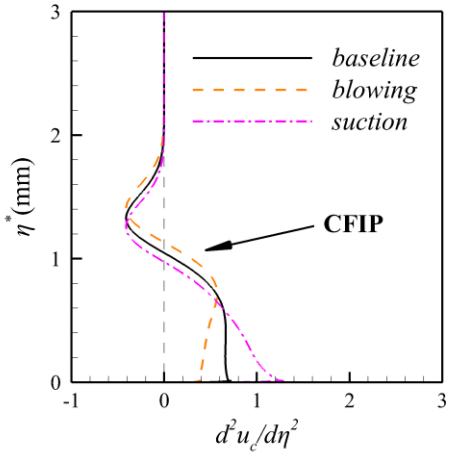

(d) $d^2u_c/d\eta^2$

Figure 4-7 Baseflow quantities at $s^* = 80$ mm in wall suction cases.

The N factors of the blowing-suction cases are depicted in Figure 4-8. The results indicate that wall blowing and suction both have only a marginal influence on the crossflow waves, with the observed variation in the N factor being on the order of 0.1. Wall suction provides only a slight stabilization effect on the traveling crossflow waves. A reduction in the N factor is associated with an increase in u_c.

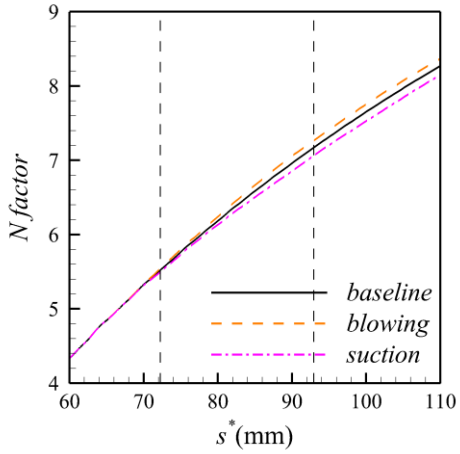

Figure 4-8 N factors in wall suction cases.

4.2.3. Porous coatings

Porous coatings with different admittance phases θ = 0.5π, 1π, and 1.5π are designed using the admittance equation proposed by Zhao et al.[93]. Figure 4-9 presents definitions of the porous coating parameters, where shadowed regions denote solid walls. Table 4-2 details coating geometric parameters, admittance values, and corresponding LST-predicted growth rates for the crossflow mode at s^* = 80 mm. The coatings are labeled according to their respective θ values. Stabilizing or destabilizing effects relative to the no-coating case are indicated alongside the LST growth rates. According to LST predictions, porous coatings strongly stabilize the crossflow mode when θ = 0.5π, slightly stabilize the crossflow mode when θ = π, but destabilize the crossflow mode when θ = 1.5π.

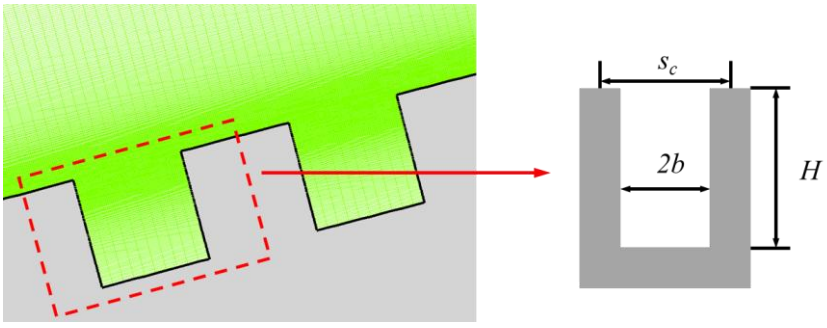

Figure 4-9 Definitions of porous coating and groove parameters.

Table 4-2 Porous coating parameters.

	$\theta = \pi$	$\theta = 0.5\pi$	$\theta = 1.5\pi$
b /m	2×10^{-4}	2.5×10^{-4}	9×10^{-4}
H /m	8×10^{-3}	2.5×10^{-3}	1.06×10^{-2}
aspect ratio	0.05	0.2	0.17
porosity	0.5	0.5	0.5
Admittance	−9.007+0.128i	−1.228+5.310i	−2.976+8.942i
LST	0.00723 (−8.6%)	0.00352 (−55.4%)	0.00902 (14.0%)

The N factors of porous-coating cases are illustrated in Figure 4-10. The beginning and end of porous coatings are marked by the vertical dark dashed lines. DNS results demonstrate notable discrepancies from LST predictions: Coatings $\theta = \pi$ and 0.5π exhibit marginal influence on the crossflow mode, while coating $\theta = 1.5\pi$ stabilizes the crossflow mode. These stabilizing effects appear correlated with the coating's geometric dimensions.

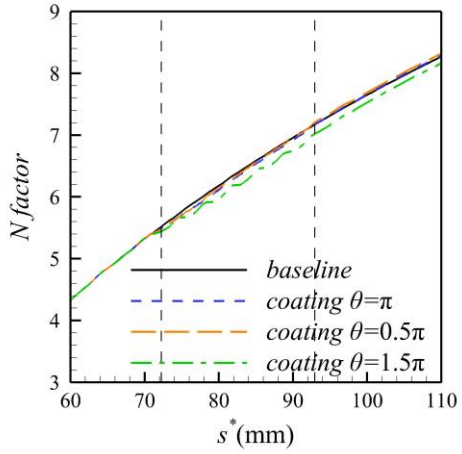

Figure 4-10 N factor in porous coating cases.

The flow quantities are averaged over one porous coating period around $s^* = 80$ mm. The average flow quantities are depicted in Figure 4-11. Porous coatings marginally influence the average baseflow characteristics except for a small region near the wall.

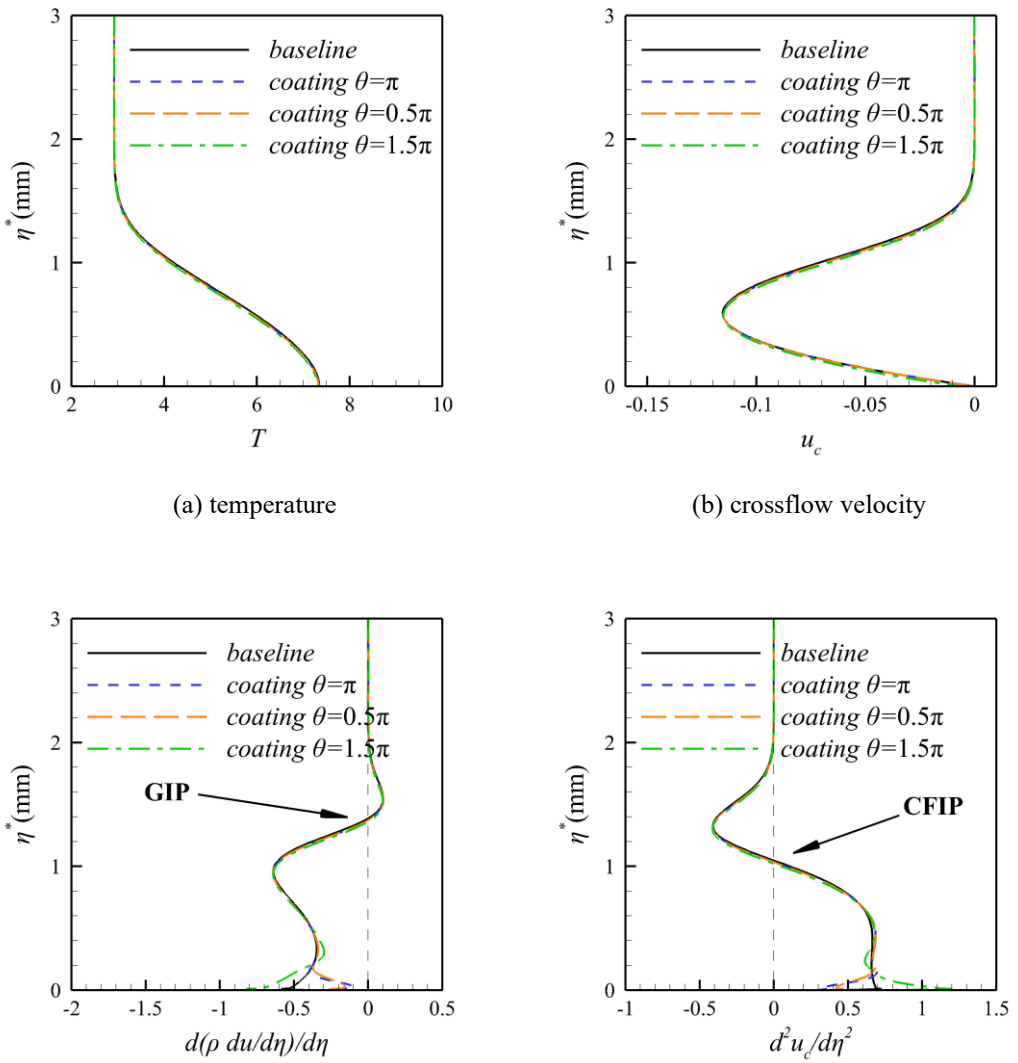

(a) temperature

(b) crossflow velocity

(c) $d(\rho\, du/d\eta)/d\eta$

(d) $d^2u_c/d\eta^2$

Figure 4-11 Average baseflow quantities at $s^* = 80$ mm in porous coating cases.

Adopting the analytical framework from Sec. 3.3.3, LST is applied to the distorted baseflows to investigate correlations between baseflow distortion and growth rates. Although first Mack and crossflow modes share the same nature, a distinct LST strategy from the first mode yields better predictions. For crossflow modes, LST analysis excludes cavity flow fields, focusing solely on distorted baseflows, as depicted in

Figure 4-12. The LST-predicted growth rates and baseflow pressure contours are depicted in Figure 4-13. From baseflows, low-pressure regions are induced by the expansion waves at beginnings of open cavities, while weak compression waves are formed at ends of cavities. In small half-width cases (θ = π and θ = 0.5π), weak compression and expansion waves are generated, confining mean-flow pressure disturbances to small near-wall regions. Growth rates are lower than or equal to the values in the baseline case. The growth rates decline in solid wall regions and recover at each cavity. The large half-width case (θ = 1.5π) produces intensified compression and expansion waves that significantly alter off-wall pressure distributions. The changes in growth rate become stronger and can exceed baseline values at compression wave positions. Enhanced stabilization effects in the larger half-width case correlate with changes in N factors near s^* = 80 mm in Figure 4-10. These agreements between LST and DNS results confirm that baseflow distortions, not wall admittance, drive the stabilization of crossflow instabilities, while the flows in the cavities are less important compared to first Mack modes.

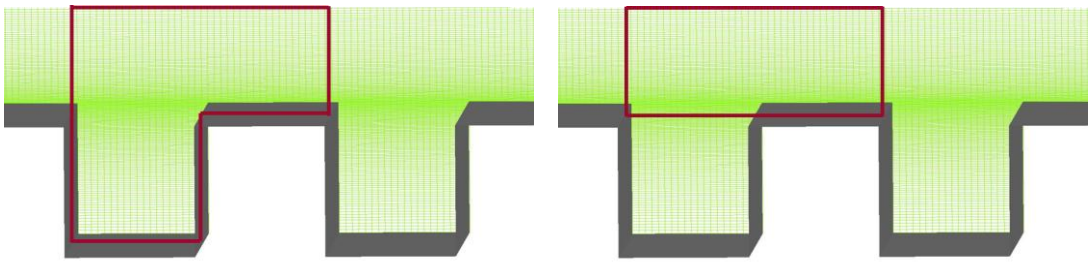

(a) first mode LST region (b) crossflow mode LST region

Figure 4-12 Schematic of LST regions for different modes.

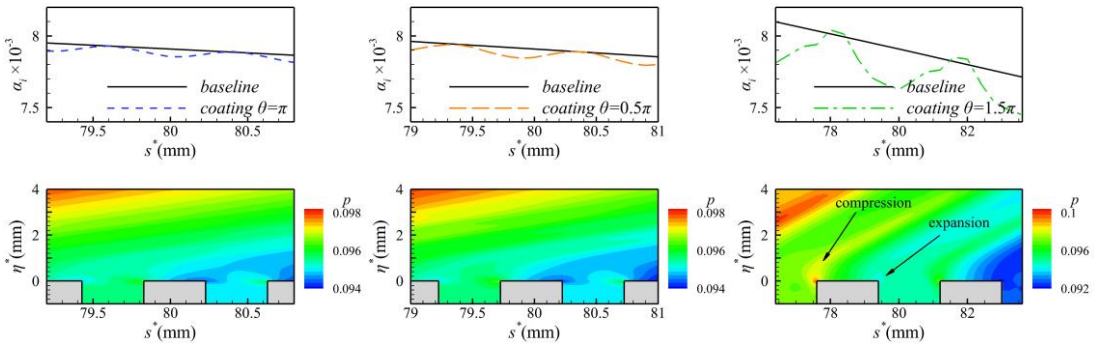

(a) case $\theta = \pi$ (b) case $\theta = 0.5\pi$ (c) case $\theta = 1.5\pi$

Figure 4-13 Growth rates from LST and baseflow pressure contours of porous-coating cases.

4.2.4. Grooves

The stabilizing effects of parallel grooves, located between $x^* = 60$ mm and $x^* =$ 80 mm, are investigated in the current study. Groove parameters are defined in consistent with Figure 4-9. For all grooved cases, the period s_c is set to $2\delta^* = 4.32$ mm, where δ^* is the boundary-layer thickness at $x^* = 60$ mm, distinguished by $dw/d\eta < 0.01$. This criterion is close to the mean-shear-based methods in Ref. [120]. The groove widths and heights are varied to determine the optimal control effect.

The investigation first focuses on the impact of the cavity half-width. The cavity height H is maintained at δ^*, while the half-width varies as follows: $0.05\delta^*$ (case *H1b0.05*), $0.25\delta^*$ (case *H1b0.25*), $0.5\delta^*$ (case *H1b0.5*), $0.75\delta^*$ (case *H1b0.75*), $0.9\delta^*$ (case *H1b0.9*). The grid dimensions for the narrowest groove are specified as 8 × 178 (width × depth) for each cavity, while the widest groove has grid dimensions of 31 × 178. The grid convergence for the grooved cases is illustrated in Figure 4-14. The *H1b0.5* case is selected as the test case. The grid in each cavity is changed from 11 × 178 × 21 to 16 × 267 × 21. There is no visible difference between the results using these two grids. The corresponding N factors are plotted in Figure 4-15(a). In the grooved regions, only case *H1b0.9* amplifies the crossflow mode. After the grooved regions, all the grooves stabilize the crossflow mode. The N factors at $s^* = 110$ mm are summarized in Figure 4-16, with a spline drawn to show the trend. As shown in Figure 4-16(a), the maximum stabilization effect is achieved when $b = 0.5\delta^*$. Beyond this width, the stabilization effect diminishes.

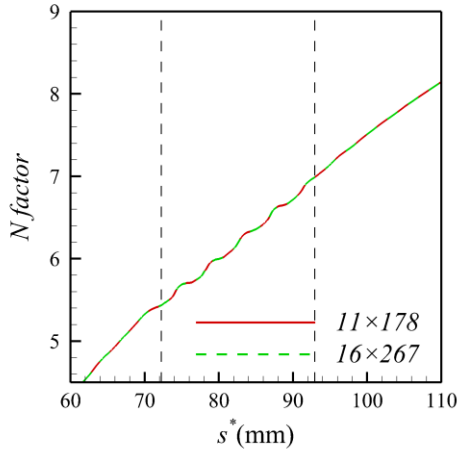

Figure 4-14 N factors in the *H1b0.5* case using different grids.

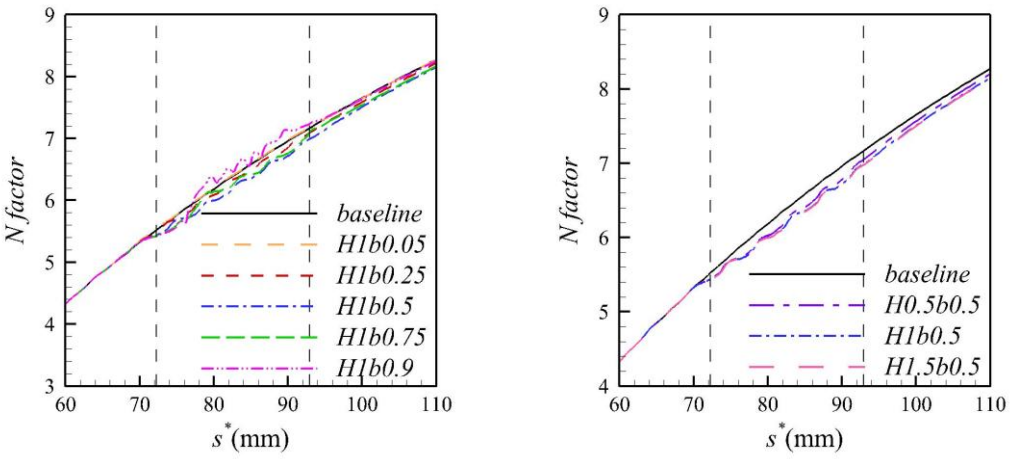

(a) grooved cases with different widths (b) grooved cases with different heights

Figure 4-15 N factor in grooved cases.

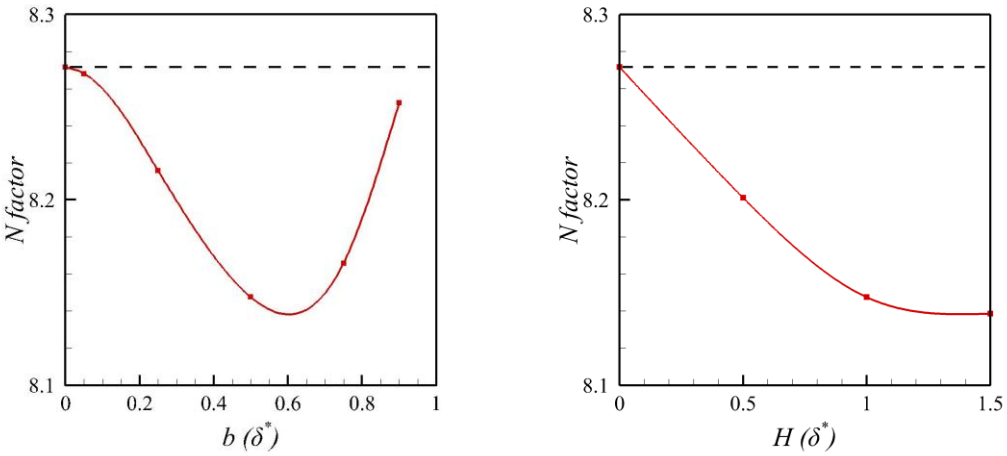

(a) $H=\delta^*$ (b) $b=0.5\delta^*$

Figure 4-16 N factor at $s^* = 110$ mm.

The influence of the cavity height is studied with $b = 0.5\delta^*$ and heights of $0.5\delta^*$ (case *H0.5b0.5*), $1.0\delta^*$ (case *H1b0.5*), and $1.5\delta^*$ (case *H1.5b0.5*). The shallowest groove has grid dimensions of 11 × 123 for each cavity, while the deepest groove has grid dimensions of 11 × 216. The N factors are plotted in Figure 4-15(b) and Figure 4-16(b). All cases exhibit a stabilizing effect on the crossflow modes, both during and after the grooved regions. The control effect is positively correlated with the cavity height, while the slope becomes small after $H = \delta^*$.

Across all grooved cases, the variations in the N factor are on the order of 0.1,

suggesting that the traveling crossflow waves are moderated by the grooves. Although the stabilizing effect is small, it is interesting to consider why the traveling crossflow mode is stabilized and why the control effect is maximized when $W = \delta^*$. Hence, the baseflows of the *H1b0.5* case and the *H1b0.9* case are analyzed to provide a possible interpretation. The LST-predicted growth rates and pressure contours are depicted in Figure 4-17. As shown, the grooves generate expansion waves at beginnings of cavities, while compression waves form at the ends. Growth rates decrease in low-pressure regions but recover at compression wave positions. This behavior closely resembles the large half-width porous coating case (θ = 1.5π), indicating shared stabilization mechanisms between porous coatings and grooves when the half-width is large. For case *H1b0.9*, LST results significantly diverge from DNS results, suggesting non-parallel effects and cavity-related motions become critical in these oversized cavities. Except for the baseflow distortion, local scattering effects at solid-cavity and cavity-solid junctions constitute an additional mechanism for both porous coatings and grooves, producing the wavy patterns of N factors in the controlled cases. The detailed mechanisms need further investigation with MPT.

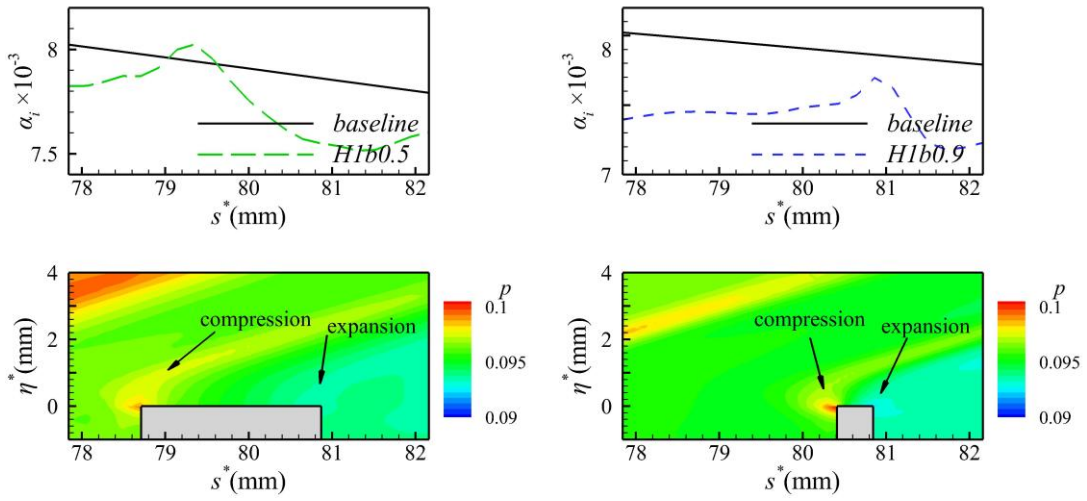

(a) case *H1b0.5* (b) case *H1b0.9*

Figure 4-17 Growth rates from LST and baseflow pressure contours of grooved cases.

The flow quantities are averaged across one groove period at around s^* = 80 mm. The average flow quantities are plotted in Figure 4-18. Black dashed lines in Figure 4-18 (c) and (d) denote the zero value. The flow quantities shift towards the wall under the influence of the grooves, while the maximum crossflow velocity is unchanged.

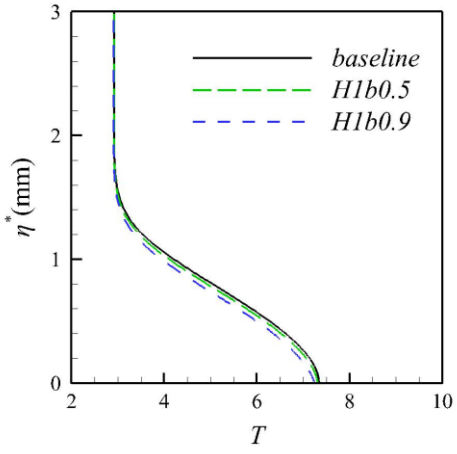

(a) temperature

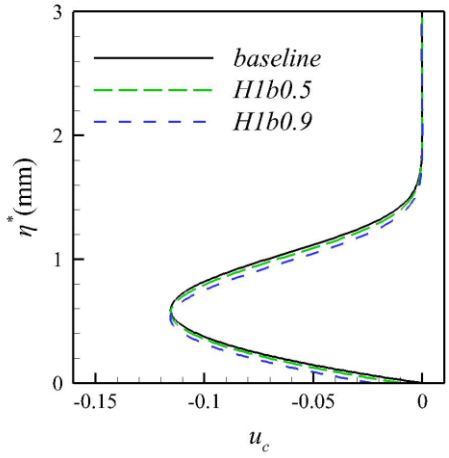

(b) crossflow velocity

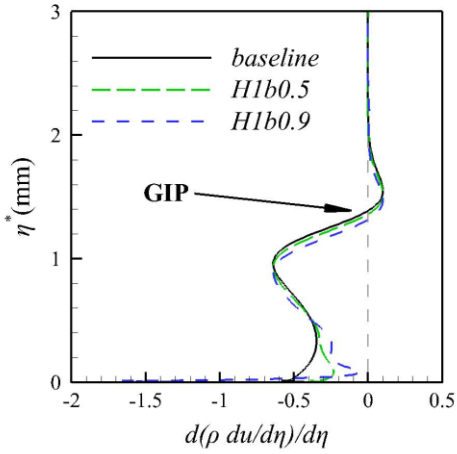

(c) $d(\rho\, du/d\eta)/d\eta$

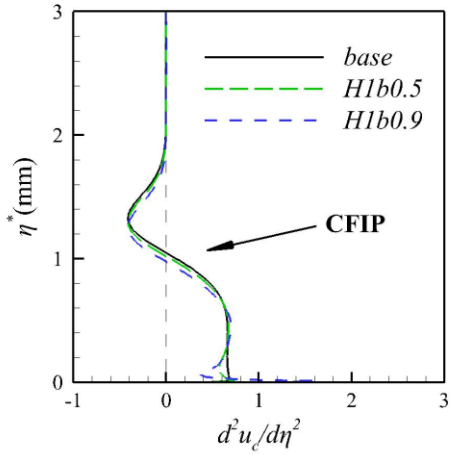

(d) $d^2u_c/d\eta^2$

Figure 4-18 Average baseflow quantities at s^* = 80 mm in grooved cases.

4.3. MPT Analysis of Stabilization Mechanisms

4.3.1. Wall cooling-heating

The $0.8T_r$ case is analyzed in the MPT framework. To analyze the characteristics of the traveling crossflow mode, the fluctuation momentum density is decomposed into the instantaneous MPT components. Snapshots of the acoustic component $\boldsymbol{m'}_A$, vortical component $\boldsymbol{m'}_B$, and thermal component $\boldsymbol{m'}_T$ in the baseline case and the $0.8T_r$ case are plotted in the local body-fitted coordinates in Figure 4-19. The upper lines are the boundary layer edge; the middle lines are the GIP, and the lower lines are

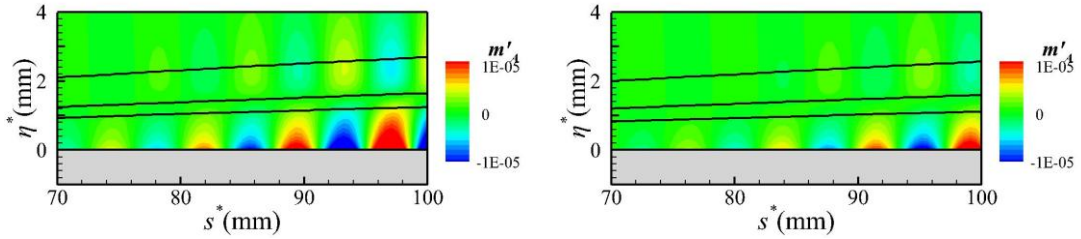

(a) acoustic component in the baseline case

(b) acoustic component in $0.8T_r$ case

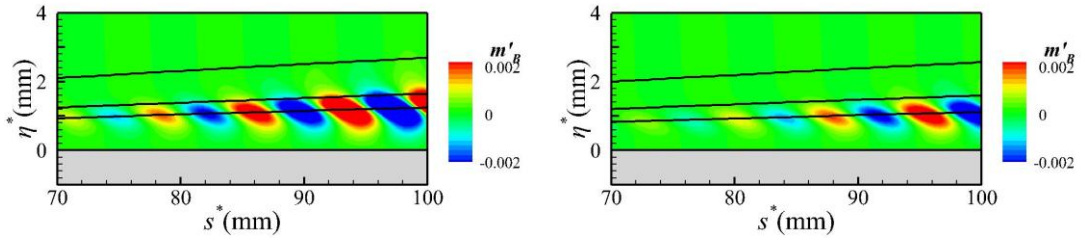

(c) vortical component in the baseline case

(d) vortical component in $0.8T_r$ case

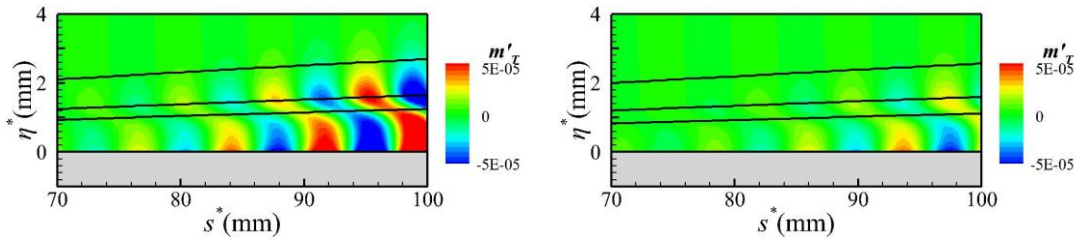

(e) thermal component in the baseline case

(f) thermal component in $0.8T_r$ case

Figure 4-19 The instantaneous snapshots of MPT components.

the CFIP in Figure 4-19. For the baseline case, the vortical component $\boldsymbol{m'_B}$ associated with the traveling crossflow wave exhibits the largest magnitude, while $\boldsymbol{m'_A}$ is the smallest. "Two-cell" structures can be observed for $\boldsymbol{m'_A}$ and $\boldsymbol{m'_T}$, whereas the vortical field is characterized by "single-cell" structures. Furthermore, $\boldsymbol{m'_B}$ is several orders of magnitude greater than $\boldsymbol{m'_A}$ and $\boldsymbol{m'_T}$. This significant disparity in the magnitude of the MPT components highlights the vortical nature of the crossflow instability. The GIP reflects the phase shift of $\boldsymbol{m'_A}$ in the wall-normal direction, whereas the CFIP indicates the peak value of $\boldsymbol{m'_B}$ and the phase shift of $\boldsymbol{m'_T}$, emphasizing the significance of the crossflow velocity in the traveling crossflow mode. Comparing the contours of the baseline case and the $0.8T_r$ case, the three components for the cold wall behave in a similar manner to the adiabatic wall case, albeit with much smaller magnitudes. Specifically, the single-cell and two-cell structures are still apparent in Figure 4-19 (b), 11(d), and 11(f). The peak value of $\boldsymbol{m'_B}$ and the phase

shift of $\boldsymbol{m}'_T$ are still located in the vicinity of the CFIP.

As discussed in Sec. 3.3.1, the variations in the wavelength of the MPT components are indicative of the sensitivity of a certain component to the stabilization technique. In this section, the spanwise wavelength of the perturbations remains constant at λ_z^* =7.5 mm. The wavelengths λ_s^* in the *s*-direction of the perturbations (evaluated and represented by u') and the corresponding MPT components are summarized in Table 4-3. The averaged streamwise wavelengths of the crossflow mode (and MPT components) are obtained by examining the periodicity of u', $\boldsymbol{m}'_A$, $\boldsymbol{m}'_B$, and $\boldsymbol{m}'_T$ at η^* = 1 mm within the groove or wall suction region (x^* = 60~80 mm), considering η^* = 1 mm is approximately the height of CFIP. From the change in the wavelength of u', larger-wavelength traveling crossflow modes are more likely to be amplified under low-wall-temperature conditions. For the MPT components, the change in $\boldsymbol{m}'_T$ is the most significant among all MPT components under wall cooling (i.e., 9% difference compared with the baseline case). This difference is related to the change in the baseflow, as shown in Figure 4-5. This variation in the MPT components suggests that reducing the wall temperature stabilizes the traveling crossflow waves directly through the thermal component, while the acoustic and vortical components are subsequently changed.

Table 4-3 Comparison of λ_s^* between the baseline case and the wall cooling case.

λ_s^* (mm)	u'	$\boldsymbol{m}'_A$	$\boldsymbol{m}'_B$	$\boldsymbol{m}'_T$
Baseline	7.68	7.66	7.68	8.00
Wall cooling	7.83	7.38	7.83	8.72
Proportion	1.95%	−3.66%	1.95%	9.00%

The magnitudes of the MPT components in the baseline and $0.8T_r$ cases at s^* = 80 mm are depicted in Figure 4-20. The boundary layer edge (solid lines) and the CFIP (dashed lines) are plotted to allow the wall-normal position to be identified in Figure 4-20. When reducing the wall temperature, all the MPT components slightly towards the wall. This can be attributed to the thinner boundary layer and lower GIP at lower wall temperatures. $\|\boldsymbol{m}'_B\|$ and $\|\boldsymbol{m}'_T\|$ become significantly smaller, indicating that less fluctuating momentum is transported off the wall in the form of vortical and thermal components. MPT components show similar changes with those in the highly oblique first mode (Sec. 3.4.1).

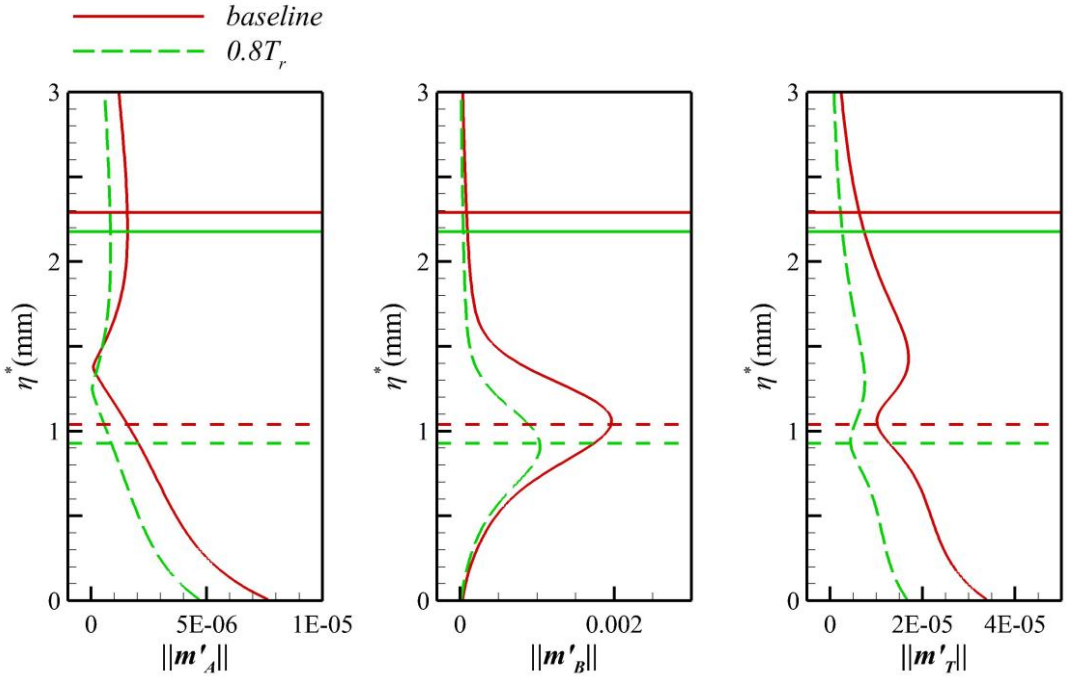

(a) acoustic component (b) vortical component (c) thermal component

Figure 4-20 The amplitudes of MPT components in the $0.8T_r$ case.

4.3.2. Wall blowing-suction

The wall suction case with A_s =0.001 is analyzed in the MPT framework. From Figure 4-21, neither the instantaneous behaviors nor the magnitudes of the MPT components exhibit significant changes. The boundary layer edge (upper lines), the GIP (middle lines), and the CFIP (lower lines) are plotted in Figure 4-21. From Table 4-4, a larger wavelength of the traveling crossflow mode is identified under wall suction. The wavelength of $\boldsymbol{m'}_B$ obviously increases, while the other two components remain relatively unchanged. This result suggests that wall suction predominantly impacts the vortical component.

Table 4-4 Comparison of λ_s^* between the baseline case and the wall suction case.

λ_s^* (mm)	u'	$\boldsymbol{m'}_A$	$\boldsymbol{m'}_B$	$\boldsymbol{m'}_T$
Baseline	7.68	7.66	7.68	8.00
Wall suction	7.98	7.68	7.98	7.98
Proportion	3.91%	0.26%	3.91%	−0.25%

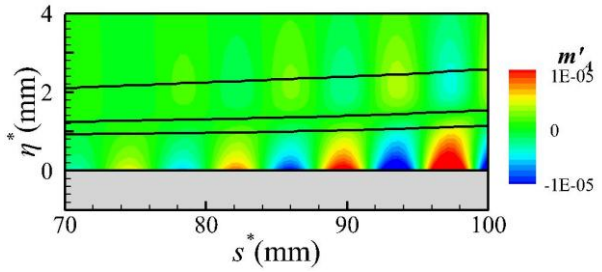

(a) acoustic component

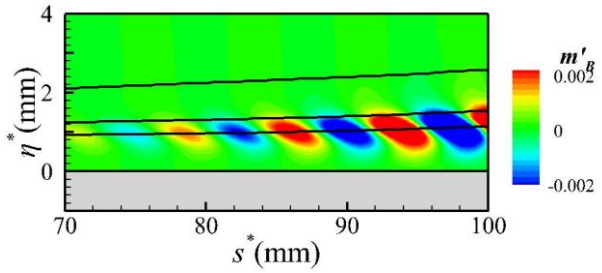

(b) vortical component

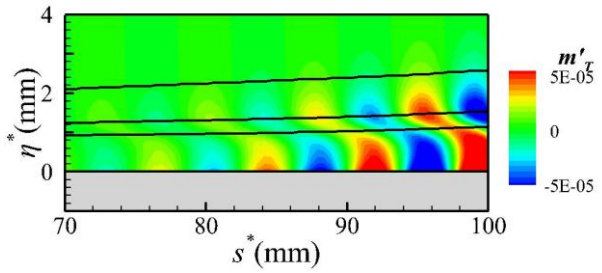

(c) thermal component

Figure 4-21 The instantaneous snapshots of MPT components in wall suction cases.

The magnitudes of the MPT components are depicted in Figure 4-22. All the components shift slightly towards the wall, which aligns with the change in the baseflow. The peak value of $\|\boldsymbol{m}'_B\|$ slight decreases, while those of $\|\boldsymbol{m}'_A\|$ and $\|\boldsymbol{m}'_T\|$ remain nearly unchanged. These changes in MPT components align with those in the highly oblique first mode (Sec. 3.4.2), except for that the thermal component of the 3D first mode is more active.

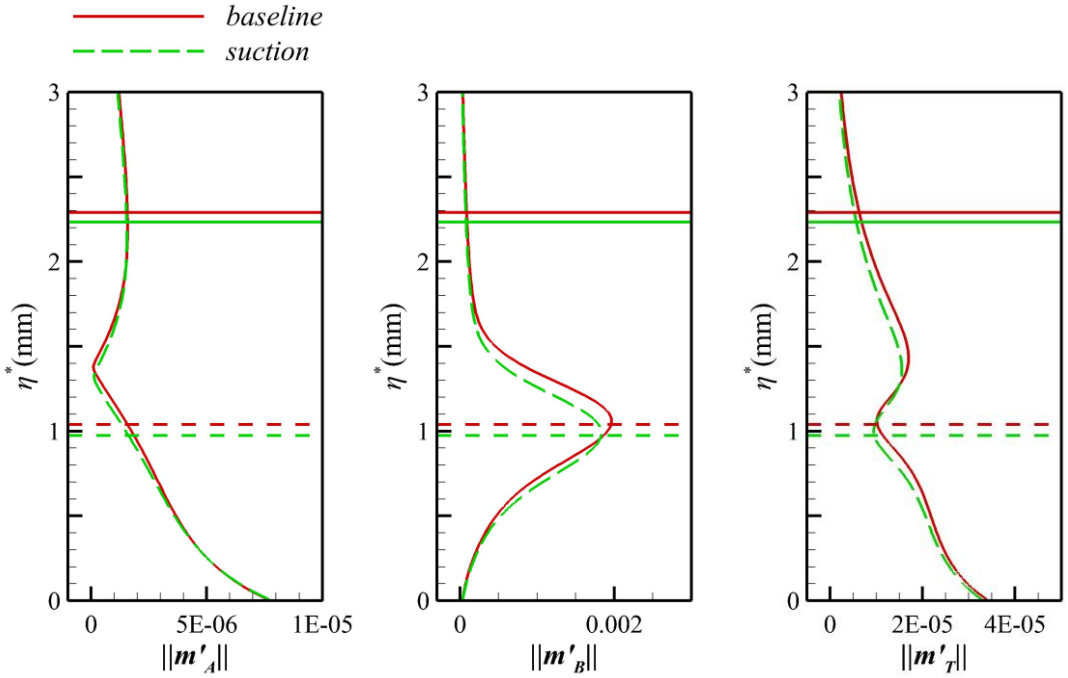

(a) acoustic component (b) vortical component (c) thermal component

Figure 4-22 The amplitudes of MPT components in the wall suction case.

4.3.3. Grooves

Considering small half-width porous coatings yield nearly no impact on traveling crossflow modes, and large half-width coatings have a highly similar stabilization mechanism with the grooves, the porous coating cases will not be analyzed with MPT. Instead, the grooved cases (*H1b0.5* and *H1b0.9*) are analyzed with MPT. The instantaneous magnitudes of the MPT components in these two cases are plotted in Figure 4-23. The upper lines are the boundary layer edge, the middle lines are the GIP, and the lower lines are the CFIP in Figure 4-23. Different from wall cooling and suction, grooves strongly alter the behavior of the MPT components. For $\boldsymbol{m'}_A$, the acoustic field is perturbed by the compression and expansion waves induced by the cavities. The two-cell structures do not even appear in the *H1b0.9* case. The $\boldsymbol{m'}_B$ component exhibits a lower sensitivity to the waves. The single-cell structure persists in these cases, although some deformations can be observed in Figure 4-23(c) and (d). The $\boldsymbol{m'}_T$ component appears to be relatively unaffected by the compression and expansion waves. Instead, it moves down towards the cavity due to the lack of a solid wall. The wavelengths of the MPT components quantify their sensitivity to the grooves. The wavelength of $\boldsymbol{m'}_A$ undergoes the most substantial change in both cases. The change

in the wavelength of m'_B is also noteworthy. According to Table 4-5, both grooves shorten the wavelength. The wavelength of m'_A undergoes the most substantial change in both cases. The change in the wavelength of m'_B is also noteworthy.

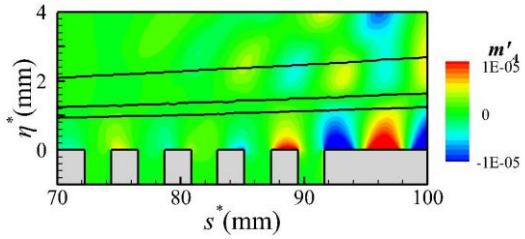

(a) acoustic component in the *H1b0.5* case

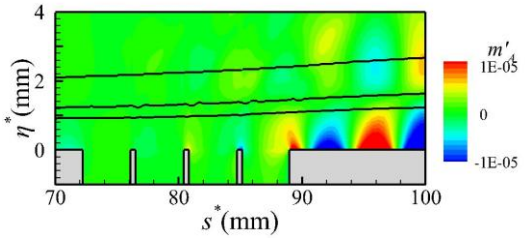

(b) acoustic component in *H1b0.9* case

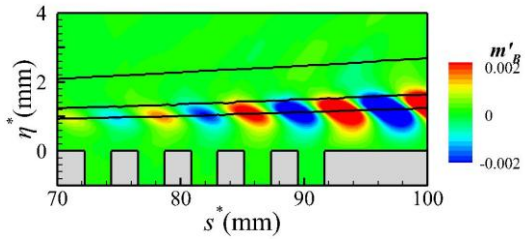

(c) vortical component in the *H1b0.5*case

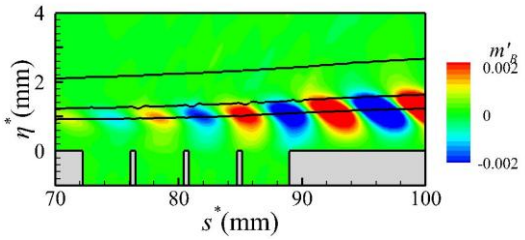

(d) vortical component in *H1b0.9* case

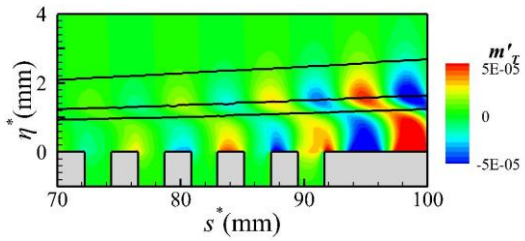

(e) thermal component in the *H1b0.5*case

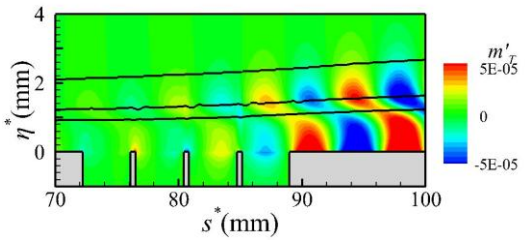

(f) thermal component in *H1b0.9* case

Figure 4-23 The instantaneous snapshots of MPT components in grooved cases.

Table 4-5 Comparison of λ_s^* between the baseline case and grooved cases.

λ_s^* (mm)	u'	m'_A	m'_B	m'_T
Baseline	7.68	7.66	7.68	8.00
H1b0.5	7.62	6.47	7.48	7.91
Proportion	−0.78%	−15.54%	−2.60%	−1.13%
H1b0.9	7.39	6.82	7.31	7.68
Proportion	−3.78%	−10.97%	−4.82%	−4.00%

Figure 4-24 depicts the magnitudes of the MPT components, with spatial averaging conducted over one groove period. In Figure 4-24, solid lines denote the boundary layer edge and dashed lines are the CFIP. For both cases, $\|\boldsymbol{m}'_A\|$ and $\|\boldsymbol{m}'_T\|$ decrease at the wall due to the lack of solid walls, while $\|\boldsymbol{m}'_B\|$ increases near the wall. In the *H1b0.9* case, $\|\boldsymbol{m}'_B\|$ has a broad distribution under the CFIP, while the peak value decreases. These trends indicate that more fluctuating momentum is transported to the cavities, while off-wall fluctuating momentum is damped due to mean flow distortions. This mechanism has also been found to be responsible for the destabilization of oblique first modes in Sec. 3.4.4.

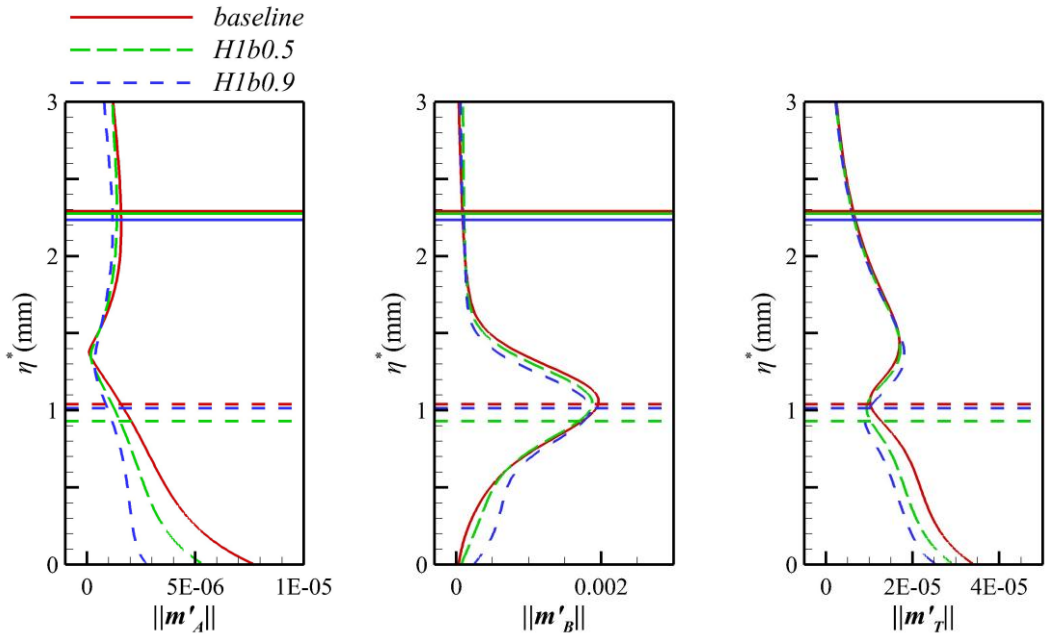

(a) acoustic component (b) vortical component (c) thermal component

Figure 4-24 The amplitudes of MPT components in grooved cases.

4.4. Summary

The traveling crossflow wave over a spanwise-infinite swept wing has been thoroughly investigated. Wall cooling, wall suction, and grooves have been used to stabilize the traveling crossflow wave. The physical properties of the traveling crossflow instability and the mechanisms of these laminar control techniques were analyzed within the MPT framework.

For the baseline case, the vortical component constitutes the largest proportion in

the traveling crossflow mode, followed by the thermal component. This dominance of the vortical component emphasizes the inherent vortical nature of the crossflow instability. Both the acoustic component and the thermal component exhibit characteristic two-cell structures, whereas the vortical component displays single-cell behavior. The center of the single cell, which also exhibits the maximum magnitude of the vortical component, is roughly aligned with the CFIP. Although the vortical component is the most important in the traveling crossflow mode, different control techniques impact various components, thereby exhibiting different stabilization mechanisms.

Wall cooling is an efficient laminar control technique. The N factor can be reduced by more than 2 when the wall temperature is set to $0.5T_r$. Analysis of the behavior and wavelengths of MPT components suggests that wall cooling primarily affects the thermal component.

Wall suction is less effective than wall cooling. A strong suction amplitude of $A_s = 0.001$ only reduces the N factor by 0.1. Wall suction shifts the flow quantities toward the wall. The vortical component is directly influenced, although its sensitivity remains relatively weak.

Porous coatings exhibit negligible influence on crossflow modes at small half-widths but impart a mild stabilization effect at large half-widths. Their stabilization mechanism is the same as that of grooves, thus they can be regarded as micro-slit grooves.

Grooves are also not particularly efficient in stabilizing the traveling crossflow mode, with the maximum reduction of the N factor being on the order of 0.1. For a groove period of $2\delta^*$, the control effect is positively correlated with the cavity height, but does not change monotonically with respect to the cavity width. The control effect reaches its maximum when the width is δ^*. MPT analysis indicates that the acoustic and vortical components are sensitive to the grooves. Baseflow distortions are identified as the primary mechanism for the stabilization effect.

These stabilization mechanisms show high similarities with the oblique first mode except for a less active thermal component, reinforcing the relationships between the oblique first and traveling crossflow instabilities.

Chapter 5 Unified Identification of First Mack and Crossflow Instabilities

After clarifying stabilization mechanisms of first Mack and crossflow modes, this chapter focuses on the long-standing conceptual debate involving the independence of the oblique first Mack and traveling crossflow instabilities. The present chapter aims to introduce a new perspective on these debates by examining the receptivity process of first and crossflow modes. As the receptivity stage explains the origins of instabilities, divergent receptivity pathways would imply independent instability mechanisms. Clarifying whether these modes share identical receptivity pathways provides new evidence for the controversy.

5.1. Problem Description

This investigation specifically examines the first Mack mode and crossflow instabilities over a spanwise-infinite swept wing, as illustrated in Figure 5-1. Here x, y, and z represent the Cartesian coordinates, and s, η, and z denote the local body-fitted coordinates, Λ is the sweep angle, U_∞ is the free-stream velocity, and k_∞ is the free-stream wave vector in the x-z plane. It should be noted that the wave angle θ_∞ is defined between the wave vector k_∞ and the free-stream velocity U_∞ to facilitate further calculations. The geometry of the biconvex airfoil is an arc, designed to sustain quasi-constant pressure gradients, with a chord length of 200 mm and a thickness of 1 mm. The 1:200 thickness-to-chord ratio ensures moderate pressure gradient ranges, as the first Mack modes are fully damped under large favorable pressure gradients. This small thickness also results in relatively small discrepancies between x and s. The free-stream conditions align with the experiment setup of Ref. [121], which are summarized in Table 5-1. The wall is modeled as no-slip and adiabatic. The sweep angle Λ ranges from 0° to 45°, enabling a systematic analysis of receptivity mechanism evolution across the first Mack mode and crossflow instabilities. This DNS framework achieves resolution fidelity via very dense grids (1281 × 501 × 21), ensuring that the interactions between the boundary layer and free-stream waves are captured exactly.

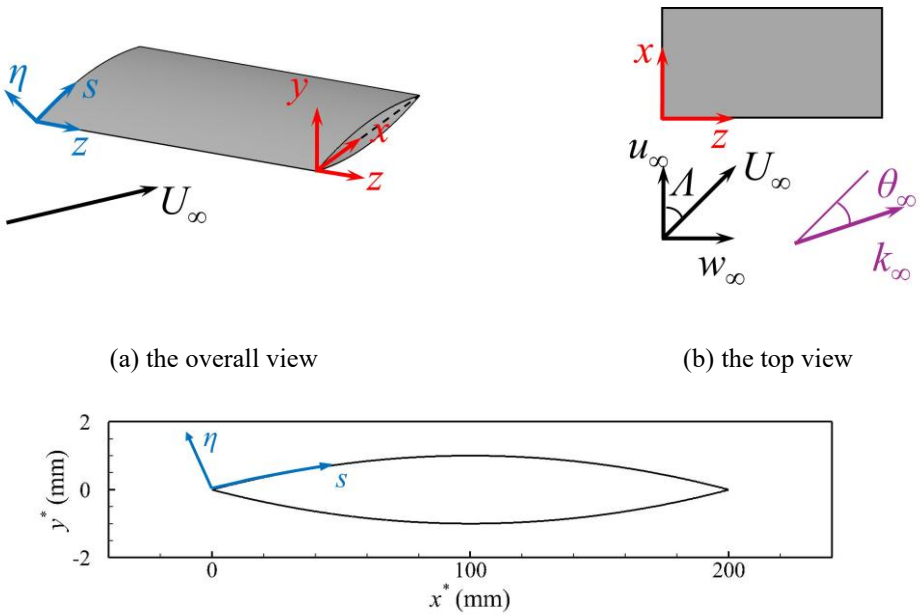

(a) the overall view (b) the top view

(c) the side view

Figure 5-1 The schematic of the spanwise-infinite swept wing and coordinate systems

Table 5-1 Free-stream conditions.

Ma	Re_∞	T_∞^*	Λ
5.9	9.15×10^7 m^{-1}	76.74 K	0°, 15°, 30°, 45°

Mach number distributions and pressure contours over the front airfoil (x^* = 0 ~ 40 mm) for the Λ = 0° case are displayed in Figure 5-2. A weak shock forms at the leading edge of the airfoil, followed by progressive pressure reduction through surface-generated expansion waves. Away from near-wall regions, Mach numbers exceed 5, maintaining hypersonic boundary layer conditions. Both first Mack mode and crossflow instabilities are examined within the hypersonic regime. Figure 5-3(a) details wall pressure p_w and streamwise pressure gradient m distributions, where pressure gradient m is calculated by:

$$m = \frac{1}{p_w}\frac{dp_w}{ds} \tag{5.1}$$

Based on this definition, negative m values denote favorable pressure gradients. As shown in Figure 5-3(a), the pressure exhibits a localized shift at the leading edge due to the shock wave, followed by a steady downstream decrease attributed to constant curvatures of the thin-wing configuration, with m achieving near-constant values. The

crossflow velocity u_c, defined as the velocity component perpendicular to the inviscid streamline, constitutes a fundamental component of crossflow instabilities. Figure 5-3(b) depicts crossflow velocity profiles across all swept cases. Elevated sweep angles induce higher crossflow velocities, suggesting that the crossflow instability is more likely to dominate the transition process with increasing sweep angles. The maximum crossflow velocity is 1.5% of the freestream velocity, which is smaller than the criterion proposed by Reed and Saric[48]. Because this criterion is proposed from low-speed scenarios, it is not applicable to the current configuration. The subsequent LST results will further confirm the existence of crossflow instability.

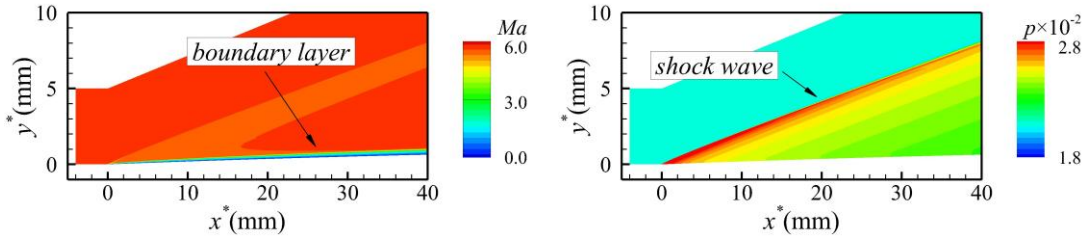

(a) Mach number (b) pressure

Figure 5-2 The baseflow contours over the front airfoil (x^* = 0 ~ 40 mm) for the Λ = 0° case.

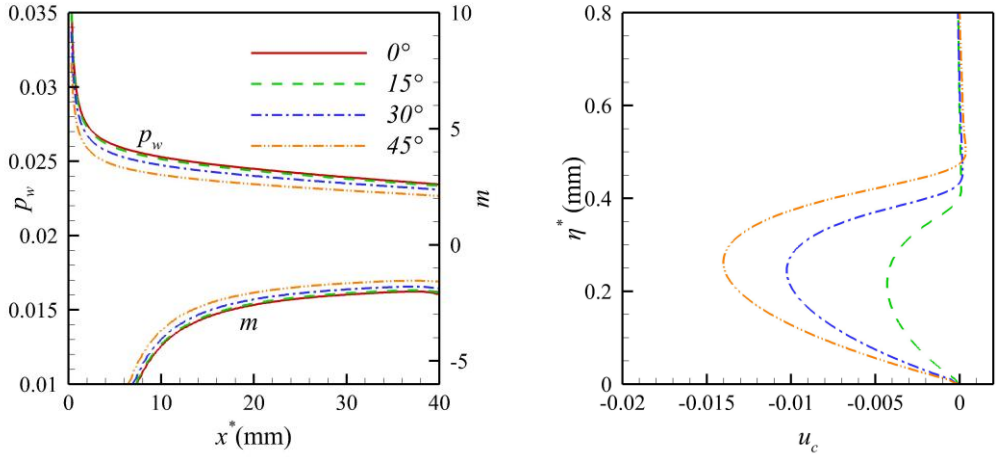

(a) Pressure and pressure gradients at the wall (b) u_c profiles at x^* = 40 mm

Figure 5-3 Baseflow variables in different cases.

5.2. Linear Stability Theory Results

Spatial LST is employed to capture the unsteady modes in this hypersonic flow, where $L^* = 0.001$ m serves as the reference length. Figure 5-4 illustrates the spatial growth rate contours at $s^* = 40$ mm for the $\Lambda = 0°$ case in the Cartesian coordinate, the $\Lambda = 45°$ case in the Cartesian coordinate, the $\Lambda = 45°$ case in the streamline-aligned coordinate, and the $\Lambda = 45°$ case in the streamline-aligned coordinate with u_c deliberately set to 0. The contour line at $-\alpha_i = 0.025$ is plotted to facilitate identifying different instability regions. Positions at $\beta = 0$ are marked as dashed lines to enable observing the symmetry of instabilities.

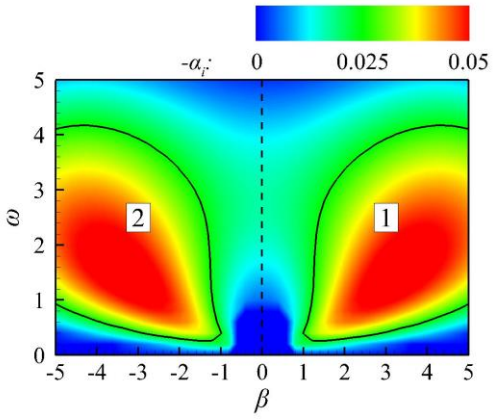

(a) $\Lambda = 0°$ case in the Cartesian coordinate

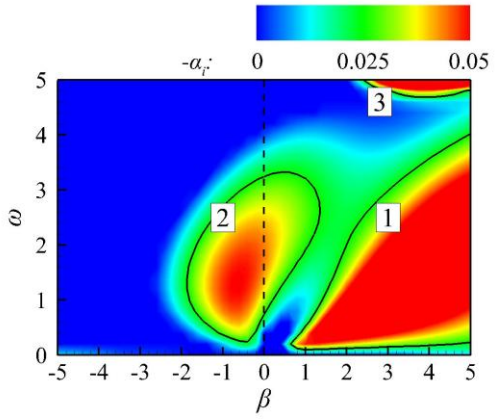

(b) $\Lambda = 45°$ case in the Cartesian coordinate

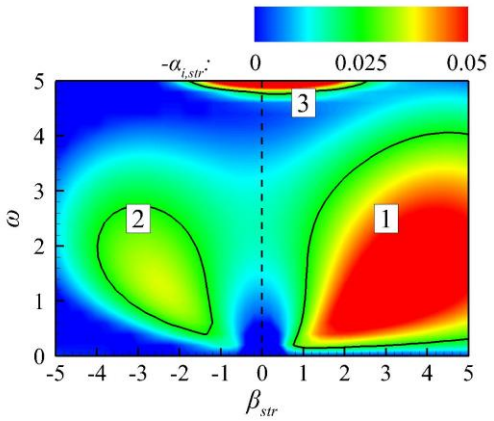

(a) $\Lambda = 45°$ case in the streamline-aligned coordinate

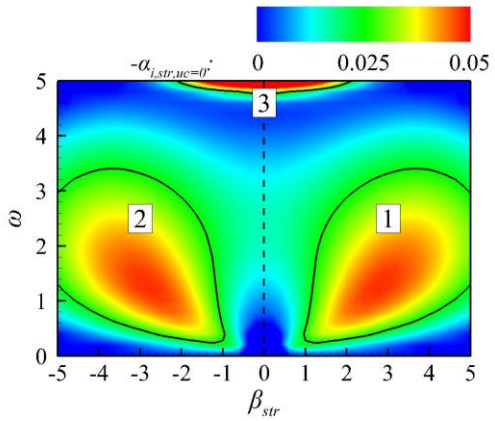

(b) $\Lambda = 45°$ case in the streamline-aligned coordinate with u_c deliberately set to 0

Figure 5-4 Growth rate contours at $s^* = 40$ mm.

The instability mechanism is first discussed within the Cartesian coordinate, where velocity components u and w are employed. Since the DNS is applied in Cartesian coordinates, this LST approach enables direct comparisons in subsequent analyses. For $\Lambda = 0°$, two instability regions, which are symmetric to $\beta = 0$, span extensive ranges of β values within the lower frequency domain. These instability regions correspond to the first Mack mode, as expected for 2D configurations. At $\Lambda = 45°$ in the Cartesian coordinate, three distinct instability regions are identified: Region 1 spans a wide range of β and connects to zero-frequency branches, typifying the emergence of crossflow instability in the traditional terminology. Region 2, a modified mode, is confined to a narrow β region. This instability originates from the coalescence of the negative spanwise wavenumber of the first mode under the asymmetric effect of the 3D baseflow, consistent with observations in Refs. [10] and [31]. The asymmetry between regions 1 and 2 also highlights the emergence of crossflow instability. Region 3, typifying the oblique second Mack mode, occupies the high-frequency domain. Under the current flow condition, second Mack modes can exhibit higher growth rates, whereas this study focuses on lower-frequency first Mack and crossflow instabilities. Therefore, the disturbance frequency and spanwise wavelength are set to guarantee the evolution of a highly amplified crossflow instability, where $F^* = 80$ kHz, $\lambda_z^* = 4$ mm ($\omega = 0.485$, $\beta = 1.571$).

LST results in the streamline-aligned coordinate are then analyzed to clarify the mechanisms of each instability region. For the $\Lambda = 45°$ case in the streamline-aligned coordinate, regions 1 and 2 remain asymmetric. Region 3 still characterizes the second Mack mode, with its maximum growth rate shifted away from $\beta = 0$. In Figure 4(d), the crossflow velocity is artificially set to 0, thereby illustrating the instability originating from the streamwise velocity. Compared to the $\Lambda = 0°$ case, the first mode becomes less significant and the second Mack mode shifts to lower-frequency regions. Crossflow components universally destabilize the positive-β branch, while stabilizing the negative-β branch, confirming that crossflow components act as a modulating mechanism rather than constituting a distinct instability mode

As discussed before, favorable pressure gradients suppress first Mack modes[49,50], while amplifying crossflow modes[51]. A comparative analysis employs a decreased airfoil thickness of 0.5 mm. Pressure gradients and spatial growth rates from LST at $s^* = 40$ mm for both thickness configurations are summarized in Figure 5-5. As depicted, thinner profiles substantially decrease favorable pressure gradients across all sweep angles. At $\Lambda = 0°$ and 15°, the spatial growth rate diminishes with strengthened pressure gradients. For $\Lambda = 30°$ and 45°, the instability is amplified under an enhanced favorable

pressure gradient, confirming the predominance of the crossflow instability. Based on the instability's response to pressure gradients, the dominant mechanism is the first Mack mode when $\Lambda = 0°$ and 15°, whereas the crossflow instability for the $\Lambda = 30°$ and 45° cases.

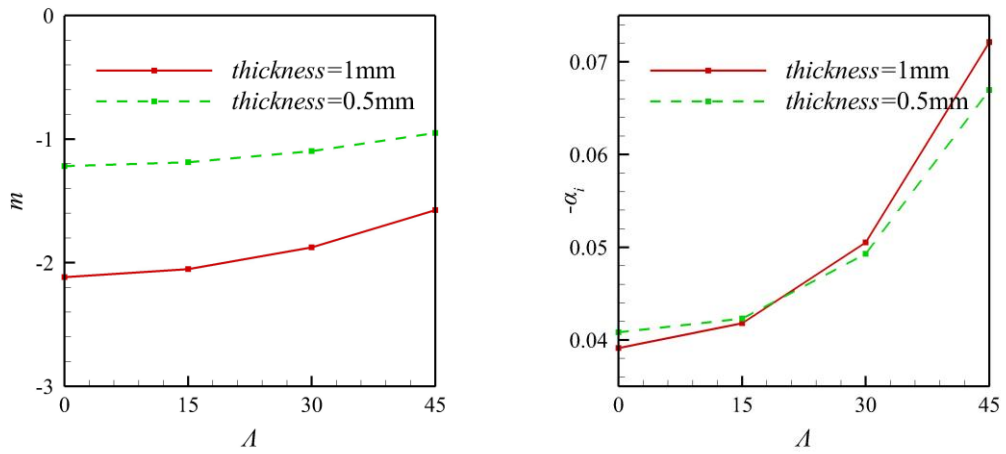

(a) Pressure gradients (b) spatial growth rates at $s^* = 40$ mm

Figure 5-5 Pressure gradients and spatial growth rates under different thicknesses.

Although disturbances at distinct Λ exhibit differential responses to pressure gradients, both oblique first modes and crossflow modes belong to S modes based on LST. Figure 5-6 presents eigenspectra at $s^* = 2$, 4, 6, 8, 10, 15, 20, 25, 30, 35, and 40 mm for both $\Lambda = 0°$ and $\Lambda = 45°$ cases. Solid black trajectories track the evolution of the S modes from stable to unstable states with increasing s^*, while green circles highlight persistently neutral F modes. This consistent behavior in both cases indicates a fundamental connection between these instabilities. Table 5-2 documents neutral point locations where the first Mack or crossflow modes' growth rates transition to positive values. The neutral point shifts upstream with increasing sweep angles.

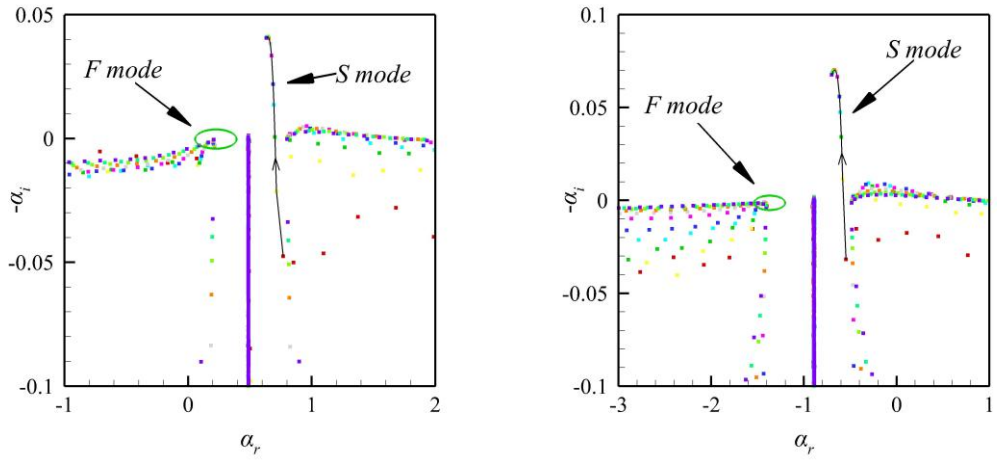

(a) Λ = 0° case (b) Λ = 45° case

Figure 5-6 The evolution of F and S modes.

Table 5-2 Locations of neutral points at different sweep angles.

Λ	0°	15°	30°	45°
Location of the neutral point (mm)	6	5.6	4.6	3.4

5.3. Receptivity to Freestream Waves

This section investigates the boundary layer receptivity mechanisms to free-stream acoustic and vorticity perturbations at a frequency of F^* = 80 kHz and a spanwise wavelength of λ_z^* = 4 mm. As established in the prior analysis, the first Mack mode (at Λ = 0°) or the crossflow mode (at Λ = 45°) serves as the dominant instability under these parametric conditions. The wave field for the receptivity simulation is expressed as:

$$\boldsymbol{Q}'(x,y,z,t) = \boldsymbol{Q}(x,y,z,t) - \bar{\boldsymbol{Q}}(x,y,z) \tag{5.2}$$

where $\boldsymbol{Q}'(x,y,z,t)$ is the perturbation of a flow variable, $\boldsymbol{Q}(x, y, z, t)$ represents the instantaneous value from unsteady DNS, and $\bar{\boldsymbol{Q}}(x,y,z)$ corresponds to the time-averaged values from steady DNS. The computational framework assumes spanwise-periodic conditions for swept-wing geometries, with free-stream disturbance wave propagation occurring exclusively in the x-z plane. For small-amplitude free-stream perturbations, the perturbations of an arbitrary flow variable can be described in the following form:

$$\begin{bmatrix} u' \\ w' \\ p' \\ \rho' \end{bmatrix}_\infty = \begin{bmatrix} \delta u \\ \delta w \\ \delta p \\ \delta \rho \end{bmatrix}_\infty \exp\left(i\left[\alpha_{r,\infty} x + \beta z - \omega t\right]\right) \tag{5.3}$$

where δu, δw, δp, and $\delta \rho$ represent dimensionless amplitudes of the free-stream perturbations in the Cartesian coordinate. The dispersion relations and perturbation magnitudes for the slow acoustic waves and vorticity waves are represented as follows (align with the definition in Ref. [59], the usage of different axis directions causes differences on the sign):

slow acoustic waves (*AC*): $\omega = k_\infty \left(-\frac{1}{M_\infty} + \cos\theta_\infty \right)$

$$\begin{aligned} &\delta u = -A_p \frac{M_\infty \alpha_{r,\infty}}{k_\infty}, \quad \delta w = -A_p \frac{M_\infty \beta}{k_\infty}, \\ &\delta p = A_p, \qquad\qquad \delta \rho = A_p M_\infty^2 \end{aligned} \tag{5.4}$$

vorticity waves (*VO*): $\omega = k_\infty \cos\theta_\infty$

$$\begin{aligned} &\delta u = A_p \frac{\beta}{k_\infty}, \quad \delta w = -A_p \frac{\alpha_{r,\infty}}{k_\infty}, \\ &\delta p = 0, \qquad\qquad \delta \rho = 0 \end{aligned} \tag{5.5}$$

where *AC* denotes slow acoustic waves, *VO* represents vorticity waves. Hereinafter, the case nomenclature combining disturbance type and sweep angle, *AC*-0°, as an example, corresponds to the slow acoustic wave case under Λ = 0°. A_p is the dimensionless magnitude of free-stream waves, set to 10^{-6} in this study. The relationships between the free-stream wavenumber vector k_∞, the incident wave angle θ_∞ (see Figure 5-1), $\alpha_{r,\infty}$ and β are:

$$k_\infty = \sqrt{\alpha_{r,\infty}^2 + \beta^2} \quad \tan(\theta_\infty + \Lambda) = \beta / \alpha_{r,\infty} \tag{5.6}$$

The current research employs perturbations with identical frequencies (ω) and spanwise wavenumbers (β) to enable systematic comparison, where ω and β have been derived from LST. The undetermined quantities, i.e., $\alpha_{r,\infty}$, k_∞, and θ_∞, are resolved by combining equation (5.6) with either equation (5.4) or (5.5). Table 5-3 catalogs computed $\alpha_{r,\infty}$ values across all configurations, where negative values indicate that trace velocities of the waves propagate opposite to the chordwise direction. Note that linear growth phases occur upstream of x^* = 40 mm in all cases. Unlike the second Mack

mode, neither the first Mack nor crossflow instabilities exhibit a synchronization point between F and S modes, and no new flow structures emerge after linear growth onsets. Receptivity calculations are hereby restricted to the front airfoil regions ($x^* \leq 40$ mm) to reduce calculation cost. After obtaining the perturbation field with DNS, MPT is applied on the perturbation fields for a physics-based interpretation of the receptivity process.

Table 5-3 The spatial wavenumbers $\alpha_{r,\infty}$ of freestream disturbances.

Λ	0°	15°	30°	45°
AC	0.783	0.364	−0.039	−0.490
VO	0.485	0.081	−0.347	−0.885

5.3.1. Receptivity to slow acoustic waves

The spatial evolution of perturbation fields is systematically examined through density ρ' and velocity u' distributions shown in Figure 5-7 and Figure 5-8. Figure 5-7 displays slices taken at $z^* = 0$ mm, streamwise stations $s^* = 1$, 10, 20, 30, 40 mm, and the wall, while Figure 5-8 details instantaneous snapshots of u' at $z^* = 0$ mm and $s^* = 30$ mm. Shock waves and boundary layer edges are marked by white solid lines and dashed lines in Figure 5-8. Following Balakumar's analytical framework[7], the whole perturbation field comprises four distinct regions: the freestream disturbance region, the shock layer, the area between the shock and boundary layer, and the boundary layer.

The first region, located outside the shock, is characterized by uniformly propagating acoustic waves, as shown in Figure 5-7. For slow acoustic waves, the magnitude of ρ' is at the same level as that of the boundary layer disturbance, while u' is relatively small compared to the boundary layer values and consequently absent in Figure 5-8. This originates from the magnitude relationship in equation (5.4). The second region encompasses the shock layer, where interactions between shock waves and slow acoustic waves result in localized amplifications of ρ'. However, u' disturbances remain too weak to be visible in Figure 5-8. The third region between the shock and the boundary layer comprises transmitted external acoustic fields and disturbances radiating from the boundary layer. These transmitted waves soon dissipate, whereas the radiating disturbances exhibit continuous amplifications as propagating downstream. Interestingly, Figure 5-7(c) reveals exclusively positive ρ' values across these three regions at $z^* = 0$ mm. This is attributed to the small $\alpha_{r,\infty}$ value (as shown

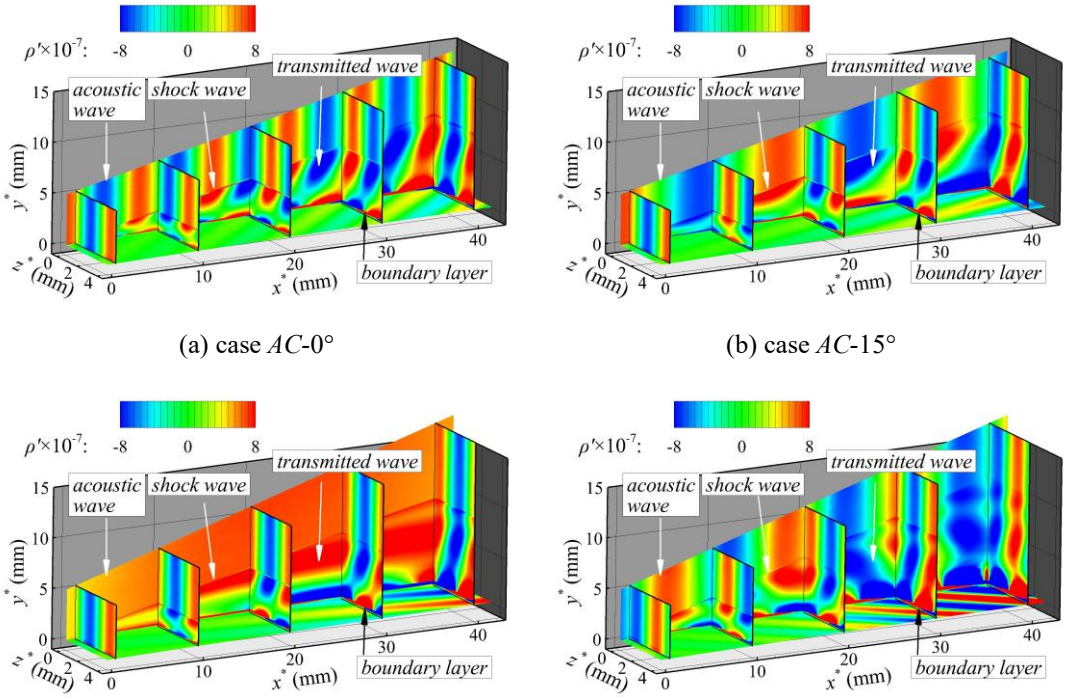

(a) case *AC*-0°

(b) case *AC*-15°

(c) case *AC*-30°

(d) case *AC*-45°

Figure 5-7 The density fluctuation contours.

in Table 5-3), yielding elongated streamwise wavelengths for free-stream disturbances. Free-stream disturbances still propagate uniformly in this case, which can be observed in the spanwise direction from the streamwise slices, for example, $s^* = 30$ mm. The behaviors of acoustic waves and transmitted waves in these three regions quite align with 2D receptivity simulations in Ref. [7] for acoustic waves, while diverging behaviors in the boundary layer arise due to distinct instability modes. Disturbances evolve and manifest as single-cell structures in the ρ' and u' fields in the boundary layers. In all scenarios, the boundary-layer disturbances start from the leading edge and rapidly surpass free-stream amplitudes. The disturbances within the boundary layer are critical to the transition process, therefore, they will be examined in detail through the analysis of wall density fluctuations.

The amplitudes and wavenumbers of wall density disturbances from DNS are presented in Figure 5-9, compared against the N factors and wavenumbers of S modes from LST. The time series of fluctuating pressure at the wall is processed by Fourier transformation to obtain phase angle φ'. The local wavenumber α_r of wall density disturbances is subsequently calculated by[75]:

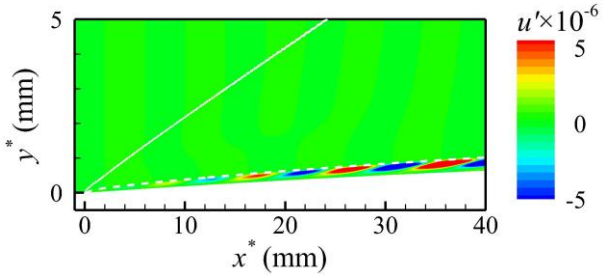

(a) $z^* = 0$ in case *AC*-0°

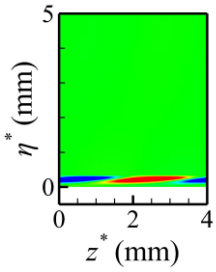

(b) $s^* = 30$ mm in case *AC*-0°

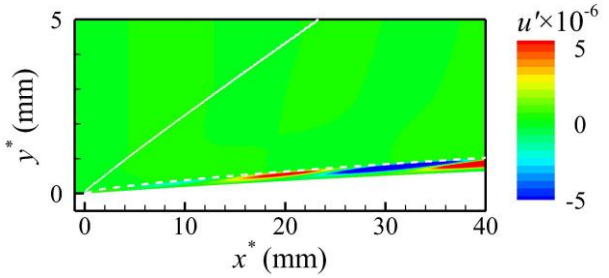

(c) $z^* = 0$ in case *AC*-15°

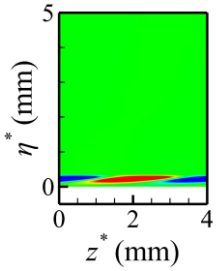

(d) $s^* = 30$ mm in case *AC*-15°

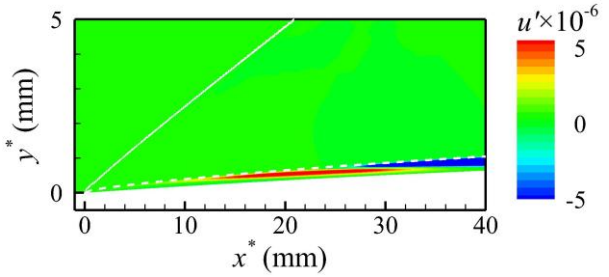

(e) $z^* = 0$ in case *AC*-30°

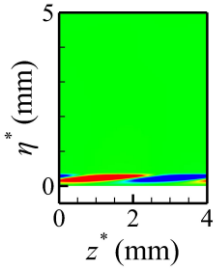

(f) $s^* = 30$ mm in case *AC*-30°

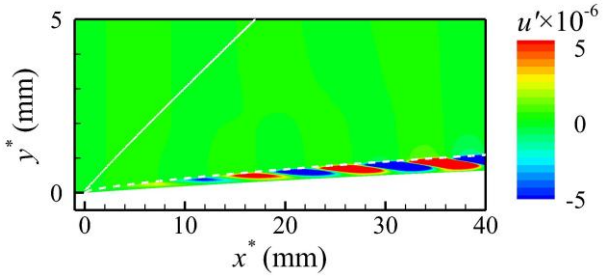

(g) $z^* = 0$ in case *AC*-45°

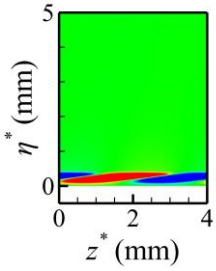

(h) $s^* = 30$ mm in case *AC*-45°

Figure 5-8 The streamwise velocity fluctuation contours.

$$\alpha_r = L^* \frac{d\varphi'}{dx} \tag{5.7}$$

The N factor from the LST is calculated by[122]:

$$N = \int_{x_{neutral}}^{x} -\alpha_i dx \tag{5.8}$$

where $x_{neutral}$ is the neutral point location. The formation of first and crossflow modes goes through a non-modal stage. The beginning of linear growth is set to where the disparity in both amplitudes and wavenumbers between DNS and LST is less than 5% (for oscillating α_r from DNS, α_r should be closely around LST values). The beginning of linear growth is marked by dark gray lines in Figure 5-9.

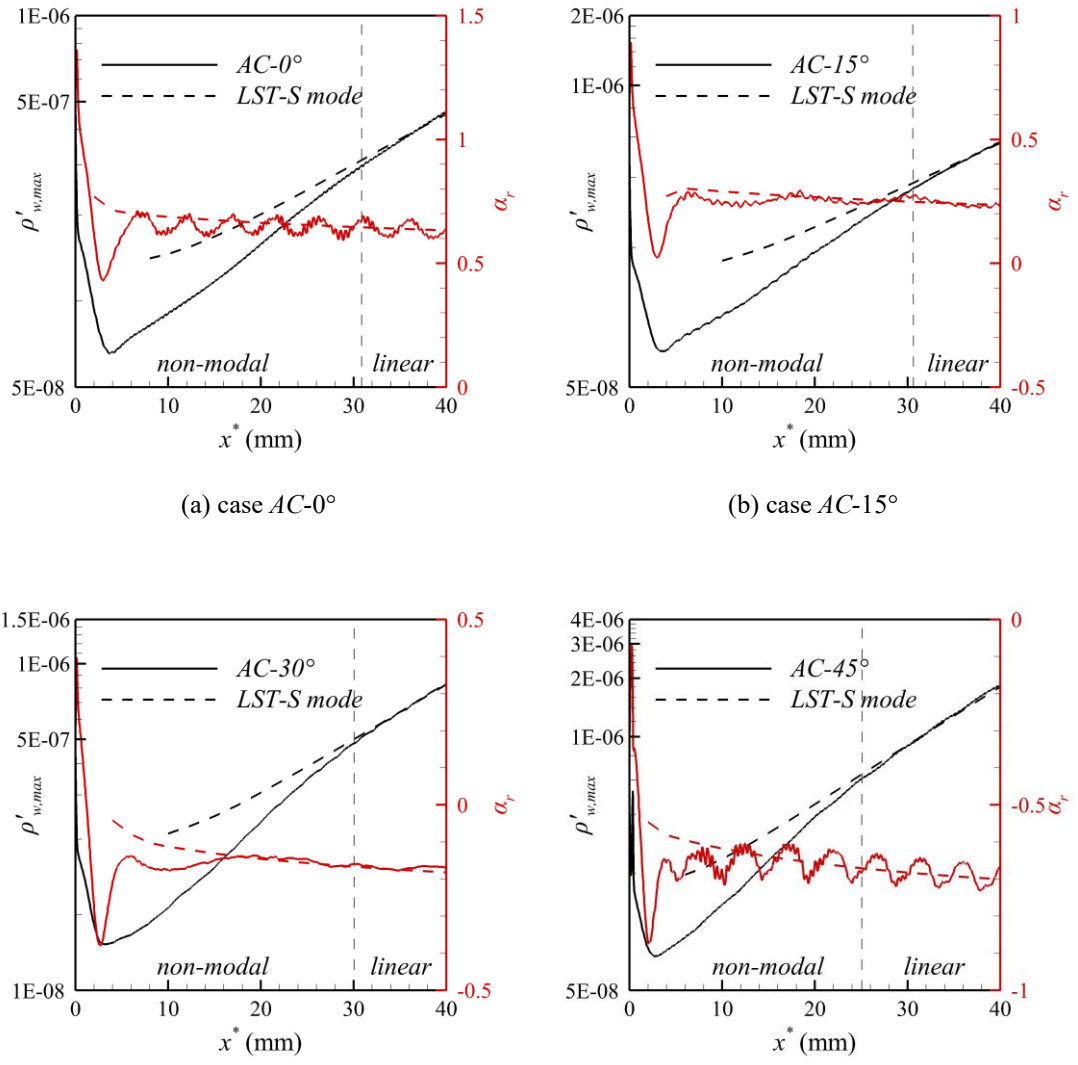

(a) case *AC*-0°

(b) case *AC*-15°

(c) case *AC*-30°

(d) case *AC*-45°

Figure 5-9 The wall density fluctuation amplitudes and streamwise wavenumbers.

The results indicate first Mack and crossflow modes undergo a uniform receptivity pathway. At leading edges, the interactions between acoustic waves, shock waves, and boundary layers induce sudden amplitude enlargement followed by rapid damping, accompanied by abrupt shift. After the local minimum of $\rho'_{w,\max}$, perturbation growth rates surpass LST predictions, along with the wavenumbers gradually converge toward S-mode values. During this rapid growing region, wavenumbers approach S-mode values sooner than the amplitudes, implying the perturbations possess some key natures of the S mode before the onset of linear growth. This is corroborated by u'-profiles at the neutral point (as depicted in Figure 5-10), where cases *AC*-0° and *AC*-45° exhibit strong agreement with LST eigenfunctions prior to linear growth phases. After this rapid growth stage, both spatial growth rates and wavenumbers of perturbations align with LST solutions, indicating linear growths of first Mack or crossflow instabilities occur. Two fundamental questions arise from these observations: Why does rapid damping occur at the leading edge despite the synchronization between S modes and slow acoustic waves? How does non-modal growth persist when perturbation profiles already approximate S-mode eigenfunctions? The underlying mechanisms of this receptivity pathway are then discussed with MPT.

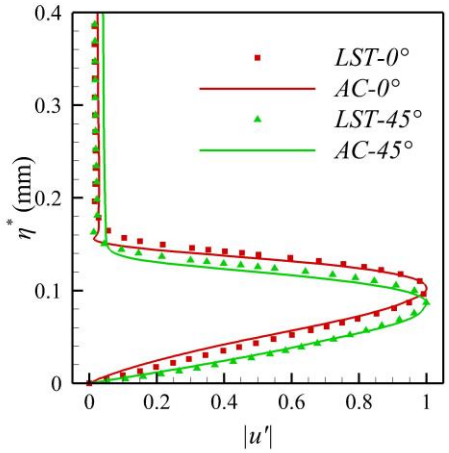

Figure 5-10 The u' profiles for *AC*-0° and *AC*-45° cases at neutral points.

Instantaneous snapshots of MPT components in cases *AC*-0° and *AC*-45° are illustrated in Figure 5-11. Shock waves and boundary layer edges are marked by white solid lines and dashed lines, whereas the vertical black dashed line refers to the beginning of linear growth stage. MPT components exhibit distinct behaviors in different regions: In the freestream disturbance region, the acoustic component $\boldsymbol{m}'_A$

propagates uniformly, whereas m'_B and m'_T remain negligible in the free stream. At the shock layer, m'_A experiences localized distortion, accompanied by weak m'_B generation due to baroclinity, while m'_T persists at negligible levels. Su and Geng[123] demonstrate that transmitted waves, generated by the interaction between freestream waves and shock waves, also play a role in the receptivity process. Freestream disturbance waves have intrinsic physical connection with MPT components: acoustic waves correspond to acoustic components, vorticity waves to vortical components, and entropy waves to thermal components. This relationship allows for a preliminary analysis of the transmitted waves behind the shock. From Figure 5-11, the post-shock region contains significant acoustic components and small vortical components, indicating that the transmitted waves are composed of acoustic and vortical waves.

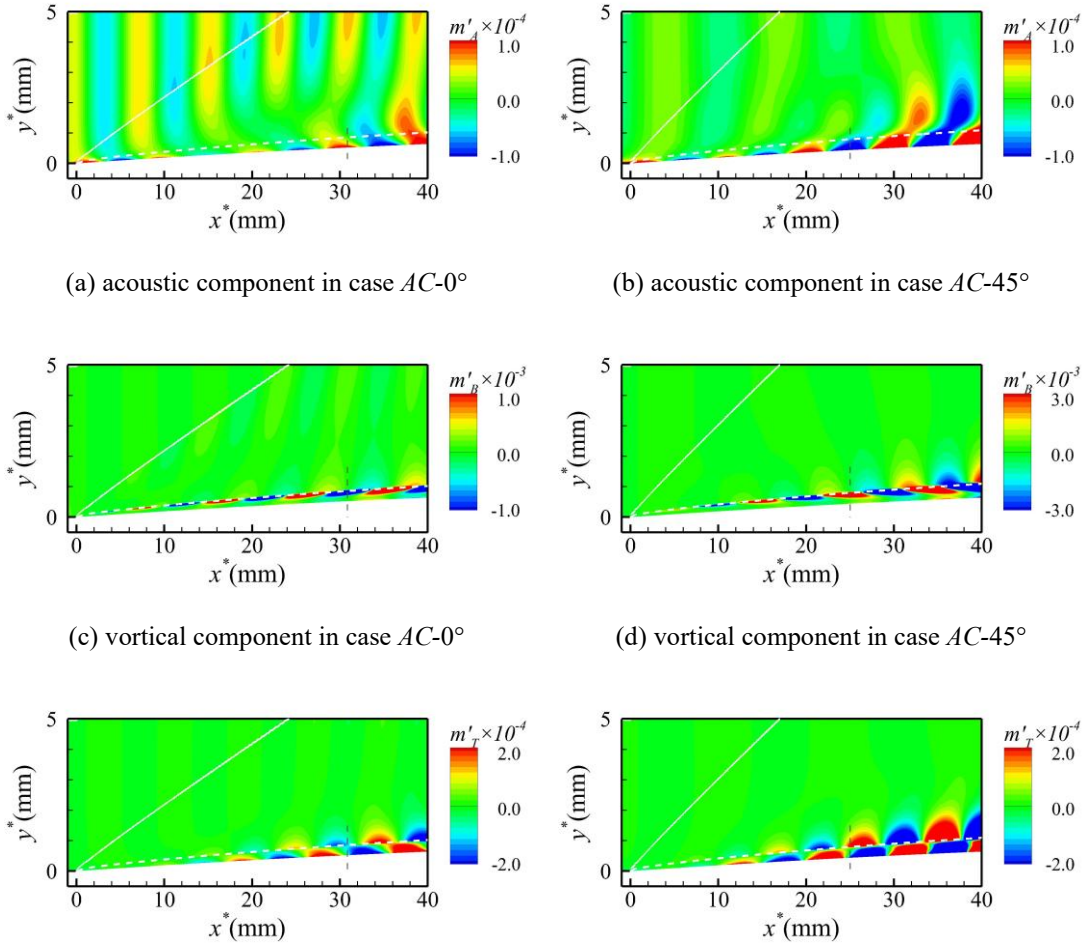

(a) acoustic component in case *AC*-0°

(b) acoustic component in case *AC*-45°

(c) vortical component in case *AC*-0°

(d) vortical component in case *AC*-45°

(e) thermal component in case *AC*-0°

(f) thermal component in case *AC*-45°

Figure 5-11 The instantaneous snapshots of MPT components.

Figure 5-12 depicts the amplitudes of MPT components at s^* = 1, 20, 40 mm, aiming to capture the leading edge, non-modal growth, and linear growth behaviors. Each amplitude is normalized by the maximum fluctuation momentum density $\boldsymbol{m}'$ in boundary layers. During the linear growth stage (the s^* = 40 mm profile), $\boldsymbol{m}'_B$ is the dominant component, exceeding both $\boldsymbol{m}'_A$ and $\boldsymbol{m}'_T$ in magnitudes, which reflects the vortical nature of the oblique first mode and crossflow mode.

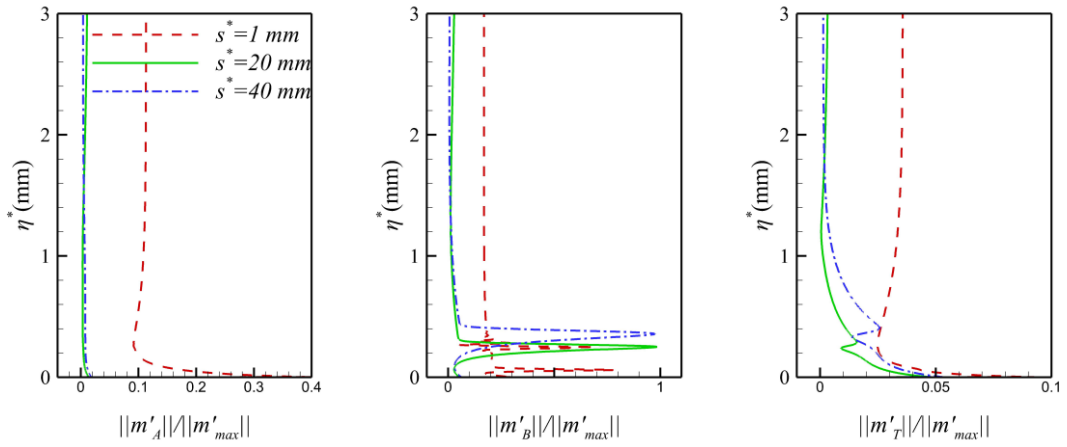

(a) acoustic component in case *AC*-0° (b) vortical component in case *AC*-0° (c) thermal component in case *AC*-0°

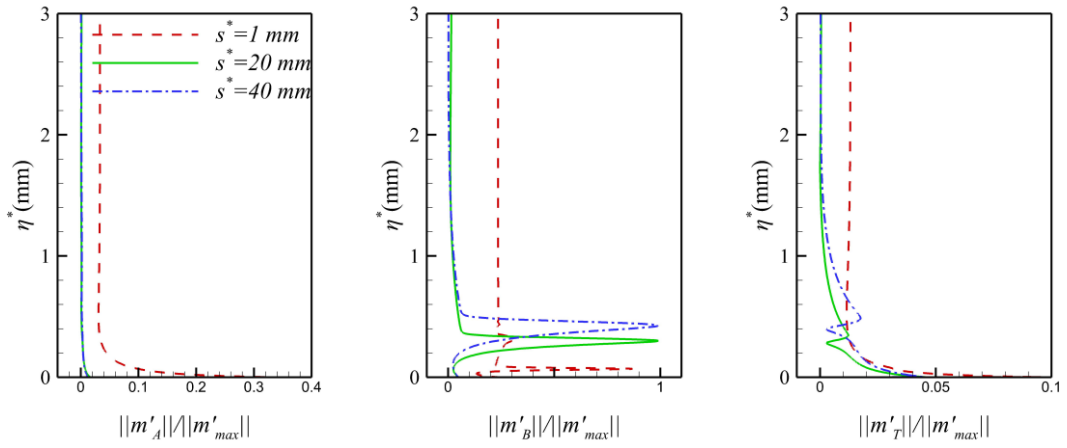

(d) acoustic component in case *AC*-45° (e) vortical component in case *AC*-45° (f) thermal component in case *AC*-45°

Figure 5-12 The normalized amplitudes of MPT components.

For the disturbance evolution in boundary layer regions, the origin of non-modal stages is explained by MPT component dynamics. At the leading-edge, significant $\boldsymbol{m}'_A$ is generated through the synchronization mechanism[64]. $\boldsymbol{m}'$ rapidly decays as this

large acoustic component can not persist in boundary layers. Concurrently, $\boldsymbol{m}'_{\boldsymbol{B}}$ makes up a smaller proportion than the linear stage, while $\boldsymbol{m}'_{\boldsymbol{T}}$ constitutes a large fraction. The high amplitude and fast dissipation at the leading edge observed in Figure 5-9 correspond to the damping of acoustic perturbations. During the rapid non-modal growth stage, $\boldsymbol{m}'_{\boldsymbol{A}}$ dissipating to a small proportion, with $\boldsymbol{m}'_{\boldsymbol{T}}$ reduces to a lower level than the linear growth. In Figure 5-11(c, d) and Figure 5-12(b, e), $\boldsymbol{m}'_{\boldsymbol{B}}$ exhibits continuous growth in magnitudes from $s^* = 1$ to 20 mm. The predominance of $\boldsymbol{m}'_{\boldsymbol{B}}$ near the neutral point results in the good agreement between perturbation profiles and LST eigenfunctions in Figure 5-10, since the vortical component is the primary contributor to first Mack and crossflow modes. In this stage, the adjustment of $\boldsymbol{m}'_{\boldsymbol{A}}$ and $\boldsymbol{m}'_{\boldsymbol{T}}$ drive $\rho'_{w,\max}$ and α_r toward convergence with LST results, whereas the high growth rate is credited to the growth of $\boldsymbol{m}'_{\boldsymbol{B}}$. Further downstream, all MPT components enter a steady growth phase, signaling the free-stream acoustic waves successfully excite the oblique first mode or crossflow mode, thereby completing the receptivity process.

Both cases *AC*-0° and *AC*-45° share the same receptivity mechanisms, with their divergence manifesting in amplitudes of MPT components. The underlying mechanisms of the receptivity pathway can be summarized as: $\boldsymbol{m}'_{\boldsymbol{A}}$ initially penetrates the boundary layer at high proportions, subsequently undergoing damping and recovery. $\boldsymbol{m}'_{\boldsymbol{B}}$ exhibits continuous growth throughout the receptivity process. $\boldsymbol{m}'_{\boldsymbol{T}}$ goes through a similar pathway with $\boldsymbol{m}'_{\boldsymbol{A}}$ but with lower initial proportions among the three components.

The receptivity coefficient refers to the efficiency of disturbance waves in generating instability waves, thus is a crucial factor in engineering. According to Balakumar's definition[41], the receptivity coefficient to slow acoustic waves is defined at the neutral point, formed as:

$$C_{AC} = \left(u'_{\max} / \left| p' \right|_{AC}\right)_{\text{neutral}} \tag{5.9}$$

As neutral points lie in non-modal regions and after the minimum of $\rho'_{w,\max}$, where dynamics are governed by the behavior of increasing $\boldsymbol{m}'_{\boldsymbol{B}}$, this metric effectively quantifies the efficiency of acoustic waves in exciting vortical components, offering practical insight for engineering applications. The receptivity coefficients to slow acoustic waves for various sweep angles are summarized by the red line in Figure 5-13. C_{AC} demonstrates a consistent decrease as the sweep angle increases. The absence of abrupt discontinuities in C_{AC} when the sweep angle increases further highlights that these two instabilities are of the same nature.

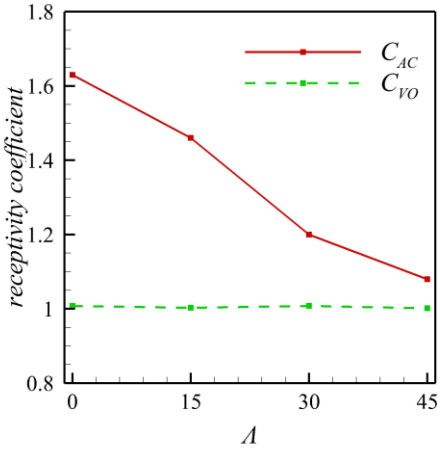

Figure 5-13 The receptivity coefficients of all cases.

5.3.2. Receptivity to vorticity waves

Consistent with equation (5.5), vorticity waves are introduced into the flow field. Figure 5-14 illustrates the spatial distributions of u' across all cases with vorticity disturbances. White solid lines are plotted in the $z^* = 0$ mm slice to mark the shock wave positions. Instantaneous snapshots of ρ' at $z^* = 0$ mm and $s^* = 30$ mm are presented in Figure 5-15. Shock waves and boundary layer edges are marked by white solid lines and dashed lines. Given the unique receptivity behavior associated with vorticity waves, perturbation fields near leading edges are presented in zoomed-in views to facilitate observation. The flow field is also divided into four regions: the freestream disturbance region, the shock layer, the area between the shock and boundary layer, and the boundary layer.

In the freestream disturbance regions, only velocity disturbances (u') are observed, while ρ' remain absent, consistent with the governing relation defined in equation (5.5). Shock layers generate density disturbances at a comparable order of magnitude to those in the boundary layer, while changes in u' are small. Impacts of weak leading-edge shock waves on vorticity disturbances are less significant than that on slow acoustic waves. The transmitted waves closely resemble vorticity waves and connect to boundary layers, which complicate the identification of unstable modes with u' in boundary layers. A practical method for identifying unstable modes is to observe ρ' in Figure 5-15. Disturbances with short spatial wavelengths are generated through the interaction between shock waves, vorticity waves, and boundary layers at the leading edge. These disturbances dissipate quickly, forming “dead zones”, which are characterized as the relatively low magnitudes of perturbations. Downstream of these

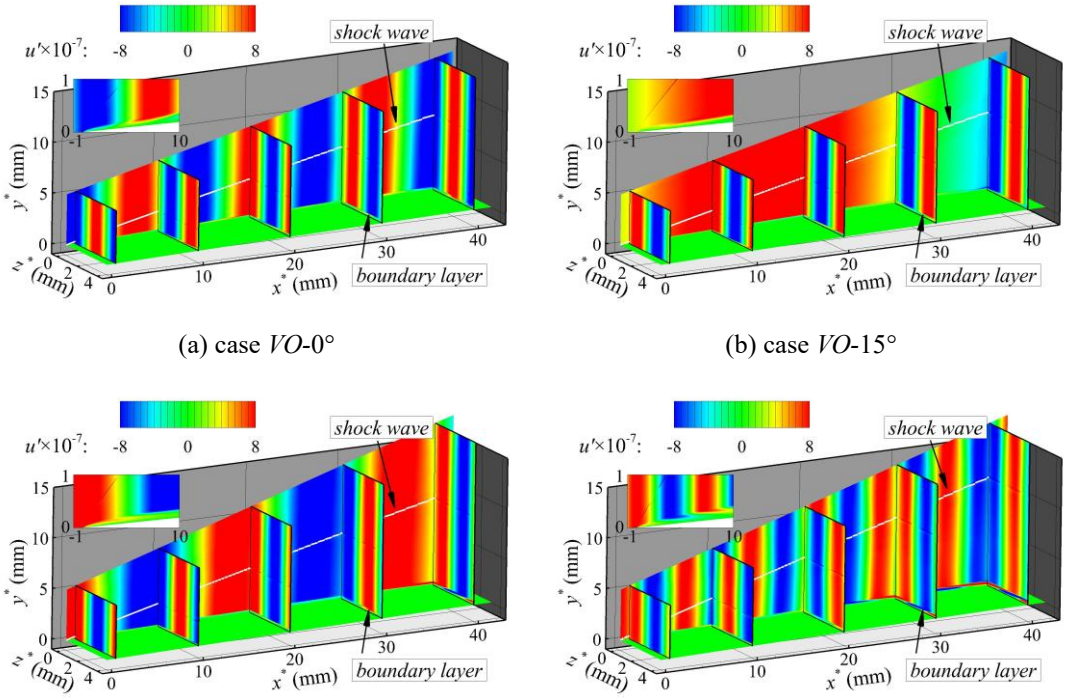

(a) case *VO*-0° (b) case *VO*-15°

(c) case *VO*-30° (d) case *VO*-45°

Figure 5-14 The streamwise velocity fluctuation contours.

"dead zones", first and crossflow modes are established. Within a considerable distance (until approximately $s^* = 30$ mm), u' amplitudes within boundary layers remain smaller than the free-stream perturbation levels (see Figure 5-14).

Figure 5-16 summarizes the amplitudes and spatial wavenumbers of wall density disturbances from DNS, along with N factors and α_r of S modes from LST. The beginning of linear growth is marked by vertical black lines. In all cases, $\rho'_{w,\max}$ peaks form at the leading edge but soon undergo rapid attenuation (start at approximately $x^* = 2$ mm), accompanied by steep reductions in α_r. These leading-edge declines persist over longer streamwise distances compared to *AC* cases. The "dead zones" emerge as a direct consequence of this prolonged attenuation phase. Previous studies suggest that F modes are easily excited by vorticity waves[7,59]. However, the leading-edge wavenumbers are incompatible with F modes, indicating this mechanism does not occur under current flow configurations, where F modes remain neutral throughout the boundary layer (depicted in Figure 5-6). The decline of $\rho'_{w,\max}$ and α_r after the leading-edge peak ($x^* = 2$ to 10 mm) is similar to the leading-edge decline observed in acoustic wave cases (Figure 5-9, $x^* = 0$ to 4 mm). This parallel demonstrates that the dissipation may act as the governing mechanism in this region, while the mechanism of forming $\rho'_{w,\max}$ peaks remains unresolved, requiring further analysis with MPT.

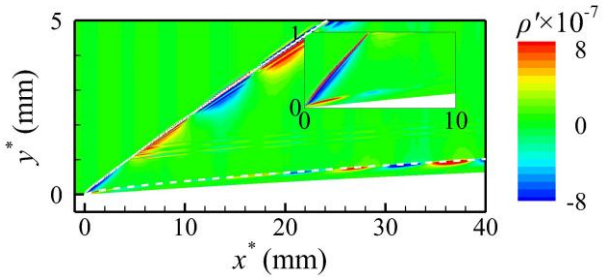

(a) z^* = 0 in case *VO*-0°

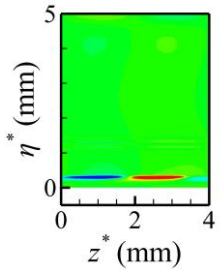

(b) s^* = 30 mm in case *VO*-0°

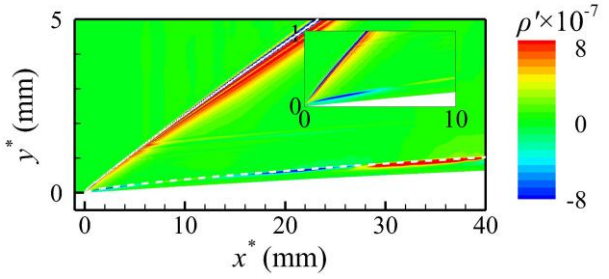

(c) z^* = 0 in case *VO*-15°

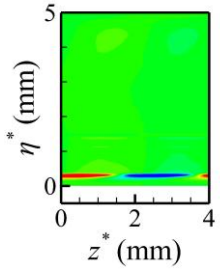

(d) s^* = 30 mm in case *VO*-15°

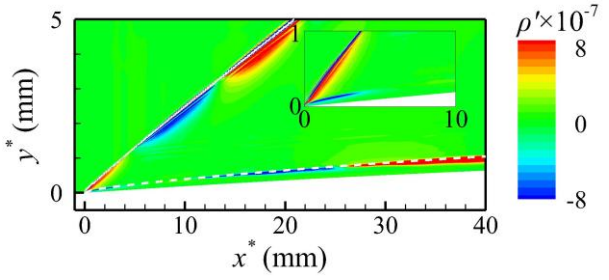

(e) z^* = 0 in case *VO*-30°

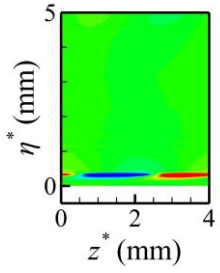

(f) s^* = 30 mm in case *VO*-30°

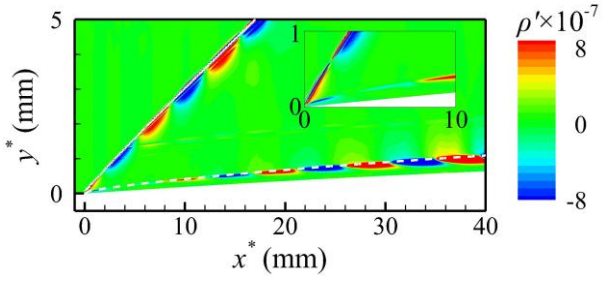

(g) z^* = 0 in case *VO*-45°

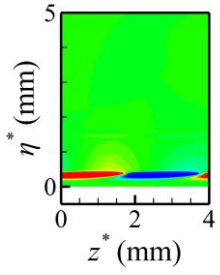

(h) s^* = 30 mm in case *VO*-45°

Figure 5-15 The density fluctuation contours.

Following this dissipating region, $\rho'_{w,\max}$ exhibit plateaus (nearly vanish in case *VO*-45°) and subsequently lower growth rates compared to S modes. During this regime, α_r remain marginally dispart from LST predictions. Finally, linear growth occurs in region III, where both $\rho'_{w,\max}$ growth and α_r converge with LST predictions. Interestingly, the non-modal stage persists longer than that in case *AC*-0°, while this trend reverses in cases 45°, implying a stronger receptivity of crossflow instabilities to vorticity waves.

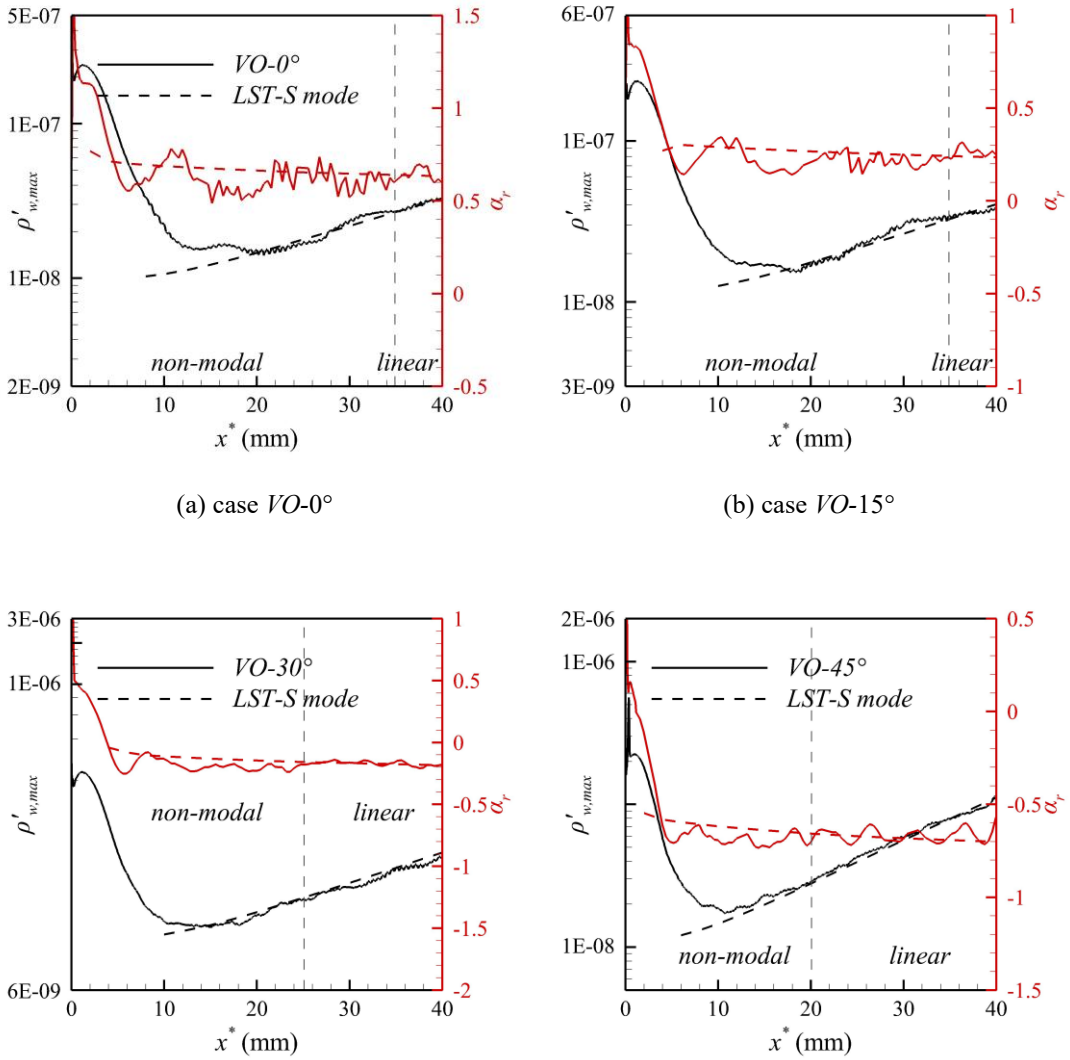

(a) case *VO*-0° (b) case *VO*-15°

(c) case *VO*-30° (d) case *VO*-45°

Figure 5-16 The wall density fluctuation amplitudes and streamwise wavenumbers.

Instantaneous snapshots of MPT components for the cases *VO*-0° and *VO*-45° are presented in Figure 5-17. Shock waves and boundary layer edges are marked by white solid lines and dashed lines, whereas the vertical black dashed line refers to the beginning of linear growth stage. As both the incoming perturbations and S modes are of vortical nature, the receptivity process in *VO* cases mainly involves the behaviors of $\boldsymbol{m}'_B$. Magnified views of $\boldsymbol{m}'_B$ near the leading edge are included to highlight its behavior. Upstream of shock waves, $\boldsymbol{m}'_B$ is uniformly transported by the free-stream vorticity waves, while $\boldsymbol{m}'_A$ are observed due to the contamination from the shock layer. At the shock layer, $\boldsymbol{m}'_A$ undergoes significant generation, alongside weaker $\boldsymbol{m}'_T$ generation, while $\boldsymbol{m}'_B$ is locally disturbed. Notably, within the shock layer, $\boldsymbol{m}'_A$ achieves higher amplitudes compared to its presence in the boundary layer, whereas $\boldsymbol{m}'_T$ is less prominent. The transmitted waves comprise a predominant vortical component, a small acoustic component, and the smallest thermal component, indicating that the post-shock transmitted waves remain primarily vorticity waves. At the boundary layer edge, Figure 5-17(c) and (d) reveal a distinctive phenomenon: the vorticity components are effectively blocked from the boundary layer. This observation aligns with the inference in Ref. [56] that the boundary layer effectively swallows vorticity waves. These results provide direct support that the primary source of boundary-layer modes originates from the interactions at the leading edge, with external vorticity waves contributing as a secondary mechanism, transferring limited energy at the boundary-layer edge.

Figure 5-18 depicts the amplitudes of MPT components at s^* = 1, 10, 40 mm, aiming to capture the leading edge, non-modal growth, and linear growth behaviors. Profile at s^* = 10 mm is selected because it is the location where the dissipating at leading edge ends and the plateau initiates. Each amplitude is normalized by the maximum fluctuation momentum density $\boldsymbol{m}'$ in boundary layers. Different from *AC* cases, the interactions between the vorticity wave, shock wave, and boundary layer produce strong vortical components, whereas acoustic and thermal components exhibit lower proportions of the total fluctuation momentum density $\boldsymbol{m}'$. This different behavior forms the $\rho'_{w,\max}$ peak in Figure 5-16 (compared to Figure 5-9 for *AC* cases). These components undergo adjustment. $\boldsymbol{m}'_A$ and $\boldsymbol{m}'_B$ exhibit a shape similar to that of linear regimes at s^* = 10 mm, except for comparatively large transmitted wave amplitudes (η^* > 0.4 mm), while $\boldsymbol{m}'_T$ undergoes attenuations and recoveries (see Figure 5-17). Subsequently, the linear growth phase commences, enabling boundary-layer modes to develop in a manner consistent with linear stability theory. The proportions of MPT components become highly similar with *AC* cases in Figure 5-12.

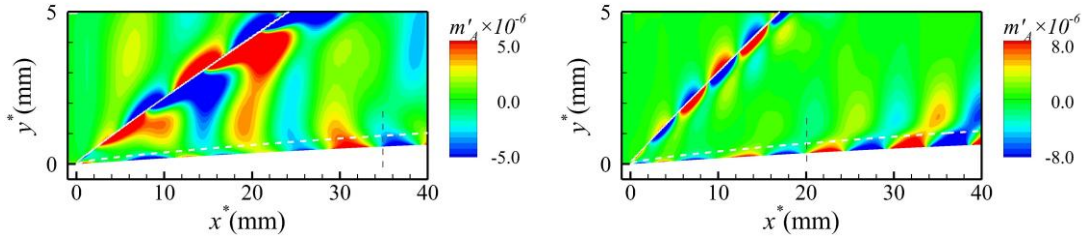

(a) acoustic component in case *VO*-0°　　(b) acoustic component in case *VO*-45°

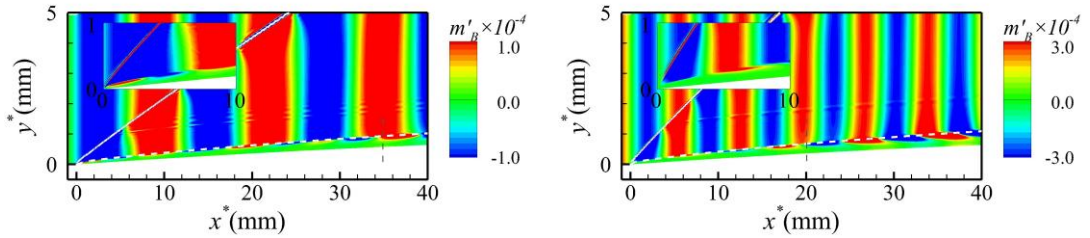

(c) vortical component in case *VO*-0°　　(d) vortical component in case *VO*-45°

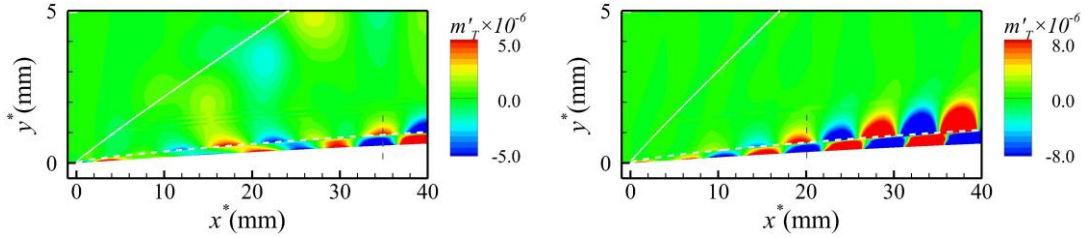

(e) thermal component in case *VO*-0°　　(f) thermal component in case *VO*-45°

Figure 5-17 The instantaneous snapshots of MPT components.

Cases *VO*-0° and *VO*-45° also share the same receptivity mechanisms, with their divergence manifesting in amplitudes of MPT components. The underlying mechanisms of the receptivity pathway can be summarized as: $\boldsymbol{m}'_B$ initially penetrates the boundary layer as a dominant component, then adjusts its eigenfunction to fit the linear growth. $\boldsymbol{m}'_A$ undergoes a similar pathway but initiates at a low proportion. $\boldsymbol{m}'_T$ attenuates initially but recovers downstream. These parallels highlight the first and crossflow modes are of the same nature.

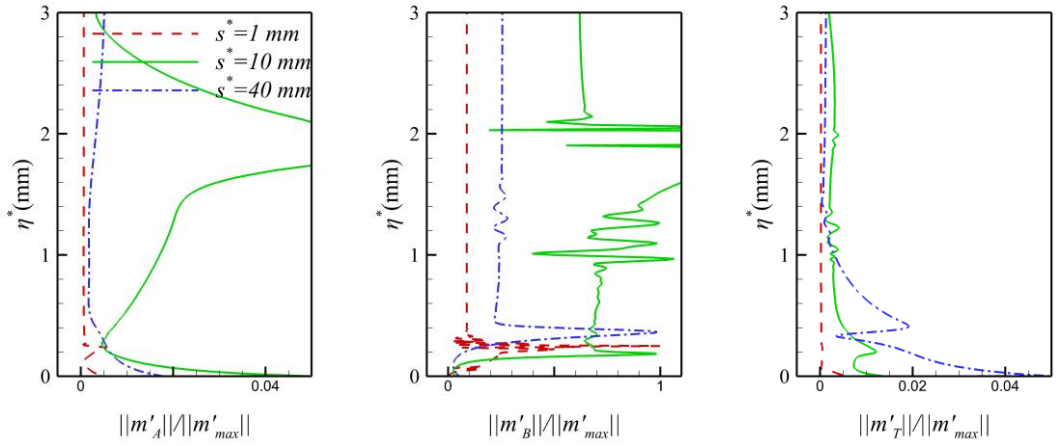

(a) acoustic component in case *VO*-0°

(b) vortical component in case *VO*-0°

(c) thermal component in case *VO*-0°

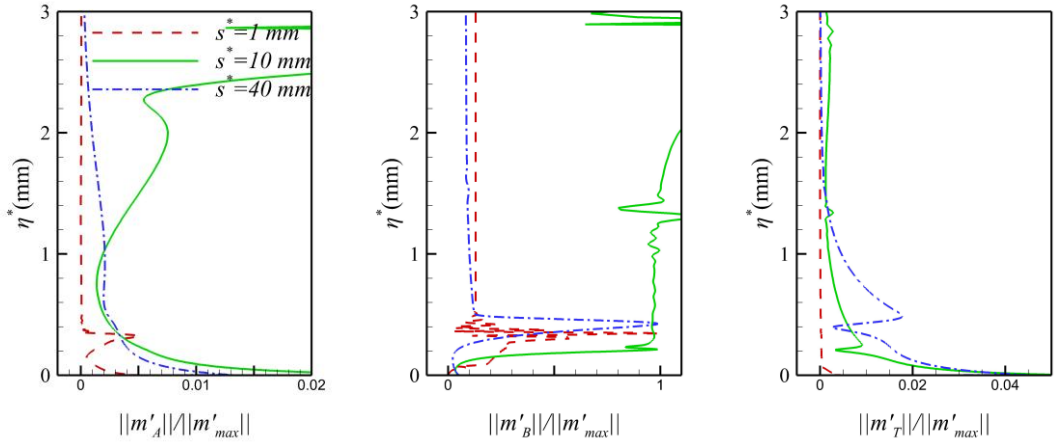

(d) acoustic component in case *VO*-45°

(e) vortical component in case *VO*-45°

(f) thermal component in case *VO*-45°

Figure 5-18 The normalized amplitudes of MPT components.

The receptivity coefficients are then calculated with the definition in Ref. [41]:

$$C_{VO} = \left(u'_{\max} / |u'|_{VO}\right)_{\text{neutral}} \tag{5.10}$$

These coefficients are summarized in Figure 5-13. All the receptivity coefficients are nearly 1 because the neutral points align with the dissipating phase of leading-edge disturbances. This situation renders them inadequate for effectively quantifying the genuine efficiency of vorticity waves in inducing unstable modes.

5.4. Summary

The receptivity of a spanwise-infinite wing to 3D slow acoustic waves and vorticity waves at various sweep angles has been comprehensively investigated. LST was utilized to provide a preliminary prediction of the properties of the relevant instabilities, offering a foundational understanding. DNS was then employed to obtain the detailed perturbation fields, capturing the precise dynamics of the receptivity processes. Furthermore, the MPT decomposition was employed to analyze these receptivity processes in detail, providing insight into the generation and evolution of boundary-layer instabilities.

For the baseflows, the sharp wing configuration with a constant curvature establishes a nearly constant favorable pressure gradient downstream of the leading edge. As the sweep angle increases, there is a noticeable rise in both the crossflow velocity and the boundary layer thickness. LST categorizes both the first Mack modes and crossflow instabilities as S modes. At the prescribed frequency and spanwise wavelength, S modes convert to an unstable state in the downstream region, whereas F modes remain neutral across the boundary layer. With increasing sweep angle, the location of the neutral point for the dominant modes shifts upstream. The dominant instability is the first mode at Λ = 0° and 15°, whereas the crossflow mode becomes dominant when Λ = 30° and 45°.

First and crossflow modes go through the same receptivity pathway to slow acoustic waves: A strong perturbation with large α_r is generated through the synchronization mechanism at the leading edge. Strong acoustic components $\boldsymbol{m}'_{\boldsymbol{A}}$ are produced through synchronization. Then a rapid damping of disturbance amplitudes and α_r happens as this strong acoustic component cannot persist in boundary layers. Then the non-modal growth exhibits a higher growth rate than that of the S mode, and α_r deviates slightly from the S mode. In this phase, high growth rates are governed by the continuous growth of the vortical components ($\boldsymbol{m}'_{\boldsymbol{B}}$), meanwhile adjustments of $\boldsymbol{m}'_{\boldsymbol{A}}$ and the thermal component ($\boldsymbol{m}'_{\boldsymbol{T}}$) drive the convergence of $\rho'_{w,\max}$ and α_r to LST predictions. The linear growth stage begins after the MPT components adjust and the results of DNS and LST match each other. At this final stage, $\boldsymbol{m}'_{\boldsymbol{B}}$ is the dominant component, exceeding both $\boldsymbol{m}'_{\boldsymbol{A}}$ and $\boldsymbol{m}'_{\boldsymbol{T}}$ in magnitude. The oblique first mode and traveling crossflow mode are both of vortical nature. The receptivity coefficient demonstrates a consistent decrease as the sweep angle increases.

The receptivity to vorticity waves of these two modes is also consistent, while the

pathway is different from acoustic wave cases: At the leading edge, disturbances are generated at the leading edge through the complex interactions between the incoming vorticity wave, the shock wave, and the boundary layer. These disturbances comprise mainly $\boldsymbol{m}_B'$. Then the disturbances dissipate and exhibit a plateau in magnitudes. In this phase, all components undergo spatial reshaping, exhibiting similar behaviors with linear growth but at different proportions. Finally, the MPT components achieve equilibrium, and the linear growth occurs. In vorticity wave cases, all the receptivity coefficients are nearly 1. The receptivity coefficient is ineffective for quantifying the capability on exciting unstable modes.

The current results highlight the consistency between oblique first Mack modes and traveling crossflow modes in hypersonic boundary layers: Both instabilities belong to S modes. $\boldsymbol{m}_B'$ is the dominant component in both instabilities for their linear growth. The receptivity processes of both instabilities to slow acoustic waves and vorticity waves do not show qualitative differences. These observations suggest that the first and crossflow modes are of the same nature.

Based on the unified characterization of first and crossflow instabilities as inherently consistent S modes, systematic parametric studies are required to quantify the impacts of flow parameters, i.e., Mach number and Reynolds number, on these instabilities. This unified understanding sheds light on the design of laminar control techniques. Control methods such as wall cooling and blowing-suction may be refined within a unified framework, potentially reducing the cost of such techniques.

Chapter 6 Conclusion

6.1. Summary and Conclusions

The thesis studies the linear instability and control methods of first Mack mode and crossflow mode with direct numerical simulation, linear stability theory, and momentum potential theory. The aims depicted in Figure 1-1 are achieved by discussing the first Mack and crossflow modes in different cases. Complete physical interpretations of first Mack and crossflow modes are given as follows:

Slightly oblique first modes manifest oscillatory waves trapped between the sonic line and the wall, resembling second-mode behaviors. For larger β, however, new vortex pairs emerge at the sonic line, rapidly expanding to dominate the region beneath the generalized inflection point, signifying a vortex-dominant mechanism. The critical point for this transition coincides with the maximum streamwise wavenumber α_r.

The distinct physical characteristics of first modes lead to differing responses to stabilization techniques: Wall cooling marginally stabilizes 2D first modes and significantly stabilizes highly oblique first modes by suppressing the thermal component. Wall suction similarly exhibits a weaker stabilization effect on 2D first modes compared to their highly oblique counterparts, with the latter showing damped thermal and vortical components under steady suction. Porous coatings and grooves share similar stabilization mechanisms, despite their different geometric scales. They both govern 2D first modes through wall–admittance mechanisms, where acoustic component modulations are responsible for their stabilization and destabilization effects. For highly oblique first modes, destabilization effects arise primarily from baseflow distortions.

Traveling crossflow modes exhibit similar stabilization mechanisms except for a less active thermal component compared to oblique first Mack modes: The stabilization effect of wall cooling originates from the damping of the thermal component. Wall suction influences the vortical component directly. Mean-flow distortions of grooves interpret their slight stabilization effects, which also account for the minimal impact of porous coatings.

Oblique first Mack and traveling crossflow instabilities share identical receptivity pathways: For slow acoustic waves, strong acoustic components are generated at the leading edge through the synchronization mechanism and subsequently diminish. The vortical components grow steadily throughout the receptivity process, resulting in a

high-growth-rate non-modal growth phase of perturbations. After adjustments of acoustic and thermal components, the linear growth occurs. While for vorticity waves, leading-edge disturbances primarily consist of vortical components, arising from interactions between vorticity waves, shock waves, and boundary layers. Acoustic and vortical components go through adjustment in their shape, and thermal components exhibit initial decay followed by recovery, resulting in a lower-growth-rate non-modal growth phase. Ultimately, the linear growth phase commences.

The consistencies between oblique first Mack and traveling crossflow instabilities are highlighted by their identical categorization as S modes, unified receptivity pathways, shared vortical nature, and similar stabilization mechanisms.

6.2. Possible Directions for Future Work

The observations noted in this thesis encourage a future course of work in the following directions:

- Further investigation into the relationship between the first Mack and crossflow instabilities:

Chapter 5 demonstrates that oblique first Mack and traveling crossflow instabilities share identical receptivity pathways, suggesting a common physical nature. However, a critical issue remains unresolved, which concerns their divergent responses to pressure gradients. Clarifying the underlying mechanisms could contribute to the design of laminar control techniques within a unified theoretical framework. Establishing the energy budget for their disturbance growth offers a promising pathway to resolving this problem.

- Secondary instabilities of first Mack and crossflow modes:

The linear instability of these two modes has been analyzed in detail, while their secondary instabilities and breakdown processes remain unexamined. As noted in Chapter 1, previous experimental and numerical studies highlight the critical role of these modes in boundary-layer transition. Considering their fundamental similarities, the secondary instability of these two modes may exhibit analogous behaviors. These parallels could establish a unified framework for predicting and controlling transitions driven by these instabilities.

- Spanwise-uneven control strategies for first Mack modes:

Crossflow instabilities are efficiently stabilized by 3D biasing of the baseflow[51].

The 3D biasing can be introduced by patterned roughness[124], localized pinpoint suction[94], and volume-force actuators[125]. Since the first Mack and crossflow modes share similar physical properties, the effects of spanwise-uneven control strategies on first Mack modes have not been systematically investigated.

- Combined control strategies for first Mack and crossflow modes:

Since the stabilizing mechanisms of wall blowing-suction, wall cooling-heating, and grooves are clarified, combining these strategies becomes a viable option. For example, groove cavities could simultaneously function as suction pores, potentially enhancing the stabilization effect on crossflow instabilities. Further investigations on combined control strategies are needed.

References

[1] A. Fedorov, "Transition and stability of high-speed boundary layers," *Annual Review Fluid Mechanics*, vol. 43, pp. 79–95, 2011.

[2] Z. B. Riley, R. Deshmukh, B.A. Miller, J.J. McNamara, and K.M. Casper, "Characterization of structural response to hypersonic boundary-layer transition," *AIAA Journal*, vol. 54, pp. 2418–2431, 2016.

[3] A. H. Whitehead, Jr., "NASP aerodynamics," in *National Aerospace Plane Conference.* July 1989. AIAA 1989-5013.

[4] Y. Zhu, D. Gu, W. Zhu, S. Chen, C. Lee, and E. S. Oran, "Dilatational-wave-induced aerodynamic cooling in transitional hypersonic boundary layers," *Journal of Fluid Mechanics*, vol. 911, pp. A36, 2021.

[5] M. Morkovin, E. Reshotko, and T. Herbert, "Transition in open flow systems: a reassessment," *Bulletin of the American Physical Society*, vol. 39, no. 9, p. 1882, 1994.

[6] W. S. Saric, H. L. Reed, and E. J. Kerschen, "Boundary-layer receptivity to freestream disturbances," *Annual Review of Fluid Mechanics*, vol. 34, pp. 291–319, 2002.

[7] P. Balakumar. "Receptivity of Hypersonic Boundary Layers to Acoustic and Vortical Disturbances (Invited)," in *45th AIAA Fluid Dynamics Conference*. June 2015. AIAA 2015-2473.

[8] L. M. Mack, "Linear stability theory and the problem of supersonic boundary-layer transition," *AIAA Journal*, vol. 13, pp. 278–289, 1975.

[9] M. R. Malik, "Numerical methods for hypersonic boundary layer stability," *Journal of Computational Physics*, vol. 86, no. 2, pp. 376–413, 1990.

[10] Z. Liu, "Cross-flow linear instability in compressible boundary layers over a flat plate," *Physics of Fluids*, vol. 34, no. 9, pp. 094110,2022.

[11] L. M. Mack, "Boundary-Layer Linear Stability Theory," in *AGARD Report No. 709*, 1984.

[12] N. Malmuth, A. Fedorov, V. Shalaev, J. Cole, M. Hites, D. Williams, and A. Khokhlov. "Problems in high speed flow prediction relevant to control," in *2nd AIAA, Theoretical Fluid Mechanics Meeting*. June 1998. AIAA 1998-2695.

[13] W. S. Saric, H. L. Reed, and E. B, White, "Stability and transition of three-dimensional boundary layers," *Annual Review of Fluid Mechanics*, vol. 35, pp. 413–440, 2003.

[14] M. Morkovin, "Transition at hypersonic speeds," in *Technical Report ICASE*

Interim Report 1, NASA Contractor Report 178315, ICASE, NASA Langley Research Center, NASA Langley Research Center, Hampton, VA (1987).

[15] C. P. Knisely and X. Zhong, "Sound radiation by supersonic unstable modes in hypersonic blunt cone boundary layers. I. Linear stability theory," *Physics of Fluids*, vol. 31, pp. 24103, 2019.

[16] J. J. Kuehl, "Thermoacoustic interpretation of second-mode instability," *AIAA Journal*, vol. 56, pp. 3585–3592, 2018.

[17] X. Tian and C. Wen, "Growth mechanisms of second-mode instability in hypersonic boundary layers," *Journal of Fluid Mechanics*, vol. 908, pp. R4, 2021.

[18] X. Chen, Y. Zhu, and C. Lee, "Interactions between second mode and low-frequency waves in a hypersonic boundary layer," *Journal of Fluid Mechanics*, vol. 820, pp. 693–735, 2017.

[19] Y. Zhu, W. Zhu, D. Gu, C. Lee, and C. R. Smith, "Characteristics of transition to turbulence over a Mach 6 flared cone," *Physics of Fluids*, vol. 33, pp. 101708, 2021.

[20] P. Guo, J. Hao, and C. Y. Wen, "Interaction and breakdown induced by multiple optimal disturbances in hypersonic boundary layer," *Journal of Fluid Mechanics*, vol. 974, pp. A50, 2023.

[21] P. J. Schmid and D.S. Henningson, "Stability and transition in shear flows," Springer: New York, 2001.

[22] L. M. Mack, "On the inviscid acoustic-mode instability of supersonic shear flows," *Theoretical and Computational Fluid Dynamics*, vol. 2, pp. 97–123, 1990.

[23] F. T. Smith, "On the first-mode instability in subsonic, supersonic or hypersonic boundary layers," *Journal of Fluid Mechanics*, vol. 198, pp. 127–153, 1989.

[24] T. Liang, S. Kafle, A. A. Khan, P. Paredes, and J. Kuehl, "On the inviscid energetics of Mack's first mode instability," *Theoretical and Computational Fluid Dynamics*, vol. 37, pp. 1–15, 2023.

[25] M. Sippel. "Research on TBCC Propulsion for a Mach 4.5 Supersonic Cruise Airliner," in *14th AIAA/AHI Space Planes and Hypersonic Systems and Technologies Conference*. November 2006. AIAA 2006-7976.

[26] S. A. Craig, and W. S. Saric, "Crossflow instability in a hypersonic boundary layer," *Journal of Fluid Mechanics*, vol. 808, pp. 224–244, 2016.

[27] J. Chen, S. Yi, X. Li, G. Han, Y. Zhang, Q. Yang, and X. Yuan, "Theoretical, numerical and experimental study of hypersonic boundary layer transition: Blunt circular cone," *Applied Thermal Engineering*, vol. 194, pp. 116931, 2021.

[28] F. Li, M. Choudhari, C. L. Chang and J. White. "Analysis of Instabilities in Non-Axisymmetric Hypersonic Boundary Layers over Cones," in *10th AIAA/ASME Joint Thermophysics and Heat Transfer Conference*, June 2010. AIAA 2010-4643.

[29] A. J. Moyes, P. Paredes, T. S. Kocian and H. L. Reed. "Secondary Instability Analysis of Crossflow on a Hypersonic Yawed Straight Circular Cone," in *54th AIAA Aerospace Sciences Meeting*, January 2016. AIAA 2016-0848.

[30] J. Chen, S. Dong, X. Chen, X. Yuan, and G. Xu, "Stationary cross-flow breakdown in a high-speed swept-wing boundary layer," *Physics of Fluids*, vol. 33, no. 2, pp. 024108, 2021.

[31] H. Qiu, M. Shi, Y. Zhu, and C. Lee, "Boundary layer transition of hypersonic flow over a delta wing," *Journal of Fluid Mechanics*, vol. 980, pp. A57, 2024.

[32] G. Xu, J. Chen, G. Liu, S. Dong, and S. Fu, "The secondary instabilities of stationary cross-flow vortices in a mach 6 swept wing flow," *Journal of Fluid Mechanics*, vol. 873, pp. 914–941, 2019.

[33] H. Quintanilha, P. Paredes, A. Hanifi, and V. Theofilis, "Transient growth analysis of hypersonic flow over an elliptic cone," *Journal of Fluid Mechanics*, vol. 935, pp. A40, 2022.

[34] P. Balakumar, and R. A. King, "Receptivity and stability of supersonic swept flows," *AIAA Journal*, vol. 50, no. 7, pp. 1476–1489, 2012.

[35] X. Chen, S. Dong, G. Tu, X. Yuan, and J. Chen, "Boundary layer transition and linear modal instabilities of hypersonic flow over a lifting body," *Journal of Fluid Mechanics*, vol. 938, pp. A8, 2022.

[36] B. M. Wheaton, D. C. Berridge, T. D. Wolf, D. B. Araya, R. T. Stevens, B. E. Mcgrath, B. L. Kemp, and D. W. Adamczak, "Final design of the boundary layer transition (bolt) flight experiment," *Journal of Spacecraft and Rockets*, vol. 58, no. 1, pp. 6–17, 2021.

[37] H. Deyhlet, and H. Bippes, "Disturbance Growth in an Unstable Three-Dimensional Boundary Layer and its Dependence on Environmental Conditions," *Journal of Fluid Mechanics*, vol. 316, pp. 73–113, 1996.

[38] H. Bippes, "Basic Experiments on Transition in Three-Dimensional Boundary Layers Dominated by Crossflow Instability," *Progress in Aerospace Sciences*, vol. 35, pp. 363–412, 1999.

[39] E. B. White, and W. S. Saric, "Secondary Instability of Crossflow Vortices," *Journal of Fluid Mechanics*, vol. 525, pp. 275–308, 2005.

[40] L. R. Owens, G. Beeler, R. King, A. Chou, P. Balakumar and D. Banks. "Supersonic Crossflow Transition Control in Ground and Flight Tests," in *AIAA*

Scitech 2019 Forum. January 2019. AIAA 2019-1651.

[41] P. Balakumar and R. King. "Receptivity to Roughness, Acoustics, and Vortical Disturbances in Supersonic Boundary Layers Over Swept Wings," in *41st AIAA Fluid Dynamics Conference and Exhibit*. June 2011. AIAA 2011-3880.

[42] A. J. Moyes, P. Paredes, T. S. Kocian, and H. L. Reed, "Secondary Instability Analysis of Crossflow on a Hypersonic Yawed Straight Circular Cone," *Journal of Fluid Mechanics*, vol. 812, pp. 370–397, 2017.

[43] G. Beeler, S. Wilkinson, P. Balakumar and K. McDaniel. "Crossflow Instability on a Wedge-Cone at Mach 3.5," in *42nd AIAA Fluid Dynamics Conference and Exhibit*. June 2012. AIAA 2012-2825.

[44] B. Wan, G. Tu, X. Yuan, J. Chen, and Y. Zhang, "Identification of Traveling Crossflow Waves under Real Hypersonic Flight Conditions," *Physics of Fluids*, vol. 33, no. 4, pp. 044110, 2021.

[45] R. Song, and M. Dong, "Linear instability of a supersonic boundary layer over a rotating cone," *Journal of Fluid Mechanics*, vol. 955, pp. A31, 2023.

[46] Z. Liu, "On the identification of cross-flow mode in three-dimensional boundary layers," *AIP Advances*, vol. 13, pp. 15203, 2023.

[47] M. M. Peck, K. J. Groot, and H. L. Reed, "Boundary-layer instability on a highly swept fin on a cone at mach 6," *Journal of Fluid Mechanics*, vol. 987, pp. A13, 2024.

[48] H. L. Reed, and W. S. Saric, "Stability of three-dimensional boundary layers," *Annual Review of Fluid Mechanics*, vol. 21, pp. 235–284, 1989.

[49] Y. H. Zurigat, A. H. Nayfeh, and J. A. Masad, "Effect of pressure gradient on the stability of compressible boundary layers," *AIAA Journal*, vol. 30, no. 9, pp. 2204–2211, 1992.

[50] J. A. Masad, and Y. H. Zurigat, "Effect of pressure gradient on first mode of instability in compressible boundary layers." *Physics of Fluids*, vol. 6, no. 12, pp. 3945–3953, 1994.

[51] W. Saric and H. Reed. "Crossflow Instabilities - Theory & Technology," in *41st Aerospace Sciences Meeting and Exhibit*. January 2003. AIAA 2003-771.

[52] A. Fedorov. "Receptivity of High Speed Boundary Layer to Acoustic Disturbances (Invited)," in *32nd AIAA Fluid Dynamics Conference and Exhibit*. June 2002. AIAA 2002-2846.

[53] Y. Chen, G. Tu, B. Wan, C. Su, X. Yuan, and J. Chen, "Receptivity of a hypersonic flow over a blunt wedge to a slow acoustic wave," *Physics of Fluids*, vol. 33, no. 8, pp. 084114, 2021.

[54] B. Wan, J. Chen, X. Yuan, W. Hu, and G. Tu, "Three-dimensional receptivity of

a blunt-cone boundary layer to incident slow acoustic waves," *AIAA Journal*, vol. 60, no. 8, pp. 4523–4531, 2022.

[55] M. Niu, and C. Su, "Receptivity and its influence on transition prediction of a hypersonic boundary layer over a small bluntness cone," *Physics of Fluids*, vol. 35, no. 3, pp. 034109, 2023.

[56] A. Fedorov, and A. Khokhlov, "Prehistory of instability in a hypersonic boundary layer," *Theoretical and Computational Fluid Dynamics*, vol. 14, pp. 359–375, 2001.

[57] Y. Ma, and X. Zhong, "Receptivity of a supersonic boundary layer over a flat plate. part 1. wave structures and interactions," *Journal of Fluid Mechanics*, vol. 488, pp. 31–78, 2003.

[58] Y. Ma, and X. Zhong, "Receptivity of a supersonic boundary layer over a flat plate. part 2. receptivity to free-stream sound," *Journal of Fluid Mechanics*, vol. 488, pp. 79–121, 2003.

[59] Y. Ma, and X. Zhong, "Receptivity of a supersonic boundary layer over a flat plate. part 3. effects of different types of free-stream disturbances," *Journal of Fluid Mechanics*, vol. 532, pp. 63–109, 2005.

[60] X. Zhong, and X. Wang, "Direct numerical simulation on the receptivity, instability, and transition of hypersonic boundary layers," *Annual Review of Fluid Mechanics*, vol. 44, pp. 527–561, 2012.

[61] K. Kara, P. Balakumar, and O. A. Kandil, "Effects of nose bluntness on hypersonic boundary-layer receptivity and stability over cones," *AIAA Journal*, vol. 49, no. 12, pp. 2593–2606, 2011.

[62] P. Balakumar, and M. A. Kegerise, "Receptivity of hypersonic boundary layers over straight and flared cones," *AIAA Journal*, vol. 53, no. 8, pp. 2097–2109, 2015.

[63] Y. Liu, M., Dong, and X. Wu, "Generation of first mack modes in supersonic boundary layers by slow acoustic waves interacting with streamwise isolated wall roughness," *Journal of Fluid Mechanics*, vol. 888, pp. A10, 2020.

[64] G. Xu, G. Liu, J. Chen, and S. Fu, "Role of freestream slow acoustic waves in a hypersonic three-dimensional boundary layer," *AIAA Journal*, vol. 56, no. 9, pp. 3570–3584, 2018.

[65] A. Fedorov, and A. Tumin, "High-speed boundary-layer instability: Old terminology and a new framework," *AIAA Journal*, vol. 49, no. 8, pp. 1647–1657, 2011.

[66] R. Kimmel. "Aspects of Hypersonic Boundary Layer Transition Control," in *41st Aerospace Sciences Meeting and Exhibit*. January 2003. AIAA 2003-772.

[67] X. Wang, X. Zhong, and Y. Ma. "Response of a Hypersonic Boundary Layer to Wall Blowing-Suction," *AIAA Journal*, vol. 49, no. 7, pp. 1336–1353, 2011.

[68] F. Li, M. Choudhari, C.-L. Chang, and J. White, "Effects of injection on the instability of boundary layers over hypersonic configurations," *Physics of Fluids*, vol. 25, no. 10, pp. 104107, 2013.

[69] F. Miró Miró, and F. Pinna, "Effect of uneven wall blowing on hypersonic boundary-layer stability and transition," *Physics of Fluids*, vol. 30, no. 8, pp. 084106, 2018.

[70] R. Zhao, C.Y. Wen, X.D. Tian, T.H. Long, and W. Yuan, "Numerical simulation of local wall heating and cooling effect on the stability of a hypersonic boundary layer," *International Journal of Heat and Mass Transfer*, vol. 121, pp. 986–998, 2018.

[71] A. Sidorenko, Y. Gromyko, D. Bountin, P. Polivanov, and A. Maslov, "Effect of the local wall cooling/ heating on the hypersonic boundary layer stability and transition," *Progress in Flight Physics*, vol. 7, pp. 549–568, 2015.

[72] A.V. Fedorov, V.G. Soudakov, I.V. Egorov, "High-speed boundary-layer stability on a cone with localized wall heating or cooling," *AIAA Journal*, vol. 53, no. 9, pp. 2512–2524, 2015.

[73] M. Riherd, S. Roy, and S. Balachandar, "Local stability effects of plasma actuation on a zero pressure gradient boundary layer," *Theoretical and Computational Fluid Dynamics*, vol. 28, pp. 65–87, 2014.

[74] H. Yang, H. Liang, C. Zhang, Y. Wu, H. Zong, Z. Su, Y. Kong, D. Zhang, and Y. Li, "Investigation of hypersonic cone boundary layer stability regulation with plasma actuation," *Physics of Fluids*, vol. 35, no. 2, pp. 024112, 2023.

[75] J. Hao, and C.-Y. Wen. "Stabilization of a Two-Dimensional Hypersonic Boundary Layer Using a Shallow Cavity," *AIAA Journal*, vol. 59, no. 2, pp. 430–438, 2021.

[76] M. Dong, and C. Li. "Effect of Two-Dimensional Short Rectangular Indentations on Hypersonic Boundary-Layer Transition," *AIAA Journal*, vol. 59, no. 7, pp. 2368–2381, 2021.

[77] R. Zhao, C. Wen, Y. Zhou, G. Tu, and J. Lei, "Review of acoustic metasurfaces for hypersonic boundary layer stabilization," *Progress in Aerospace Sciences*, vol. 130, pp. 100808, 2022.

[78] V. I. Lysenko, A. A. Maslov, "The effect of cooling on supersonic boundary-layer stability," *Journal of Fluid Mechanics*, vol. 147, pp. 39–52, 1984.

[79] M. R. Malik, "Prediction and control of transition in supersonic and hypersonic boundary layers," *AIAA Journal*, vol. 27, no. 11, pp. 1487–1493, 1989.

[80] Heath Johnson, Joel Gronvall and Graham Candler. "Reacting Hypersonic Boundary Layer Stability with Blowing and Suction," in *47th AIAA Aerospace Sciences Meeting including The New Horizons Forum and Aerospace Exposition*, January 2009. AIAA 2009-938.

[81] A. Poulain, C. Content, G. Rigas, E. Garnier, and D. Sipp, "Adjoint-based linear sensitivity of a supersonic boundary layer to steady wall blowing-suction/ heating-cooling." *Journal of Fluid Mechanics*, vol. 978, pp. A16, 2024.

[82] A. V. Fedorov, N. D. Malmuth, A. Rasheed, and H.G. Hornung, "Stabilization of hypersonic boundary layers by porous coatings," *AIAA Journal*, vol. 39, pp. 605–610, 2001.

[83] V. F. Kozlov, A. V. Fedorov, and N.D. Malmuth, "Acoustic properties of rarefied gases inside pores of simple geometries," *the Journal of the Acoustical Society of America*, vol. 117, pp. 3402–3411, 2005.

[84] G. A. Brès, M. Inkman, T. Colonius, and A.V. Fedorov, "Second-mode attenuation and cancellation by porous coatings in a high-speed boundary layer," *Journal of Fluid Mechanics*, vol. 726, pp. 312–337, 2013.

[85] A. Rasheed, H.G. Hornung, A.V. Fedorov, and N.D. Malmuth, "Experiments on passive hypervelocity boundary-layer control using an ultrasonically absorptive surface," *AIAA Journal*, vol. 40, pp. 481–489, 2002.

[86] A.V. Fedorov, A. Shiplyuk, A. Maslov, E. Burov, and N. Malmuth, "Stabilization of a hypersonic boundary layer using an ultrasonically absorptive coating," *Journal of Fluid Mechanics*, vol. 479, pp. 99–124, 2003.

[87] X. Wang and X. Zhong, "Numerical simulations on mode S growth over feltmetal and regular porous coatings of a Mach 5.92 flow" in *49th AIAA Aerospace Sciences Meeting Including the New Horizons Forum and Aerospace Exposition*, 2011. AIAA 2011-375.

[88] X. Tian, R. Zhao, T. Long, and C.Y. Wen, "Reverse design of ultrasonic absorptive coating for the stabilization of Mack modes," *AIAA Journal*. vol. 57, pp. 2264–2269, 2019.

[89] R. Zhao, X. Liu, C. Wen, and X. Wang, "Broadband design of acoustic metasurfaces for the stabilization of a Mach 4 boundary layer flow," *Advances in Aerodynamics*, vol. 4, pp. 15, 2022.

[90] Y. Chen, P. Guo, and C. Wen, "A unified explanation of energy growth sources for unstable modes in flat-plate boundary layers," *Journal of Fluid Mechanics*, vol. 972, pp. A5, 2023.

[91] Z. Liu, T. Zhou, Y. Lu, and C. Yan, "Control of first-mode oblique breakdown in a supersonic boundary layer using micro-groove coating strips," *Physics of*

Fluids, vol. 34, pp. 74104, 2022.

[92] R. Zhao, C. Y. Wen, T. H. Long, and X. D. Tian, "Spatial Direct Numerical Simulation of the Hypersonic Boundary-Layer Stabilization Using Porous Coatings," *AIAA Journal*, vol. 57, no. 6, pp. 2264–2269, 2019.

[93] R. Zhao, X. X. Zhang, and C. Y. Wen, "Theoretical modeling of porous coatings with simple microstructures for hypersonic boundary-layer stabilization," *AIAA Journal*, vol. 58, pp. 981–986, 2020.

[94] T. Friederich, and M. J. Kloker, "Control of the Secondary Cross-Flow Instability Using Localized Suction," *Journal of Fluid Mechanics*, vol. 706, pp. 470–495, 2012.

[95] J. Eppink, and R. Wlezien, "Data Analysis for the NASA/Boeing Hybrid Laminar Flow Control Crossflow Experiment," in 41st AIAA Fluid Dynamics Conference and Exhibit, June 2011. AIAA 2011-3879.

[96] A. Fedorov, and A. Novikov, "Stabilization of Crossflow Mode by Grooves on a Supersonic Swept Wing," *Theoretical and Computational Fluid Dynamics*, vol. 37, pp. 261–268, 2023.

[97] L. S. G. Kovasznay, "Turbulence in Supersonic Flow," *Journal of the Aeronautical Sciences*, vol. 20, no. 10, pp. 657–682, 1953.

[98] P. E. Doak, "Momentum Potential Theory of Energy Flux Carried by Momentum Fluctuations," *Journal of Sound and Vibration*, vol. 131, no. 1, pp. 67–90, 1989.

[99] P. E. Doak, "Fluctuating Total Enthalpy as the Basic Generalized Acoustic Field," *Theoretical and Computational Fluid Dynamics*, vol. 10, pp. 115–133, 1998.

[100] S. Unnikrishnan, and D. V. Gaitonde, "Acoustic, Hydrodynamic and Thermal Modes in a Supersonic Cold Jet," *Journal of Fluid Mechanics*, vol. 800, pp. 387–432, 2016.

[101] P. Jordan, G. Daviller, and P. Comte, "Doak's Momentum Potential Theory of Energy Flux Used to Study a Solenoidal Wavepacket," *Journal of Sound and Vibration*, vol. 332, no. 17, pp. 3924–3936, 2013.

[102] S. Unnikrishnan, "Recent Advances in Feature Extraction Techniques for High-Speed Flowfields," *Progress in Aerospace Sciences*, vol. 140, pp. 100918, 2023.

[103] S. Unnikrishnan, and D. V. Gaitonde, "Interactions between Vortical, Acoustic and Thermal Components during Hypersonic Transition," *Journal of Fluid Mechanics*, vol. 868, pp. 611–647, 2019.

[104] S. Unnikrishnan, and D. V. Gaitonde, "Instabilities and Transition in Cooled Wall Hypersonic Boundary Layers," *Journal of Fluid Mechanics*, vol. 915, pp.

A26, 2021.

[105] T. Long, Y. Dong, R. Zhao, and C. Wen, "Mechanism of Stabilization of Porous Coatings on Unstable Supersonic Mode in Hypersonic Boundary Layers," *Physics of Fluids*, vol. 33, no. 5, pp. 054105, 2021.

[106] T. Long, P. Guo, R. Zhao, C. Wen, and F. Ji, "Energy Growth of Vortical, Acoustic, and Entropic Components of the Second-Mode Instability in the Hypersonic Boundary Layer," *Physics of Fluids*, vol. 35, no. 5, pp. 054104, 2023.

[107] X. Liu, Y. Dong, T. Long, R. Zhao, and C. Wen, "Stabilization Mechanisms of Various Acoustic Metasurfaces on the Second Mode in Hypersonic Boundary-Layer Flows," *Physics of Fluids*, vol. 35, no. 10, pp. 104102, 2023.

[108] W. Zhu, and C. Lee, "Perturbation Decomposition over a Flared Cone with a Wavy Wall," in *AIAA AVIATION 2022 Forum*, 2022. AIAA 2022-3854.

[109] J. Ren and S. Fu, "Competition of the multiple Görtler modes in hypersonic boundary layer flows," *Science China Physics, Mechanics & Astronomy*, vol. 57, pp. 1178, 2014.

[110] R.Song, L.Zhao, and Z.Huang, "Secondary instability of stationary Görtler vortices originating from first/second Mack mode," *Physics of Fluids*, vol. 32, pp. 034109, 2020.

[111] T. Zhou, Z. Liu, Y. Lu, Y. Wang, and C. Yan, "Direct numerical simulation of complete transition to turbulence via first- and second-mode oblique breakdown at a high-speed boundary layer," *Physics of Fluids*, vol. 34, pp. 74101, 2022.

[112] Q. Song and L. Zhao, "Scattering of Mack modes by solid-porous junctions in hypersonic boundary layers," *Physics of Fluids*, vol. 34, pp. 84104, 2022.

[113] Z. Hong, Z. Ye, and K. Ye, "Effect of two-dimensional micro-cavity surface on hypersonic boundary layer," *Acta Astronautica*, vol. 206, pp. 188–205, 2023

[114] C. J. Mack, and P. J. Schmid, "Global Stability of Swept Flow around a Parabolic Body: The Neutral Curve," *Journal of Fluid Mechanics*, vol. 678, pp. 589–599, 2011.

[115] A. P. Haas, C. Hader, and H. F. Fasel, "Linear Stability Investigation of Cross-Flow Instability for a Supersonic Swept Wing with a Biconvex Airfoil," in *AIAA AVIATION 2021 FORUM*, 2021. AIAA 2021-2848.

[116] S. G. Lekoudis, "Stability of the Boundary Layer on a Swept Wing with Wall Cooling," *AIAA Journal*, vol. 18, no. 9, pp. 1029–1035, 1980.

[117] L. M. Mack, "Compressible Boundary-Layer Stability Calculations for Sweptback Wings with Suction," *AIAA Journal*, vol. 20, no. 3, pp. 363–369, 1982.

[118] P. Wassermann, and M. Kloker, "Mechanisms and Passive Control of Crossflow-Vortex-Induced Transition in a Three-Dimensional Boundary Layer," *Journal of Fluid Mechanics*, vol. 456, pp. 49–84, 2002.

[119] L. M. Mack, "Stability of Three-Dimensional Boundary Layers on Swept Wings at Transonic Speeds," in *Symposium Transsonicum III. International Union of Theoretical and Applied Mechanics*, Zierep, J. and Oertel, H., Springer, Berlin, Heidelberg. 1989.

[120] K. P. Griffin, L. Fu, and P. Moin, "General method for determining the boundary layer thickness in nonequilibrium flows," *Physical Review Fluids*, vol. 6, pp. 024608, 2021.

[121] K. Stetson, "Nosetip bluntness effects on cone frustum boundary layer transition in hypersonic flow," in *16th Fluid and Plasmadynamics Conference*, July 1983. AIAA 1983-1763.

[122] J. van Ingen. "The eN Method for Transition Prediction. Historical Review of Work at TU Delft," in *38th Fluid Dynamics Conference and Exhibit*, June 2008. AIAA 2008-3830.

[123] C. Su, and J. Geng, "Interaction of weak free-stream disturbance with an oblique shock: validation of the shock-capturing method, " *Applied Mathematics and Mechanics*, vol. 38, pp. 1601–1612, 2017.

[124] T. Corke, A. Arndt, E. Matlis, and M. Semper, "Control of stationary cross-flow modes in a Mach 6 boundary layer using patterned roughness," *Journal of Fluid Mechanics*, vol. 856, pp. 822–849, 2018.

[125] Z. Guo, and M. J. Kloker, "Control of crossflow-vortex-induced transition by unsteady control vortices," *Journal of Fluid Mechanics*, vol. 871, pp. 429–449, 2019.